

**FACULTY  
OF MATHEMATICS  
AND PHYSICS**  
Charles University

**DOCTORAL THESIS**

Viktor Pěč

**Precise measurement of the electron  
antineutrino oscillation**

Institute of Particle and Nuclear physics

Supervisor of the doctoral thesis: Ing. Vít Vorobel, Ph.D.

Study programme: Physics

Study branch: Subnuclear Physics

Prague 2016



I declare that I carried out this doctoral thesis independently, and only with the cited sources, literature and other professional sources.

I understand that my work relates to the rights and obligations under the Act No. 121/2000 Sb., the Copyright Act, as amended, in particular the fact that the Charles University has the right to conclude a license agreement on the use of this work as a school work pursuant to Section 60 subsection 1 of the Copyright Act.

In ..... date .....

signature of the author



Title: Precise measurement of the electron antineutrino oscillation

Author: Viktor Pěč

Institute: Institute of Particle and Nuclear physics

Supervisor: Ing. Vít Vorobel, Ph.D., Institute of Particle and Nuclear physics

Abstract: The Daya Bay experiment is designed to precisely measure short-baseline disappearance of reactor antineutrinos from reactor cores at the Daya Bay nuclear power plant complex in the Guangdong Province of China. It presented the most precise measurements of oscillation parameters  $\sin^2 2\theta_{13} = 0.084 \pm 0.005$  and  $|\Delta m_{ee}^2| = (2.42 \pm 0.11) \times 10^{-3} \text{ eV}^2$ . Background to the antineutrino signals is mainly created by cosmic muons and is effectively suppressed by use of water Cherenkov and RPC muon detectors. This thesis describe testing of RPC detectors prior to their installation at the experimental site. Part of the cosmic muons stop in the experiment's antineutrino detectors, and they decay or are captured by  $^{12}\text{C}$  producing  $^{12}\text{B}$ . Isotope  $^{12}\text{B}$  contribute to accidental background. Rates of muon decays in the detectors are estimated in the thesis. The experiment can register electron antineutrinos from supernova with expected signals around 20 MeV. Energy scale of the detectors at 53 MeV is determined.

Keywords: neutrino oscillations, Daya Bay experiment, RPC, muon decay



I would like to thank my supervisor for the introduction to experimental physics and especially to the work with electronics at different levels of complexity.

I also acknowledge the team responsible for RPC tests at IHEP, Beijing, Ma Liehua, Xu Jilei, Logan Lebanowski, and Lin Shih-Kai. They have been not only diligent coworkers, but they have become good friends with whom the times I spent at IHEP became also fun. I am grateful to Sören Jetter for so many good times in Beijing, both professional and personal.

I would like to thank Dan Dwyer who mentored me during my short stays at LBNL, Berkeley.

A special thanks go to Dalibor Nosek with whom I have had never-ending discussions on various physical and personal topics, as well as several bike rides along the river Vltava.

I acknowledge a rather essential influence of my colleague Beda Roskovec. Many thanks go to all the people at our institute who have created very friendly environment.

Last but not least, I am grateful to my parents who have provided priceless support on the long journey to this point.



# Contents

<b>Introduction</b>	<b>3</b>
<b>1 Neutrino Oscillations</b>	<b>5</b>
1.1 History of Neutrino Oscillations . . . . .	5
1.2 Neutrino mixing . . . . .	6
1.3 Neutrino oscillations . . . . .	7
1.3.1 2 flavor case . . . . .	9
1.3.2 3 flavor case . . . . .	10
1.3.3 Electron antineutrino survival probability in three-neutrino mixing . . . . .	11
1.4 Neutrino mixing parameters . . . . .	11
1.5 Determining $\theta_{13}$ with nuclear reactors . . . . .	12
1.6 Results of Daya Bay . . . . .	14
1.7 Other Reactor $\bar{\nu}_e$ Oscillation Experiments . . . . .	16
<b>2 Atmospheric Muons from Cosmic Rays</b>	<b>19</b>
2.1 Cosmic Rays . . . . .	19
2.2 Production of Muons in the Atmosphere . . . . .	20
2.3 Sea level . . . . .	20
2.4 Underground . . . . .	21
<b>3 Experiment Daya Bay</b>	<b>23</b>
3.1 Experimental Overview . . . . .	23
3.2 Experimental Hall . . . . .	24
3.3 Antineutrino Detection . . . . .	25
3.3.1 Detection Method . . . . .	25
3.3.2 Antineutrino Detector . . . . .	26
3.4 Muon Veto System . . . . .	28
3.4.1 Water shield . . . . .	29
3.4.2 RPC . . . . .	31
3.5 Data Acquisition and Trigger . . . . .	33
3.5.1 PMT-based detectors . . . . .	33
3.5.2 RPC . . . . .	34
3.6 Antineutrino Signal . . . . .	34
3.7 Backgrounds . . . . .	37
3.7.1 Uncorrelated Background . . . . .	37
3.7.2 Correlated Background . . . . .	37
<b>4 RPC Testing</b>	<b>41</b>
4.1 The RPC System . . . . .	41
4.1.1 Bare chambers . . . . .	41
4.1.2 RPC modules . . . . .	43
4.1.3 Front-end-Electronics Card . . . . .	45
4.1.4 Filling gas composition and flow rate . . . . .	47
4.2 Training and testing of bare RPC chambers at IHEP . . . . .	47

4.2.1	Training of RPC . . . . .	48
4.2.2	Tests of RPC performance . . . . .	48
4.3	RPC Module Performance . . . . .	53
4.4	RPC Testing Setup in Prague . . . . .	56
<b>5</b>	<b>Muon Decay</b>	<b>61</b>
5.1	Spectrum of $e^-/e^+$ in Born approximation . . . . .	61
5.2	1st order radiative corrections . . . . .	62
5.3	Inner bremsstrahlung and radiative muon decay . . . . .	63
5.4	Spectrum of visible energy . . . . .	65
5.5	Decays in orbit . . . . .	66
5.6	Combined $\mu^-$ and $\mu^+$ decay spectrum . . . . .	68
<b>6</b>	<b>Analysis</b>	<b>71</b>
6.1	Rate of Muon Decays . . . . .	71
6.1.1	Event Selection . . . . .	71
6.1.2	Selection Efficiency . . . . .	75
6.1.3	Rate of Muon Decays from MC Simulation . . . . .	91
6.1.4	Summary . . . . .	92
6.2	Detector Energy Scale at 53 MeV . . . . .	94
6.2.1	Model of reconstructed energies of muon decays . . . . .	94
6.2.2	Data Selection . . . . .	95
6.2.3	MC Simulations . . . . .	96
6.2.4	Fit to Data . . . . .	100
6.2.5	Summary . . . . .	100
	<b>Conclusion</b>	<b>103</b>
	<b>A Supplement to Model of Muon Decay</b>	<b>105</b>
A.1	Radiative Corrections to Muon Decay Process . . . . .	105
A.2	Branching Ratio of Radiative Muon Decay . . . . .	106
	<b>Bibliography</b>	<b>109</b>
	<b>List of Figures</b>	<b>115</b>
	<b>List of Tables</b>	<b>119</b>
	<b>List of Abbreviations</b>	<b>121</b>

# Introduction

Neutrino oscillation has attracted attention of many particle physicists as it is perceived as an evidence and affordable tool for investigation of physics beyond the Standard Model. Large experimental efforts for neutrino detection since 1950s resulted in detection and confirmation of neutrino oscillations at the beginning of this millennium.

Experiment Daya Bay is one of the current generation of experiments which aim to confirm and complete the current description of the oscillations. The experiment, located in southern China near Hong Kong, is designed to measure disappearance of electron antineutrinos from nuclear reactors at short baselines which is due to oscillation mode previously undetected. In 2012, Daya Bay announced discovery of the oscillation mode. Since then, Daya Bay has been providing precise measurement of parameters describing this oscillation,  $\theta_{13}$ , and  $\Delta m_{ee}^2$ .

Most of the background to the signal of antineutrino detection is created by cosmic ray muons. Daya Bay experimental halls are placed underground and are shielded against most of the muons, still, substantial amount of background is created. Active muon detectors are used to identify signals related to the cosmic muons and the background is suppressed to manageable level.

The muon detector system of the Daya Bay experiment consist of water Cherenkov detectors and arrays of modules built from resistive plate chambers—RPC. The RPC system is designed to increase efficiency of muon detection and, consequently, of background removal. It provides independent measurement of muon fluxes and it also has muon tracking capabilities. Its main value is in helping to understand production of muon related background and in validation of methods of background measurement.

Part of this thesis is the result of my contribution to building the RPC system of Daya Bay. I was a part of the group responsible for quality control of individual RPC chambers and I participated in their testing. I helped with installation of RPC modules in the experimental halls at the location of the experiment. The testing of RPC which took place in Beijing in 2008 and 2009 is described, and performance of the assembled modules is reported.

Second part of this thesis focuses on measurement of decays of cosmic muons in the antineutrino detectors of the experiment. I estimate total rates of the decays in each experimental hall. Rates of decays of stopped muons can help with determination of captures of negatively charged muons which produce relatively long-living isotope  $^{12}\text{B}$ , contributor to background signals. This method can help validate measurement of total production of the isotope, which is difficult using other methods.

Muon decays in the detector give signal with specific feature in the spectrum of registered energies. It has a steep edge at around 53 MeV and it can be used to calibrate the detector outside the range of energies covered by conventional calibration sources. Although this specific energy is beyond the interest of the main analysis of the antineutrino oscillation, for which the energies range up to about 12 MeV, it can be useful in validation of models describing the energy response of the detector. Moreover, Daya Bay is also sensitive to neutrinos from

supernovae, for which the signal energy is expected to have wide distribution peaking around 20 MeV and a calibration point at 53 MeV becomes useful. I present a method of estimation of energy response at the edge in the muon decay spectrum and give results for detectors in one of the experimental halls.

Daya Bay started measuring in December 2011 in partial configuration with only 6 out of final 8 antineutrino detectors installed. During the summer of 2012, remaining 2 detectors were installed and the experiment restarted measurements in full configuration in October 2012. The analyses of muon decays were done on data sample recorded from October 2012 through July 2015 in full configuration.

The thesis is structured into 6 chapters. Chapter 1 provides a short introduction into theoretical basics of neutrino oscillation and history of experimental evidence, and describe current situation with emphasis on measurements of reactor antineutrinos. Production of cosmic ray muons in the atmosphere and a description of their flux underground is the topic of Chapter 2. I give an overview of the Daya Bay experiment in Chapter 3. A detailed description of the RPC system is in Chapter 4 together with the report on testing of the RPC chambers and on performance of the modules. In Chapter 5, I introduce a model of energy distribution from decays of stopped cosmic muons. Chapter 6 is dedicated to the analysis of muon decays in the Daya Bay antineutrino detectors.

# 1. Neutrino Oscillations

Compelling evidence of transformation of one neutrino flavor to another, which is called neutrino oscillation, has been observed in solar, atmospheric, reactor and accelerator experiments, using a wide variety of detector technologies. The only known consistent explanation of these results is that neutrinos are massive and that the states which participate in weak interactions, the flavor states, are actually quantum superpositions massive particle states—the effect is called neutrino mixing.

The purpose of this chapter is to create a brief overview of the theoretical framework behind the oscillations as well as of experimental evidence and measurements of its parameters. I will start with history of neutrino detection and discovery of its oscillation. I will then summarize the current knowledge of the parameters of the neutrino mixing model. I will give more room to measurements of reactor antineutrinos, especially to the measurements of the Daya Bay experiment, and I will also briefly mention other current experiments.

## 1.1 History of Neutrino Oscillations

Current and past experiments which have been measuring neutrino oscillations can be classified based on the source of neutrinos they measure and the distance at which the respective neutrinos are registered. Neutrinos and antineutrinos from accelerators, reactors, the Sun, atmosphere, supernovae, artificially built strong radioactive sources, and decay processes in Earth has been observed by various experiments. The distance at which are detected then determine a subset of mixing parameters to which these experiments are sensitive to.

Reactor and solar neutrino experiments were among the first to detect neutrinos. The first observation of neutrinos was done in two experiments which observed reactor antineutrinos[1, 2]. Reactors are prolific sources of electron antineutrinos  $\bar{\nu}_e$  which are produced in beta decays of the fission products. Team led by Reines and Cowan was searching for  $\bar{\nu}_e$  interactions with protons in the detector's target region in which two signals correlated in time were produced. They pioneered the technique which is being used, with some modifications, in current experiments too.

It was the solar neutrino detection which led to the discovery of the now well accepted phenomenon of the neutrino oscillation. The neutrinos that are born in the Sun are electron neutrinos  $\nu_e$ . They are produced in the fusion reactions in the Sun's core. A deficit of them in the observed flux[3] on the Earth created a long lasting puzzle, the "Solar Neutrino Problem", which was resolved by introduction of the neutrino mixing and inclusion of the matter effect in the Sun.

However, the neutrino transformations were not confirmed until observations of SNO[4] and Super-Kamiokande[5]. Super-Kamiokande measured muon-flavored neutrinos which originate in the Earth's atmosphere. They saw distribution of zenith angles in muon-like neutrino events inconsistent with expected distribution, but it was consistent when two-flavor neutrino oscillation was assumed. This was real evidence of the neutrino transformations. However, it was not directly related to the solar neutrinos. SNO experiment was able to measure

neutrinos from the Sun in a flavor-independent way as well as in the interactions where only electron neutrinos participate. Their measured flavor-independent flux was in agreement with the standard solar model predictions for electron neutrinos, whereas the flux of only electron flavor was not. It turned out that the oscillation of Super-Kamiokande was of different kind than the one responsible for the Solar neutrino deficit. The effect of high electron density in the core of the Sun affects propagation of the electron neutrinos via the so called MSW[6, 7, 8] effect and is determined by the mixing of massive neutrinos  $\nu_1$  and  $\nu_2$ . The transformation observed by Super-Kamiokande is related to the mixing of  $\nu_1$  and  $\nu_2$  with  $\nu_3$ .

Major breakthrough came with results of reactor neutrino experiment KamLAND[9]. The experiment observed oscillatory variations in flux of  $\bar{\nu}_e$  from various nuclear power plants as function of distance-to-energy ratio. The neutrino oscillation could be considered as experimentally confirmed.

KamLAND not only confirmed the oscillation hypothesis but also gave precise measurements of the mixing parameters also involved in the solar neutrino transformations.

The last important type of experiments that I mention here are accelerator neutrino experiments. They detect neutrinos from a beam created at particle accelerators. First to measure muon neutrinos over large distances of hundreds of kilometers was K2K experiment[10]. More such experiments followed and provided precise measurement of the parameters involved in the oscillation of atmospheric neutrinos first observed by Super-Kamiokande.

The currently best measurements of the oscillation parameters will be listed in Section 1.4.

## 1.2 Neutrino mixing

The neutrino oscillation is a quantum effect which has been successfully described in the framework of quantum mechanics. More proper treatment in the framework of quantum field theory has also been used, however, the simple quantum-mechanical treatment of observed oscillations is sufficient in most cases.

The effect of oscillations arises from interference between states of different massive neutrinos which are produced and then detected coherently in weak interactions. The coherent interaction, in production and detection, is possible due to their very small mass difference relative to the masses and energies of the other participants of the interactions.

Neutrinos with a given flavor are not particles per se. The neutrino state  $\nu_\alpha$ ,  $\alpha = e, \mu, \dots$ , which participate in weak interaction with a lepton with flavor  $\alpha$ , can be therefore seen as a superposition of states of the massive neutrinos  $\nu_i$ ,  $i = 1, 2, \dots$ . I will, henceforth, denote generic flavor states with a Greek-letter indices and massive neutrino states with Latin indices. Both representations are orthogonal and there must exist a unitary transformation between the two,  $U_{\alpha i}$ , for which the relation between the mass and flavor states can be written as

$$|\nu_i\rangle = U_{\alpha i}|\nu_\alpha\rangle, \quad |\nu_\alpha\rangle = U_{\alpha i}^*|\nu_i\rangle \quad (1.1)$$

For the sake of clarity I used the standard Einstein's summation convention where the expression on the right-hand side is summed over the doubled index  $\alpha$ , or  $i$ .

The neutrino states are expressed in the usual bra-ket notation. The matrix  $U_{\alpha i}$  is commonly called mixing matrix and its elements can be expressed in terms of a scalar product of the state vectors:

$$U_{\alpha i} = \langle \nu_{\alpha} | \nu_i \rangle. \quad (1.2)$$

In the case of three neutrino flavor and massive states, it's known as the Pontecorvo-Maki-Nakagawa-Sakata mixing matrix, after the founders of the idea of neutrino mixing and of the formalism [11, 12]. The matrix is commonly parametrized with three angles,  $\theta_{12}$ ,  $\theta_{13}$ ,  $\theta_{23}$ , and three complex phases,  $\delta_{\text{CP}}$ ,  $\Phi_1$ ,  $\Phi_2$ :

$$U_{\text{PMNS}} = \begin{pmatrix} 1 & 0 & 0 \\ 0 & C_{23} & S_{23} \\ 0 & -S_{23} & C_{23} \end{pmatrix} \begin{pmatrix} C_{13} & 0 & \hat{S}_{13}^* \\ 0 & 1 & 0 \\ -\hat{S}_{13} & 0 & C_{13} \end{pmatrix} \begin{pmatrix} C_{12} & S_{12} & 0 \\ -S_{12} & C_{12} & 0 \\ 0 & 0 & 1 \end{pmatrix} \begin{pmatrix} e^{i\Phi_1} & & \\ & e^{i\Phi_2} & \\ & & 1 \end{pmatrix}, \quad (1.3)$$

where I used a shortcut notation of the trigonometric functions of the mixing angles,  $C_{jk} = \cos \theta_{jk}$ ,  $S_{jk} = \sin \theta_{jk}$ ,  $\hat{S}_{13} = e^{i\delta_{\text{CP}}} \sin \theta_{13}$ . This is the most general parametrization of any unitary matrix.  $\Phi_1$  and  $\Phi_2$  are the so called Majorana phases<sup>1</sup> and are relevant only if the neutrinos are Majorana particles. They, however, do not contribute to the neutrino oscillations as will be shown later in this chapter.

### 1.3 Neutrino oscillations

After a flavor state is produced, its massive parts evolve in time differently changing composition of the state and generating the oscillation of the probability that the flavor can be detected again. In quantum mechanics evolution of any state is determined by the evolution operator and time evolution of a flavor state  $|\nu_{\alpha}\rangle$  can be described as<sup>2</sup>:

$$|\nu_{\alpha}(t)\rangle = e^{-i\hat{H}t} |\nu_{\alpha}\rangle. \quad (1.4)$$

$\hat{H}$  is the Hamiltonian operator of the system and I assumed it was time independent.

The probability that the state with flavor  $\alpha$  will change into state with flavor  $\beta$  after time  $t$  is defined as

$$p_{\alpha \rightarrow \beta}(t) = |\langle \nu_{\beta} | \nu_{\alpha}(t) \rangle|^2. \quad (1.5)$$

The amplitude of the probability can be expressed using (1.4):

$$\begin{aligned} \langle \nu_{\beta} | \nu_{\alpha}(t) \rangle &= \langle \nu_{\beta} | e^{-i\hat{H}t} | \nu_{\alpha} \rangle = \langle \nu_{\beta} | \nu_i \rangle \langle \nu_i | e^{-i\hat{H}t} | \nu_j \rangle \langle \nu_j | \nu_{\alpha} \rangle = \\ &= \sum_{ij} U_{\alpha j}^* U_{\beta i} \langle \nu_i | e^{-i\hat{H}t} | \nu_j \rangle, \end{aligned} \quad (1.6)$$

<sup>1</sup> Because neutrinos have zero electric charge, they can be theoretically Dirac or Majorana particles.  $\Phi_1$  and  $\Phi_2$  phases are related to the Majorana's theory. This is discussed in depth for example in [13].

<sup>2</sup>Unless stated otherwise, I will use the natural system of units in which reduced Planck constant and speed of light are set to unity,  $\hbar = c = 1$ .

where the completeness relation  $\sum_i |\nu_i\rangle\langle\nu_i| = I$  ( $I$  stands for identity operator) was used before and after the evolution operator. The mixing matrix is the result of Equation (1.2).

When only free neutrino propagation is considered, i.e. there are no interaction terms in the Hamiltonian operator, the  $|\nu_i\rangle$  are eigenvectors of the Hamiltonian with the eigenvalues  $E_i$ <sup>†</sup> and relation (1.7) then reads as

$$\langle\nu_\beta|\nu_\alpha(t)\rangle = \sum_i U_{\alpha i}^* U_{\beta i} e^{-iE_i t}, \quad (1.7)$$

After inserting this expression into (1.5), the probability equation becomes

$$\begin{aligned} p_{\alpha\rightarrow\beta}(t) &= \sum_{ij} U_{\alpha i}^* U_{\beta i} U_{\alpha j} U_{\beta j}^* e^{-i\Delta E_{ij} t} = \\ &= \sum_{ij} \Re[U_{\alpha i}^* U_{\beta i} U_{\alpha j} U_{\beta j}^*] \cos(\Delta E_{ij} t) + \\ &\quad + \sum_{ij} \Im[U_{\alpha i}^* U_{\beta i} U_{\alpha j} U_{\beta j}^*] \sin(\Delta E_{ij} t), \end{aligned} \quad (1.8)$$

where  $\Delta E_{ij} = E_i - E_j$ . Calligraphic  $\Re$  and  $\Im$  denote real and imaginary part of the respective argument. The formula can be translated into more convenient form with sine functions only using the relations for cosine of double argument. The fact that the matrix  $U$  is unitary and the term  $U_{\alpha i}^* U_{\beta i} U_{\alpha j} U_{\beta j}^*$  has symmetric (antisymmetric) real (imaginary) part with respect to an exchange of the indices  $ij$ , leads to an expression which reflects unit probability for detection at the time of production,  $t = 0$ :

$$\begin{aligned} p_{\alpha\rightarrow\beta}(t) &= \delta_{\alpha\beta} - 4 \sum_{i>j} \Re[U_{\alpha i}^* U_{\beta i} U_{\alpha j} U_{\beta j}^*] \sin^2\left(\frac{\Delta E_{ij}}{2} t\right) + \\ &\quad + 2 \sum_{i>j} \Im[U_{\alpha i}^* U_{\beta i} U_{\alpha j} U_{\beta j}^*] \sin(\Delta E_{ij} t). \end{aligned} \quad (1.9)$$

As I mentioned previously, this formula is valid for freely propagating neutrinos. The oscillations which are described by (1.9) are often called vacuum oscillations. However, presence of matter affects how the massive states propagate. The effect is stronger with higher densities of matter as well as with higher energies of neutrinos in question. Reactor antineutrinos, with their relatively low energies ( $\sim 1$  MeV), are not affected by the presence of Earth matter. However, for example, high densities of electrons in the core of the Sun cause different propagation of the electron neutrinos of different energies. The matter effect is dominant there for multi-MeV neutrinos, whereas sub-MeV neutrinos propagate as if in vacuum.<sup>4</sup>

---

<sup>†</sup>Hamiltonian with only mass and kinetic terms is considered, therefore the states with definite mass and definite momentum are stationary.

<sup>4</sup>Details on modifications for the oscillations in matter can be found in any textbook on neutrino oscillations, and I can, again, recommend manuscript by Carlo Gunti and Chung W. Kim [13].

### 1.3.1 2 flavor case

For illustration of oscillations it is common to consider simplified case of two neutrino flavors, e.g.  $\nu_e$  and  $\nu_\mu$ . The mixing matrix  $U$  which expresses the relation to the corresponding massive neutrino states  $|\nu_1\rangle$  and  $|\nu_2\rangle$  has a simple form:

$$U = \begin{pmatrix} \cos \theta & \sin \theta \\ -\sin \theta & \cos \theta \end{pmatrix}. \quad (1.10)$$

It is parametrized using only one mixing angle  $\theta$ . Now, one can find, for example, the survival probability of the electron neutrino, which is straightforward after substituting generally complex mixing matrix in (1.9) with a real one from (1.10):

$$p_{\nu_e \rightarrow \nu_e}(t) = 1 - 4 \sin^2 \theta \cos^2 \theta \sin^2 \frac{\Delta E_{12} t}{2} = 1 - \sin^2 2\theta \sin^2 \frac{\Delta E_{12} t}{2}. \quad (1.11)$$

At this point, standard procedure is to make a equal-momentum assumption and ultrarelativistic approximation. The first assumption requires that the massive neutrino states are plane waves with definite and equal momentum. Therefore the only difference in their energies is due to the difference in their masses. Although this treatment is unrealistically simplistic, it yields prescriptions which are valid for all current experiments that measure neutrino oscillations.

The ultrarelativistic approximation then simplifies dispersion relations for the neutrinos and allows to equalize neutrino's travel time to the traveled distance. Both issues are discussed and solved in detail for example in chapters 7 and 8 of [13].

After the above mentioned approximations, the energy difference in (1.11) reads  $\Delta E_{12} = \Delta m_{12}^2 / 2E$ , where  $E$  is the average energy of the neutrino states and  $\Delta m_{12}^2 = m_1^2 - m_2^2$  is a difference of squares of masses of massive neutrinos  $\nu_1$  and  $\nu_2$ . The survival probability can then be expressed in terms of the neutrino's energy and the distance between its production and detection location  $L$ :

$$p_{\nu_e \rightarrow \nu_e}(L) = 1 - \sin^2 2\theta \sin^2 \frac{\Delta m_{12}^2 L}{4E}. \quad (1.12)$$

This formula is the fundamental oscillation formula which describes how the probability, that a neutrino produced in certain flavor can be detected as the same flavor, changes over the distance from the source. The oscillation length is  $L^{\text{osc}} = 4\pi E / \Delta m_{12}^2$ . It is often convenient to rewrite the expression in units more suitable for calculation,  $L^{\text{osc}} = 2.47 E [\text{GeV}] / \Delta m_{12}^2 [\text{eV}^2] \text{km}$ . In the same spirit the equation (1.12) turns into:

$$p_{\nu_e \rightarrow \nu_e}(L) = 1 - \sin^2 2\theta \sin^2 1.27 \frac{\Delta m_{12}^2 [\text{eV}^2] L [\text{km}]}{E [\text{GeV}]}. \quad (1.13)$$

The amplitude of the probability of oscillation is given by the mixing angle  $\theta$ . Of course, if there was no mixing of the massive states,  $\theta = 0$ , there would be no oscillation. On the other hand, if the mixing was maximal, i.e.  $\theta = \pi/4$ , then the electron neutrinos could not be detected at  $L/2 +$  multiples of the oscillation length.

### 1.3.2 3 flavor case

Derivation of formulae for oscillations of 3 neutrino species follows the same pattern as described above. The 2-neutrino example has shown that the probability of neutrino survival oscillates only if at least one neutrino is massive. Frequencies of the oscillations are proportional to the difference of squared masses and the amplitudes depend on the mixing angles. In the case of three neutrinos, there are 2 independent squared mass differences,  $\Delta m_{21}^2$ ,  $\Delta m_{23}^2$ , and three mixing angles,  $\theta_{12}$ ,  $\theta_{13}$ , and  $\theta_{23}$ , as already mentioned in Section 1.2.

The main difference from the 2-neutrino case is that an additional complex phase could make the mixing matrix complex in a non-trivial way and it would become a source of charge and parity transformation symmetry violation, or CP-violation. The phase is mostly denoted as  $\delta_{CP}$ . The other two phases used in the parametrization in Section 1.2,  $\Phi_1$  and  $\Phi_2$ , contribute to the “complexness” of the mixing matrix in such way that were neutrinos the Dirac particles, they would vanish by simple redefinition of the fields. If neutrinos were Majorana particles, however, the redefinition would not be possible, and the phases must be preserved.

On the other hand, the Majorana phases do not play any role in the neutrino oscillations as will be demonstrated now.

If one uses the  $U_{\text{PMNS}}$  matrix from (1.3) in the amplitude (1.7), the Majorana phases can be factored out  $U_{\text{PMNS}} = U' \cdot \text{diag}(e^{i\Phi_1}, e^{i\Phi_2}, 1) = U' \cdot \text{diag}(u_1, u_2, u_3)$ , and (1.7) is then described as

$$\langle \nu_\beta | \nu_\alpha(t) \rangle = \sum_i U'_{\beta i} U'^*_{\alpha i} u_i u_i^* e^{-iE_i t}. \quad (1.14)$$

The matrix  $U'$  now depends only on the mixing angles and the CP-phase. From the definition of  $u_i$ , it follows that  $u_i u_i^* = 1$  for each  $i = 1, 2, 3$ . The amplitude therefore is independent of the Majorana phases.

The  $U'$  mixing matrix is commonly used in calculations of oscillating probabilities of 3 neutrino species. Based on the expression (1.3), its elements can be written as:

$$U' = \begin{pmatrix} C_{12}C_{13} & S_{12}C_{13} & \hat{S}_{13}^* \\ -S_{12}C_{23} - C_{12}S_{23}\hat{S}_{13} & C_{12}C_{23} - S_{12}S_{23}\hat{S}_{13} & S_{23}C_{13} \\ S_{12}S_{23} - C_{12}C_{23}\hat{S}_{13} & -C_{12}S_{23} - S_{12}C_{23}\hat{S}_{13} & C_{23}C_{13} \end{pmatrix}. \quad (1.15)$$

The notation uses the same shortcut convention for the trigonometric functions of the mixing angles as in (1.3).

There is an ambiguity in definition of neutrinos  $\nu_i$ ,  $i = 1, 2, 3$ . Because of the history of the observations,  $\nu_1$  and  $\nu_2$  are neutrinos mainly involved in the Solar  $\nu_e$  deficit and the heavier neutrino is defined as  $\nu_2$ , and therefore  $\Delta m_{21}^2 > 0$ . Whether  $\nu_3$  is heavier or lighter than  $\nu_1$  and  $\nu_2$  has not been determined, yet. It is often called as the problem of neutrino mass hierarchy. The case in which  $m_1 < m_2 < m_3$  is called normal hierarchy (NH) and the case in which  $m_3 < m_1 < m_2$  is called inverted hierarchy (IH).

### 1.3.3 Electron antineutrino survival probability in three-neutrino mixing

To conclude this introduction on neutrino oscillations calculation, I will write the formula for the probability that an electron antineutrino produced in reactor core could be detected in a detector at time  $t$ ,  $p_{\bar{\nu}_e \rightarrow \bar{\nu}_e}$ . Substituting (1.15) for the mixing matrix in (1.9) yields:

$$p_{\bar{\nu}_e \rightarrow \bar{\nu}_e}(t) = 1 - 4 \left[ S_{12}^2 C_{12}^2 C_{13}^4 \sin^2 \frac{\Delta E_{12} t}{2} + C_{12}^2 S_{13}^2 C_{13}^2 \sin^2 \frac{\Delta E_{13} t}{2} + S_{12}^2 S_{13}^2 C_{13}^2 \sin^2 \frac{\Delta E_{23} t}{2} \right] \quad (1.16)$$

which can be rewritten in a more convenient form:

$$p_{\bar{\nu}_e \rightarrow \bar{\nu}_e}(t) = 1 - \sin^2 2\theta_{12} \cos^4 \theta_{13} \sin^2 \frac{\Delta E_{12} t}{2} - \sin^2 2\theta_{13} \cos^2 \theta_{12} \sin^2 \frac{\Delta E_{13} t}{2} - \sin^2 2\theta_{13} \sin^2 \theta_{12} \sin^2 \frac{\Delta E_{23} t}{2}. \quad (1.17)$$

Similarly to the two-neutrino case, it is more convenient to write the probability in a relativistic approximation and dependent on the traveled distance  $L$

$$p_{\bar{\nu}_e \rightarrow \bar{\nu}_e}(L) = 1 - \sin^2 2\theta_{12} \cos^4 \theta_{13} \sin^2 \left( \frac{\Delta m_{21}^2}{4E} L \right) - \sin^2 2\theta_{13} \cos^2 \theta_{12} \sin^2 \left( \frac{\Delta m_{31}^2}{4E} L \right) - \sin^2 2\theta_{13} \sin^2 \theta_{12} \sin^2 \left( \frac{\Delta m_{32}^2}{4E} L \right). \quad (1.18)$$

## 1.4 Neutrino mixing parameters

The mixing parameters have been measured by various experiments through observations of neutrinos and antineutrinos from various sources. The first evidence of neutrino mixing and the oscillation phenomenon came with observation of solar neutrinos in the Homestake Experiment by Ray Davis et al.[3] They measured smaller rate of  $\nu_e$  than predicted by John N. Bahcall[14]. The electron neutrinos produced inside the Sun core left the Sun in the second state (by definition) with definite mass  $\nu_2$ . The major role in this effect is played by the  $\theta_{12}$  and  $\Delta m_{21}^2$  and so these parameters are often called solar parameters.

The solar oscillation parameters were most precisely measured by the reactor neutrino experiment KamLAND which was located at an average distance of 180 km from many commercial power plants, where about 79% of neutrinos were contributed by 26 reactor cores at distances between 138–214 km[15]. The combination of the average distance and effective energy of the detected neutrinos  $\sim 4$  MeV made KamLAND be sensitive to the smallest squared mass difference.

Their final results were [16]

$$\begin{aligned}\sin^2(2\theta_{12}) &= 0.846_{-0.013}^{+0.014} \\ \Delta m_{21}^2 &= (7.53 \pm 0.18) \times 10^{-5} \text{eV}^2.\end{aligned}\tag{1.19}$$

The parameters  $\theta_{23}$  and  $\Delta m_{32}^2$  are often called atmospheric, because they play major role in oscillations of neutrinos from cosmic ray interactions in the atmosphere. These oscillations were first observed by the Kamiokande-II experiment[17]. The atmospheric parameters have been precisely measured by accelerator experiments, where the most sensitive is T2K[18]. The neutrinos from the production beam have average energy around 0.6 GeV and the detector is located 295 km away from the source. They measured

$$\begin{aligned}\sin^2(\theta_{23}) &= 0.514_{-0.056}^{+0.055} \text{ NH} \\ &= 0.511 \pm 0.055 \text{ IH} \\ |\Delta m_{32}^2| &= (2.51 \pm 0.10) \times 10^{-3} \text{eV}^2 \text{ NH} \\ |\Delta m_{13}^2| &= (2.48 \pm 0.10) \times 10^{-3} \text{eV}^2 \text{ IH}\end{aligned}\tag{1.20}$$

The results are slightly dependent on whether they assumed normal (NH) or inverted (IH) mass hierarchy.

Another accelerator experiment MINOS, although with baseline not at or near the maximum of the oscillation effect, measured of the squared mass difference with comparable precision[19]. Depending on the assumed mass hierarchy they measured the following values:

$$\begin{aligned}|\Delta m_{32}^2| &= (2.37 \pm 0.09) \times 10^{-3} \text{eV}^2 \text{ NH} \\ &= (2.41_{-0.09}^{+0.12}) \times 10^{-3} \text{eV}^2 \text{ IH}.\end{aligned}\tag{1.21}$$

In Review of Particle Physics, 2015 on-line edition[20], the authors presented their own fit to global data, that included both accelerator experiments and the results from Daya Bay[21]:

$$\begin{aligned}|\Delta m_{32}^2| &= (2.42 \pm 0.06) \times 10^{-3} \text{eV}^2 \text{ NH} \\ &= (2.49 \pm 0.06) \times 10^{-3} \text{eV}^2 \text{ IH}.\end{aligned}\tag{1.22}$$

None of the experiments is sensitive to the sign of  $\Delta m_{32}^2$ , and the ordering of masses of  $\nu_1$ ,  $\nu_2$ , and  $\nu_3$ , the mass hierarchy, remains unknown.

The parameter  $\theta_{13}$  was not measured due to its smallness until 2012 when Daya Bay[22], and shortly after RENO[23], reactor experiments measured non-zero  $\sin^2 2\theta_{23}$ . More about reactor experiments and namely about the Daya Bay results will be discussed in the Section 1.5.

I can conclude by saying that all the mixing angles and squared-mass differences have been measured, and that current and future experiments will improve the precision of these measurements. Oscillation parameters that have not been determined yet are the sign of  $\Delta m_{32}^2$  and the CP-violating phase  $\delta_{CP}$ .

## 1.5 Determining $\theta_{13}$ with nuclear reactors

Nuclear reactors are prolific sources of neutrinos as approximately 6 neutrinos are produced on average by each fission process. Fission reactions in reactor

produce neutrons and daughter nuclei many of which undergo  $\beta$ -decays producing  $\bar{\nu}_e$ , because they are rich in neutrons. There are four main fission components,  $^{235}\text{U}$ ,  $^{238}\text{U}$ ,  $^{239}\text{Pu}$ , and  $^{241}\text{Pu}$ , each producing  $\bar{\nu}_e$ s with different energy spectrum. Fraction of each is developing in time during the fuel burn. As a consequence, the energy spectrum of neutrinos in the flux from reactor is time dependent as well. The expected count rate in a detector, when no oscillations are considered, is proportional to the product of the distribution of neutrino energies and of the total cross section of inverse beta decay. These are plotted in Figure 1.1 as well as the expected count rate. The highest rate of interactions occurs for neutrino energies  $\sim 4$  MeV.

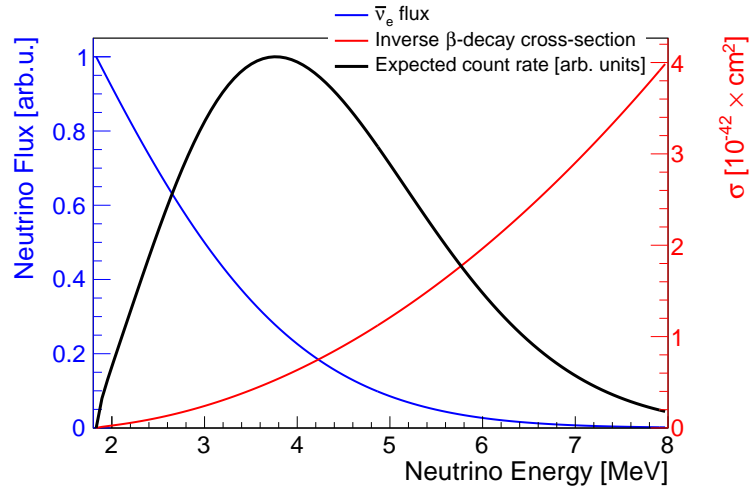


Figure 1.1: Reactor  $\bar{\nu}_e$  flux (blue), inverse beta decay cross section (red), and the spectrum of  $\bar{\nu}_e$  as observed in a detector. The flux and cross section have separate vertical axes. The final spectrum is plotted as an illustration with an arbitrary scale. The plot is based on the same plot in [24].

When considering neutrino oscillations, the probability that the produced antineutrino could also be detected in a detector at a distance  $L$  from the reactor is described by the equation (1.18). The values of  $\Delta m_{21}^2$  and  $\Delta m_{32}^2$  or  $\Delta m_{31}^2$  are very different therefore (1.18) can be split into parts:

$$p_{\bar{\nu}_e \rightarrow \bar{\nu}_e} = 1 - P_{12} - P_{13}, \quad (1.23)$$

where the amplitude of the term

$$P_{12} = \sin^2 2\theta_{12} \cos^4 \theta_{13} \sin^2 \left( \frac{\Delta m_{21}^2}{4E} L \right) \approx \sin^2 2\theta_{12} \sin^2 \left( \frac{\Delta m_{21}^2}{4E} L \right) \quad (1.24)$$

is determined by the mixing angle  $\theta_{12}$ , in contrast to the term

$$P_{13} = \sin^2 2\theta_{13} \cos^2 \theta_{12} \sin^2 \left( \frac{\Delta m_{31}^2}{4E} L \right) - \sin^2 2\theta_{13} \sin^2 \theta_{12} \sin^2 \left( \frac{\Delta m_{32}^2}{4E} L \right) \quad (1.25)$$

which strongly depends on the mixing angle  $\theta_{13}$ .

The survival probability weighted with the detected neutrino spectrum from Figure 1.1 is plotted in Figure 1.2 along with terms  $P_{12}$  and  $P_{13}$ . The separation

of the two terms (1.24) and (1.25) is clear in the picture. The first minimum is around 2 km from the reactor core. An experiment placed at this distance would maximally exploit the effect of the oscillation related to  $P_{13}$  and consequently  $\sin^2 2\theta_{13}$ .

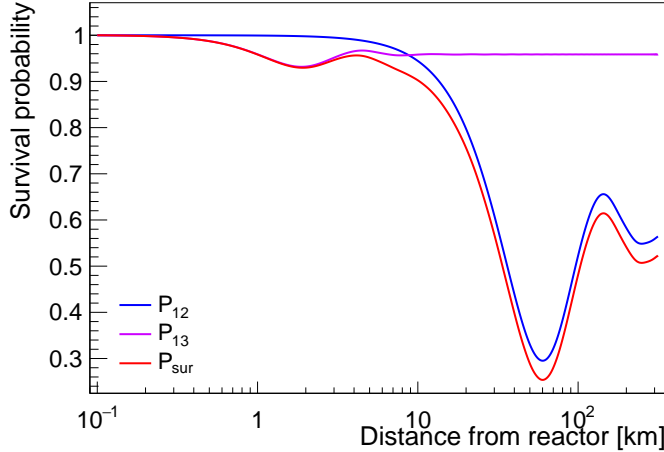


Figure 1.2: Survival probability of reactor electron antineutrino (red line). The probability in (1.18) is averaged over the energy spectrum of events observable in a detector as depicted in Figure 1.1. Contributions from the individual terms, defined by (1.24) and (1.25), with different oscillation frequency are also plotted (blue and violet line). The parameters used are  $\Delta m_{31}^2 = 2.4 \times 10^{-3} \text{ eV}^2$ ,  $\Delta m_{21}^2 = 7.5 \times 10^{-5} \text{ eV}^2$ ,  $\sin^2(2\theta_{13}) = 0.084$ , and  $\sin^2(2\theta_{12}) = 0.86$ .

There is a simplification in the formula (1.18) at and around the first minimum. The  $\Delta m_{21}^2$  is known to be smaller than the larger mass splitting by a factor of 30 and therefore  $\Delta m_{31}^2$  and  $\Delta m_{32}^2$  differ negligibly and (1.25) can be expressed using an effective squared-mass difference  $\Delta m_{ee}^2$ :

$$P_{13} \approx \sin^2 2\theta_{13} \sin^2 \left( \frac{\Delta m_{ee}^2 L}{4E} \right). \quad (1.26)$$

The effective parameter  $\Delta m_{ee}^2$  is related to the real mass splittings around the first minimum of  $P_{13}$  as[25]:

$$\Delta m_{ee}^2 = \cos^2 \theta_{12} |\Delta m_{31}^2| + \sin^2 \theta_{12} |\Delta m_{32}^2|. \quad (1.27)$$

## 1.6 Results of Daya Bay

The Daya Bay experiment completed commissioning of its 6 out of planned 8 detectors in December 2011, and started with physics data collection. In the configuration of 2 and 1 detectors in its near halls and 3 detectors in the experimental hall far from the nuclear reactors, it needed only 55 days of data to publish its first oscillation results[22]. Comparison of rates of electron antineutrinos in the near halls with the rates in the far hall evidenced a deficit which is consistent with the oscillation governed by the  $\Delta m_{32}^2$ . The non-oscillation hypothesis was excluded

at the level of 5.2 standard deviations. The mixing angle  $\theta_{13}$  was measured as  $\sin^2 2\theta_{13} = 0.092 \pm 0.016(\text{stat.}) \pm 0.005(\text{syst.})$ .

In the summer of 2012, two remaining detectors were installed, completing the final design of the experiment with 2 detectors in each of the near experimental halls and with 4 detectors in the far hall. Physics data taking restarted in October 2012.

The full period where only 6 detectors were installed provided 4 times more data than was used in the first oscillation analysis. With this extended data sample Daya Bay was able to compare not only rates, but also the shape of the measured energy spectrum of the antineutrino interactions[26]. Observed changes in shape in the far hall due to the oscillation allowed to measure an effective squared-mass difference  $|\Delta m_{ee}^2| = 2.59_{-0.20}^{+0.19} \times 10^{-3} \text{ eV}^2$ . Increased statistics and improved analysis yielded  $\sin^2 2\theta_{13} = 0.090_{-0.009}^{+0.008}$ .

Accumulated data of the full period with 6 detectors also enabled analysis of events where neutrons produced in the antineutrino inverse beta decays captured on hydrogen[27]. Such signal is more prone to backgrounds and does not achieve precision comparable to the main analysis with neutrons captured on gadolinium. On the other hand, both analyses share only minimum of systematic uncertainties. Daya Bay reported an independent result of the mixing angle  $\sin^2 2\theta_{13} = 0.083 \pm 0.018$  based on the alternative analysis.

After inclusion of data with all 8 detectors, Daya Bay reported  $\sin^2 2\theta_{13} = 0.084 \pm 0.005$  and  $|\Delta m_{ee}^2| = (2.42 \pm 0.11) \times 10^{-3} \text{ eV}^2$  which effectively started a precision measurement era for the two parameters[21]. The total number of analyzed events exceeded 1,200,000. With growing statistics, not only the statistical error reduces, but also the uncertainties related to backgrounds and detector effects are reduced. The independent analysis based on events with neutrons captured on hydrogen also results to the expanded data sample[28].

The experiment will continue with data collection beyond 2017. The uncertainty with which the parameters will be measured is expected to reduce to 0.003 and  $0.07 \times 10^{-3} \text{ eV}^2$  for  $\sin^2 2\theta_{13}$  and  $\Delta m_{ee}^2$ , respectively.

Although the Daya Bay experiment is designed for measurement of the oscillation parameters, the large amount of detected antineutrinos, especially in the detectors near the reactor cores, invites for detailed study of their absolute flux and of their energy spectrum. Daya Bay measured flux consistent with previous measurements from short-baseline experiments, however, it exhibits a deficit relative to predictions based on models of reactor core workings[29]. Moreover, the measured shape of energy spectrum deviates from the predictions in region of 4–5 MeV where an excess of events is observed with local significance of  $\sim 4\sigma$ .

The observed deficit of the total flux motivated searches for so called sterile neutrinos which, if they mixed with the neutrinos of the three known families, could explain the effect. Daya Bay exploited precision with which it measures the flux and energy spectrum of antineutrinos and set strong limits on the strength of the mixing in the range  $10^{-3} \text{ eV}^2 < |\Delta m_{41}^2| < 0.3 \text{ eV}^2$  of possible squared-mass differences[30].

The Daya Bay experiment has also become part of the global observational effort for supernova neutrinos. Highlights of the efforts can be found in [31].

## 1.7 Other Reactor $\bar{\nu}_e$ Oscillation Experiments

Two other reactor antineutrino oscillation experiments are currently in operation. Both have also measured the non-zero neutrino mixing angle  $\theta_{13}$ , although neither of them has reached the sensitivity and precision of the Daya Bay experiment.

### Double Chooz

The Double Chooz experiment is located in north-east France at the border with Belgium[32]. It detects electron antineutrinos from the Chooz Nuclear Power Station with total thermal power of 8.6 GW<sub>th</sub>. The experiment operates two identical antineutrino detectors of similar design as to Daya Bay's. One is located in the experimental hall of the late CHOOZ experiment[33] at distance about 1 km. The other one is placed in a new experimental hall at a near distance to the reactor cores. Relevant parameters of the layout and reactor and detector characteristics are listed in Table 1.1.

The far detector is not at optimal distance determined by the  $\Delta m_{32}^2$  which reduces sensitivity to the  $\theta_{13}$  mixing. Moreover, target mass of the detectors is 10 times smaller than the Daya Bay's and the total power of the cores is about half of the Daya Bay power plant. This limits their statistical sensitivity. Small overburden of the experimental halls also limits their sensitivity due to larger levels of cosmogenic backgrounds.

The experiment started in early 2011 with only the detector in the far hall operational. They reported indication of non-zero mixing angle  $\theta_{13}$  with rejection of no oscillation hypothesis at 94.6% C.L. [34]. The best result achieved with only one detector, i.e. without exploiting a relative measurement was  $\sin^2 2\theta_{13} = 0.090^{+0.032}_{-0.025}$  [35]. In January 2015, the experiment started running with both detectors operational. Relative measurement improved precision of determination of the mixing angle to  $\sin^2 2\theta_{13} = 0.111 \pm 0.018$  as reported in [36]. Since the statistics are now the limiting factor for Double Chooz (after 9 months of data with 2 detectors), further improvement is expected.

### RENO

The RENO experiment is located by the Hanbit Nuclear Power Plant (formerly Yeonggwang Nuclear Power Plant) on the west coast of South Korea[37]. The power plant operates 6 pressurized-water reactors, located in line spanning about 1.6 km. The experiment has located two detectors on the axis perpendicular to the line of reactors. Design of these detectors is similar to the one of Daya Bay and Double Chooz. The experimental parameters are listed in Table 1.1. As can be seen in the table, the experiment is by design less sensitive than Daya Bay in the measurement of the mixing angle  $\theta_{13}$  due to 5 times smaller target mass and 2 times shallower overburden.

The experiment started with physics data collection in 2011 with full configuration. They published their first result after collecting 220 days of data,  $\sin^2 2\theta_{13} = 0.113 \pm 0.013 \pm 0.019$ , and claimed exclusion of no-oscillation hypothesis at the level of 4.9 standard deviations[23].

With data collected over 500 days, the experiment could compare the shapes of energy spectra in the two detectors. The combined rate and shape analy-

Experiment	Reactor Thermal Power [GW <sub>th</sub> ]	Baseline Near/Far [m]	Target Mass Near/Far [ton]	Overburden Near/Far [m.w.e.]
DC	8.54	400/1050	8/8	120/300
RENO	16.8	290/1380	16/16	120/450
DB	17.4	360(480)/1910(1540)	2×40/80	250(265)/860

Table 1.1: Overview of parameters of the three reactor antineutrino oscillation experiments, Double Chooz (DC), RENO, Daya Bay(DB). The numbers for Daya Bay in parentheses are related to different reactor clusters and two near halls.

sis improved the measurement of the mixing angle  $\sin^2 2\theta_{13} = 0.082 \pm 0.009 \pm 0.006$ , and also yielded a value of the effective squared-mass difference  $\Delta m_{32}^2 = 2.62_{-0.23}^{+0.21}(\text{stat})_{-0.13}^{+0.12}(\text{syst})$  [38].



## 2. Atmospheric Muons from Cosmic Rays

In the past decades, there has been significant development and growth in number of underground experiments. Spectrum of problems they focus on is wide, from solar neutrino observations, through neutrino oscillation and neutrinoless double-beta decay measurements, to proton decay and Dark Matter searches. These experiments are interested in rare events, and therefore are very sensitive to small amounts of background.

Cosmic rays create large part of the background signals and the experiments focus on their shielding. There are two methods which are being employed to treat cosmic rays, proper passive shielding and active detection system which helps to veto related events.

The Daya Bay experiment is built underground with sufficient overburden that suppresses majority of cosmic rays. The only highly penetrating component that remains and produces background are muons. Daya Bay built two detection systems, RPC and water Cherenkov detectors, designed to detect these muons and to help to further reduce background in the antineutrino oscillation measurement.

Prediction of the total muon flux, together with their energy and directional distribution is necessary for evaluation of performance of the systems and also in analyses of particular backgrounds. In this work I used the predictions of muon fluxes to compare the expected rate of muon decays with the measurements presented here.

In the following parts of the chapter I briefly introduce primary cosmic rays and how they produce the penetrating muons in the atmosphere. In the next part I focus on cosmic rays at sea level and present formula for calculation of muon fluxes at sea level with respect to muon energy and incident angle. In the last part I discuss how the energy spectrum of muons qualitatively changes underground.

### 2.1 Cosmic Rays

History of cosmic ray observation starts at the beginning of the 20th century. In 1909, Theodor Wulf performed measurements of level of radiation on the ground and on the top of Eiffel tower. His observation of increase in the radiation level came as surprise and was not widely accepted at that time. Evidences of non-terrestrial sources of radiation started emerging slowly. In 1912, Victor Hess performed balloon measurements at an altitude over 5 km above sea level. His observation of four-fold increase in intensity relative to the sea level and his interpretation of the effect as an evidence for a very penetrative radiation entering the atmosphere from above earned him the Nobel Prize in Physics in 1936. Since the time our knowledge about cosmic rays has evolved significantly.

Particles that constitute the extraterrestrial radiation and reach the Earth atmosphere are called primary cosmic rays. Energy spectrum of the cosmic rays spans over many orders of magnitude. Mechanism of their production is yet unknown.

Composition of cosmic rays follows tightly the composition of nuclei abundant

in the universe. There are, however, nuclei observed in the rays that are not commonly seen in the cosmological objects, such as lithium, beryllium, and boron. This observation is explained by division of primary rays into two groups. The particles in the first group originate in the regular matter and are presumed to have been accelerated by an unknown mechanism. The second group consists of particles produced in interactions of primary rays with interstellar gas.

Primary cosmic rays are dominantly composed of protons. Helium, carbon, and oxygen follow. The observed spectra of these components are well modeled by power law in the energy region expanding from approximately 1 GeV to 100 TeV. Above this energy, the energy spectrum of cosmic rays exhibit two distinctive features. The first observed around energies of  $10^{15}$  eV and is commonly known as the knee. The slope of the spectrum steepens there. Second change is observed between  $10^{18}$  eV and  $10^{19}$  eV where the spectrum flattens, and it is referred to as the ankle. Neither of these features is, as of now, explained.

Cosmic rays are significantly affected by solar winds, and the intensity of incoming primary particles anti-correlated with solar activity with its 11-year period. Low-energy charged particles are affected by the geomagnetic field and the observed flux is then dependent on the location of the observer with respect to the field. This is especially true for rays with energies below about 10 GeV.

## 2.2 Production of Muons in the Atmosphere

When the particles reach the atmosphere, only a small fraction of them survive the propagation to the Earth surface. Energetic particles quickly initiate cascade interactions, often resulting in showers. The showers are usually composed of a hadronic core from the primary strong interaction and of an electromagnetic halo. The electromagnetic component is a product of decay of neutral pions into two gammas.

Important part of the hadronic showers constitute light charged mesons  $\pi^\pm$  and  $K^\pm$ . At the beginning of the initiated shower they have large energies and they interact strongly with air further developing the shower. When their energy reaches critical energy (115 GeV for  $\pi^\pm$  and 850 GeV for  $K^\pm$ ) where their interaction length equals their decay length, the development of the shower slows down.

Almost all charged pions and about 63.5% of kaons decay into muon and neutrino,  $\pi^\pm, K^\pm \rightarrow \mu^\pm + \nu_\mu(\bar{\nu}_\mu)$ . The maximum intensity of charged pions is around altitude of 15 km[20], where most of the muons are produced. Kaons, due to their higher critical energy and shorter decay length, start decaying earlier and produce harder muon spectrum.

## 2.3 Sea level

The composition reduces dominantly to muons and neutrinos at the sea level. There is a small fraction, by about 2 orders of magnitude smaller than muons, of electromagnetic showers and nucleons from the primary rays. The energy spectrum and angular distribution of muons is given by energies at the production,

by propagation through the atmosphere, and by their decay length which grows with energy.

Measurements show the spectrum is approximately flat for energies below 1 GeV. In range of about 10–100 GeV muon energies follow the power-law distribution of their parent pions. For higher energies, at which the interactions of parent pions start to dominate over their decay, the slope of muon spectrum becomes steeper.

Gaisser derived formula for the muon energy spectrum at the sea level[39]:

$$\frac{dN_\mu}{dE_\mu d\Omega} \approx \frac{0.14}{\text{cm}^2 \text{ s sr GeV}} \left( \frac{E_\mu}{\text{GeV}} \right)^{-2.7} \left( \frac{1}{1 + \frac{1.1E_\mu \cos \theta}{115 \text{ GeV}}} + \frac{0.054}{1 + \frac{1.1E_\mu \cos \theta}{850 \text{ GeV}}} \right), \quad (2.1)$$

where  $dN_\mu$  is the number of muons with energy in interval  $(E_\mu, E_\mu + dE_\mu)$  coming from solid angle  $d\Omega$  at zenith angle  $\theta$  and passing unit area in unit time. The formula reflects the fact that the spectrum tightly follows power-law distribution of the parent meson but one power steeper. It includes zenith angle dependence originating in different energy losses for different depths of the atmosphere in particular direction. The two terms in parentheses include contribution of muons from pion and kaon decays. Kaons are part of the hadronic core of the primary interactions and they decay faster than pions. Muons from these decays are often called prompt component. Formula (2.1) has limited validity in both, zenith angle and energy. For angles above  $70^\circ$  effects of the Earth curvature comes into play and the  $1/\cos \theta$  dependence for high energies is not valid.

Guan Mengyun et al.[40] modified the formula in (2.1) in order to extend its applicability to larger zenith angles and lower energies. They corrected the formula for curvature of the earth by using transformation of zenith angle at the point at sea level to zenith angle at the production point. Further more, they added correction for muon decays which become significant at low energies,  $E_\mu < 100 \text{ GeV}/\cos \theta$ . The final formula is then:

$$\begin{aligned} \frac{dN_\mu}{dE_\mu d\Omega} = & \frac{0.14}{\text{cm}^2 \text{ s sr GeV}} \left[ \frac{E_\mu}{\text{GeV}} \left( 1 + \frac{3.64 \text{ GeV}}{E_\mu (\cos \theta^*)^{1.29}} \right) \right]^{-2.7} \\ & \times \left( \frac{1}{1 + \frac{1.1E_\mu \cos \theta^*}{115 \text{ GeV}}} + \frac{0.054}{1 + \frac{1.1E_\mu \cos \theta^*}{850 \text{ GeV}}} \right), \end{aligned} \quad (2.2)$$

where  $\theta^*$  is the zenith angle of the muon direction at its production. The authors show that the modified parameterization form agrees well with measurements at energies below 100 GeV and for zenith angles larger than  $70^\circ$ .

## 2.4 Underground

Only muons and neutrinos can penetrate through dense matter and they are the only remaining components of cosmic rays underground. Muons lose their energy via continuous ionization and via discrete radiation processes. The total energy loss per unit distance traveled in rock can be approximately expressed by[39]:

$$\frac{dE_\mu}{dX} = -\alpha - \frac{E_\mu}{\xi}, \quad (2.3)$$

where both  $\alpha$  and  $\xi$  are, in general, functions of energy. The first term represents the continuous ionization losses and is slowly varying with energy and is often approximated by a constant  $\alpha \approx 2 \text{ MeV/g cm}^2$ . The other term represents energy loss due to radiation processes. These are bremsstrahlung,  $e^-/e^+$  pair production, and photonuclear interactions with hadrons. The energy  $\epsilon = \alpha\xi$ , beyond which the energy loss due to radiation becomes larger than the loss due to ionization, is called the critical energy and is approximately 500 GeV for muons in standard rock[39].

Assuming that parameters  $\alpha$  and  $\xi$  are only slowly varying with energy the relation between the initial energy at the surface  $E_{\mu,0}$  and the energy  $E_\mu$  after traveling distance  $X$  underground, the slant depth, is given by:

$$E_{\mu,0} = (E_\mu + \epsilon)e^{X/\xi} - \epsilon. \quad (2.4)$$

For shallow depths for which  $X \ll \xi \approx 2.5 \text{ km.w.e.}$ , it follows from Equation (2.4) that  $E_{\mu,0} \simeq E_\mu(1 + X/\xi) + \alpha X$ . The spectrum of  $E_\mu$  is flat at low energies  $E_\mu \ll \alpha X$  and it follows power-law of the spectrum at sea level at higher energies. On the other hand, when the depth is large,  $X \gg \xi$ , then  $E_{\mu,0} = (E_\mu + \epsilon)e^{X/\xi}$  and the spectral shape is again flat but the turning point where it starts following the slope of the surface spectrum,  $E_\mu = \epsilon$ , is independent of slant depth.

At very larger depths the suppression of atmospheric muons is so large that muons produced by charged current interaction of atmospheric neutrinos in the Earth become dominant. The intensity of such muons is observed to be constant with slant depths larger than about 16 kmw.e.[41].

The assumption of constant parameters  $\alpha$  and  $\xi$  is only an approximation and serves for qualitative description of properties of muon fluxes underground. Also, Equation (2.3) represents only mean energy losses and does not include stochastic nature of the processes behind it. For better predictions of muon fluxes in underground, experiments must rely on MC simulations that include full geometry of usually complex profile of the ground and simulate all known interactions of muons in the rock material.

This is also the case for the Daya Bay experiment. The formula in (2.2) is used as an input of muon fluxes at surface and their propagation through the mountain profile is simulated using specialized simulation software.

# 3. Experiment Daya Bay

The Daya Bay Reactor Neutrino Experiment, also referred to as the Daya Bay experiment, was designed and built to make a precision measurement of the mixing angle  $\theta_{13}$ . This was enabled by locating it near a prolific source of  $\bar{\nu}_e$ , a strong nuclear power plant, and by measuring relative differences in the detected flux at different baselines, one near the source and the other at around  $\sim 2$  km from the source. This short-baseline measurement of reactor antineutrinos is sensitive dominantly to the value of the  $\theta_{13}$  mixing angle. The relative measurement allows suppressing most of uncertainties related to the expected  $\bar{\nu}_e$  flux and the detection efficiency. These systematics are mostly correlated between reactor cores of the power plant and also between the detectors. As such, they play negligible role in the relative comparison.

The systematic uncertainty in the measurement of the mixing angle that is uncorrelated among the detectors was proved well below 1%. This precision has been achieved thanks to the identical design of the detectors, to their controlled filling with target liquids, as well as to the rich calibration programme. The experiment's cosmic ray veto system also plays an important role. It allows effective veto of dominant backgrounds.

## 3.1 Experimental Overview

The Daya Bay experiment is located at the Daya Bay nuclear power complex in Shenzhen, on the south-east coast of China, approximately 50 km north-east off Hong Kong. The complex comprises 3 nuclear power plants, Daya Bay, Ling Ao, and Ling Ao-II. Electron antineutrinos are produced in pairs of nuclear reactors of each power plant. The reactors are Pressurized Water Reactors (PWR) of type CPR-1000. Each of them generates nominally 2.9  $\text{GW}_{\text{th}}$  of thermal power, yielding the maximal thermal power output of the complex 17.4  $\text{GW}_{\text{th}}$ .

In the standard PWR reactors, the average energy release per fission is approximately 200 MeV. There are 6 antineutrinos produced in the chain after a fission on average. Therefore, a nuclear reactor with 1  $\text{GW}_{\text{th}}$  power output generates about  $1.9 \times 10^{20}$  antineutrinos every second. Day Bay power complex can generate up to about  $3 \times 10^{21}$  antineutrinos per second.

Eight detectors are located in three experimental halls. Two experimental halls, EH1 and EH2, are situated near to the Daya Bay and Ling Ao power plants, respectively. Each of the near halls hosts 2 antineutrino detectors. The 3rd hall, EH3, is located far from the reactors and it hosts 4 antineutrino detectors. Schematic diagram of the experimental site is in Figure 3.1. Distances of each experimental hall to the center of each power plant are listed in Table 3.1.

This layout enables to measure the  $\bar{\nu}_e$  flux near the reactor cores where it is nearly unoscillated and compare it to the flux measured at a distance close to 2 km, near the oscillation maximum.

All three halls are situated underground with adequate shielding against cosmic rays. This substantial amount of material attenuated rates of cosmic rays reaching the detectors by a factor of about  $10^2$  in the near halls and about  $10^4$  in the far hall. The total vertical overburden estimated in meters of water equivalent

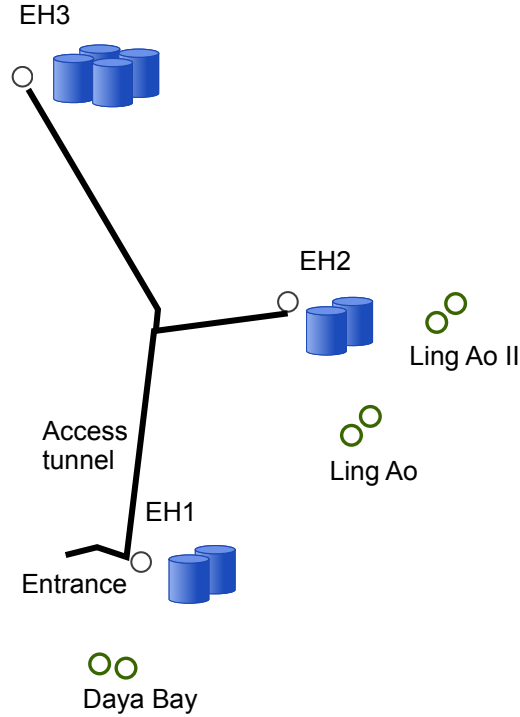


Figure 3.1: Layout of the site of the Daya Bay experiment. Locations of the detector halls and the reactor cores are marked with black open circles and open green circles, respectively. Underground access tunnel is also indicated.

	DB [m]	LA [m]	LA II [m]	Depth [m.w.e.]
EH1	360	860	1310	250
EH2	1350	480	530	265
EH3	1910	1540	1550	860

Table 3.1: Distances of each experimental hall to each pair of the reactor cores. The distances are measured from the center of each hall’s water pool to the center of the two cores and are rounded to 10 meters. Estimated vertical overburden of each hall in meters of water equivalent is given in the last column. Experimental halls are referred to as EH1, EH2, and EH3, which are the two near halls close to the Daya Bay and Ling Ao nuclear power plants and the far hall, respectively. The three power plants are denoted as DB, LA, LA II.

is listed in the last column of Table 3.1.

The experiment started data taking in 2011 with only 6 antineutrino detectors (AD) placed in the 3 halls. EH2 and EH3 were missing an AD each as compared to the final design. The remaining 2 ADs were installed in the summer of 2012, and the experiment has since continued measurements in the full design.

## 3.2 Experimental Hall

The antineutrino detectors are submerged in a water pool at each site. The water pool serves as a passive as well as an active shield against background radiations.

A substantial volume of water which separated the ADs from the pool walls by at least 2.5 meters reduced any natural radioactivity from the surrounding rock reaching the detector to a negligible level. It also attenuates fast neutrons originating in spallations initiated by cosmic ray muons.

The pools are instrumented with PMTs which are able to detect Cherenkov light produced in water by energetic charged particles. A barrier is created in each pool which divides it into two optically isolated regions, both instrumented with PMTs. Both parts serve as active vetoes of signals originating in the cosmic rays that penetrate all the way to the experimental hall.

Finally, there are layers of RPC detectors over the pools. They can serve as an additional veto system and aid tracking of detected muons.

An overall layout of an experimental hall is shown in Figure 3.2. Each of the detector subsystems will be described in more details in the following section.

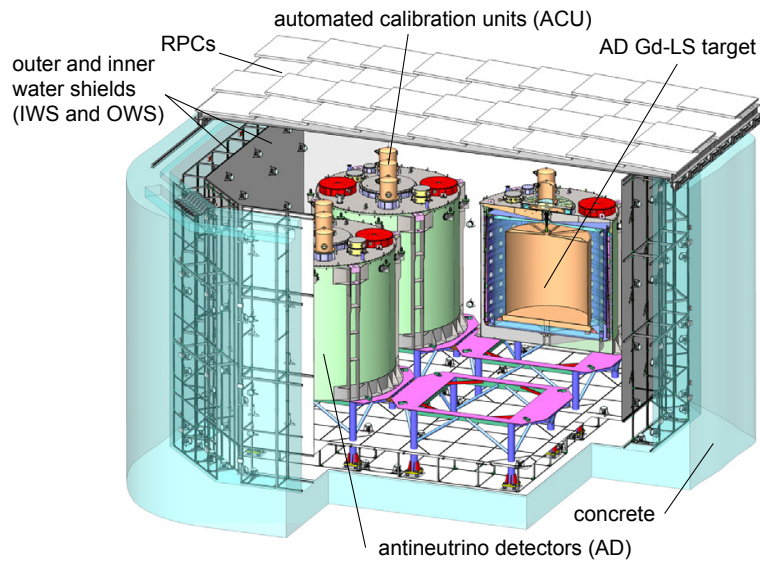


Figure 3.2: Schematic drawing of the far experimental hall. This drawing illustrates instrumentation of the far hall, where four detectors are placed in the water pool.

## 3.3 Antineutrino Detection

### 3.3.1 Detection Method

Detection of reactor antineutrinos has a long experimental history. In fact, the reactor antineutrinos were the first neutrinos observed in a detector in the 1950s by Cowan and Reines [2]. The method which was used then has not principally changed since.

The antineutrinos are observed in interactions with proton which turns into a neutron and a positron is emitted,

$$\bar{\nu}_e + p \rightarrow n + e^+. \quad (3.1)$$

This process is often called the inverse beta decay (IBD). The positron and neutron will produce two consecutive signals if the detector is designed properly.

The prompt signal comes from the positron's kinetic energy loss and its subsequent annihilation into two gammas which both contribute to the signal. The delayed signal occurs after the radiative capture of neutron on a nucleus in the material.

Reines and Cowan first used cadmium doping of liquid scintillator which served as a target in the experiment at Hanford[1]. In their improved measurement at Savannah River[2], they used water with dissolved cadmium as a target and sandwiched it with scintillators. Cadmium has large cross section to capture of thermalized neutrons, therefore most of the produced neutrons captured on Cd giving off around 9 MeV in series of gamma photons. The concentration of cadmium in the water solution was such that a characteristic capture time was around 5  $\mu$ s.

The Daya Bay experiment has followed this technique of delayed-coincidence selection, and doped its liquid scintillator with gadolinium. Neutrons produced in the IBD interaction have mean capture time around 30  $\mu$ s in such environment. Gadolinium de-excites after the capture via a cascade of gamma photons of total energy release of about 8 MeV.

The detector will be described in the following subsection.

### 3.3.2 Antineutrino Detector

The Daya Bay antineutrino detector (AD) was designed 1) to be modular so that multiple detectors could be placed in each experimental hall, 2) to be symmetric in order to avoid unnecessary complexities that would immediately bring in systematic uncertainties, 3) to be of low backgrounds so that high precision of the rare antineutrino interaction signal measurement was possible, and 4) to have high light output and collection efficiency so as to have a good energy resolution.

Each AD is a cylindrical stainless steel vessel with diameter and height of 5 m, which consists of three nested cylindrical zones. Figure 3.3 shows schematic drawing of a vertical cross section through the detector. The three zones are partitioned with two cylindrical acrylic tanks, drawn in blue and red in the picture.

The central region in the inner acrylic vessel (IAV) is filled with gadolinium-loaded organic liquid scintillator (GdLS). It has height and diameter of approximately 3 meters. Gadolinium was added in form of dissolved salt  $\text{Gd}(\text{TMHA})_3$ , where TMHA is 3,5,5-trimethylhexanoic acid. Concentration of gadolinium is 0.1% by weight. Thanks to the doping, most of the neutrons from IBD interactions in the volume undergo capture on gadolinium. This volume serves as the antineutrino target for the Daya Bay's main analyses.

More details on production of the gadolinium-loaded liquid scintillator can be found in a dedicated paper [42].

The middle layer is filled with pure liquid scintillator (LS), i.e. without the gadolinium doping. It aids the detection of gammas that escape from the target volume. The scintillator is contained in an outer acrylic vessel (OAV), which has diameter and height of approximately 4 meters.

Scintillator in both regions is made of linear alkylbenzene with fluor. 2,5-Diphenyloxazole (PPO) was used as the fluor in concentration of 3 g/L. Wavelength shifter was also added (15 mg/L of 1,4-Bis(2-methylstyryl)benzol—bis-MSB) to shift wavelength of the scintillation light to the range where the scin-

tillator becomes transparent. The emission spectrum of GdLS filtered by its transmission through the scintillator peaks in the 400–450 nm range which is well within good acceptance of photo multipliers used for the light detection.

The scintillation light produced in the scintillator volume is detected by 192 photomultiplier tubes (PMT) with 8 inch in diameter (Hamamatsu R5912, [43]). The PMTs are mounted on eight ladders installed along the circumference of the steel tank. The layer between the steel tank and the outer acrylic vessel is filled with transparent mineral oil. Mineral oil ensures better optical homogeneity thanks to an index of refraction similar to the liquid scintillator. It also shields sensitive volumes with scintillators from radiation that originates mainly from  $^{137}\text{Cs}$  in the PMTs and from U/Th chain in the stainless steel tank and the support ladders.

The dimensions of acrylic vessels and densities and weights of respective liquid volumes are listed in Table 3.2.

	Height [m]	Diameter [m]	Mass [t]	Mass of liquid [t]	Density [g/mL]
IAV	3.1	3.12	0.91–0.97	19.9	0.860
OAV	3.98	4	1.81–1.99	21.6	0.859
SSV	5	5	24	36.4	0.851

Table 3.2: Dimensions and weights of the three containers in the antineutrino detector. Masses and densities of the contained liquids are also listed. The liquids are GdLS, LS, and MO, respectively.

Daya Bay antineutrino detectors were designed with two reflective panels which were mounted at the top and bottom of the OAV, they are also labeled on the section picture of AD in Figure 3.3. The reflectors provide more efficient light collection and therefore reduce the number of PMTs needed while keeping the effective photocathode coverage. The reflectors are circular with 4.35 m diameter. Their reflective component is 3M<sup>TM</sup> Enhanced Specular Reflector which is sandwiched in between two sheets of acrylic.

## Calibration System

Important part of the antineutrino detection system is its calibration.

An automated calibration system has been designed in order to allow proper calibration, and evaluation and monitoring of performance of the scintillator, individual PMTs, and the overall detector energy scale. The system consists of three separate units (ACU as for Automated Calibration Unit) with retractable calibration sources. The units are positioned on top of each detector. One is located at the central axis of the detector, another two are located at 135 cm and 177 cm off axis at opposite sides of the central ACU. The central unit and the one at 135 cm are located above the GdLS region and its sources can be deployed vertically there. The third unit is located at the side of the GdLS region and services the LS region. The calibration units are connected with the GdLS and LS volumes with Teflon bellows that create shafts from the unit to ports in IAV and OAV. The calibration units and the respective bellows and ports are depicted in Figure 3.3.

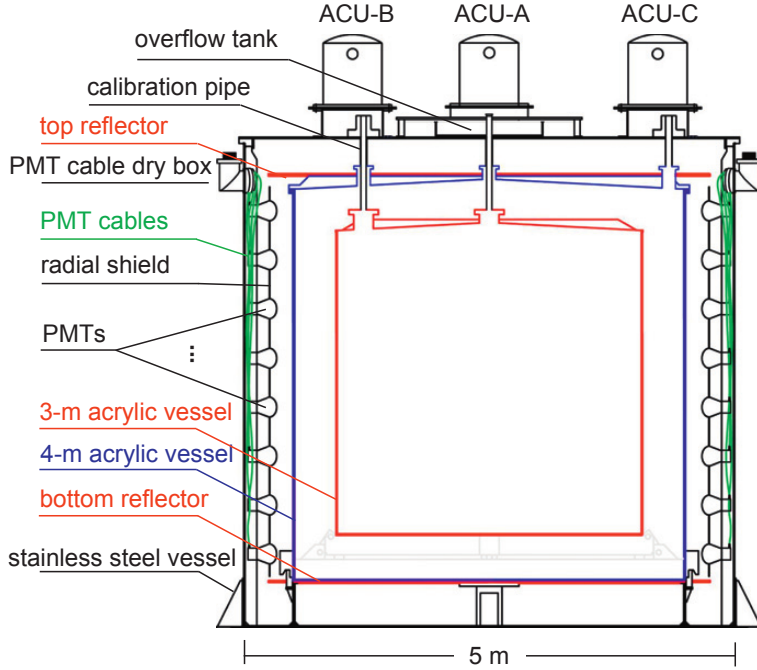


Figure 3.3: Drawing of vertical section of the AD.

By design, each ACU hosts 4 sources: 1. Am-C neutron source which allows calibration of the detector energy scale to the energies from neutron captures, and also helps with determination of the fraction of captures on gadolinium; 2.  $^{68}\text{Ge}$  positron source which produces two annihilation gammas; 3.  $^{60}\text{Co}$  gamma source with its chain decay with release of two gammas, 1.17 MeV and 1.33 MeV. 4. LED source which served as source of low levels of light and allowed measurement of PMT gain.

The Am-C neutron sources cause correlated signals which also add to antineutrino signal background. This background is negligible in the near halls, but becomes significant at the far hall due to the much lower signal rate. This correlated background reaches levels similar to the dominant background from  $^9\text{Li}/^8\text{He}$  cosmogenic isotopes. During a summer shutdown in 2012 when additional 2 ADs were installed in EH2 and EH3, the Am-C calibration sources were removed from the two off-axis calibration units in all detectors in EH3.

Detailed description of the calibration system is given in [44].

### 3.4 Muon Veto System

The detectors in each experimental hall are placed inside water pools. The water pools serve as effective shielding against radioactivity from the surrounding rock and against neutrons produced in the rock by cosmogenic muons. The pools are divided into two optically separated regions, inner water shield (IWS) and outer water shield (OWS), each of which is instrumented with PMTs and works as an independent Cherenkov detector of cosmic ray muons. The pools are covered with multi-layered resistive plate chambers.

Each of the subsystems is described in the following two subsections.

### 3.4.1 Water shield

The water pools, which host ADs in each hall, have octagonal base which is illustrated in Figure 3.4. The pools in both near halls are 10 m wide, 16 m long, and 10 m deep. The pool in the far hall has the same depth but a larger symmetric base 16 m by 16 m.

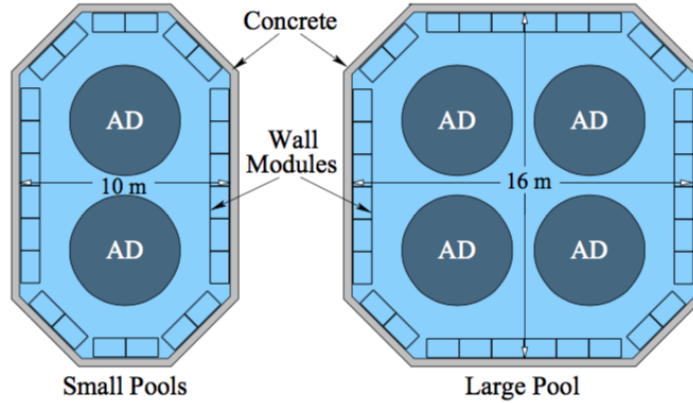


Figure 3.4: Top-view drawing of water pools of near and far halls.

Stainless steel structure is built in modules along the walls and at the bottom of the pool. It creates a 1-m padding around the walls and from the floor. Tyvek<sup>®</sup> multi-layered film is used to separate the stainless steel structure from the wall and also from outside of the structure. This way, two optically separated parts of the pool are created, IWS and OWS. PMTs are mounted onto the structure so that they are facing horizontally outwards from the center in the outer part, and inwards to the center in both the outer and inner part. See the pool partitioning and PMT instrumentation in Figure 3.2.

In total, 288 PMTs are mounted in each near hall and 384 in the far hall. The parts of water pool, IWS and OWS, instrumented with the PMTs create two separate active Cherenkov detectors. Numbers of PMTs used for each partition are listed in Table 3.3.

Hall	IWS	OWS (inward/outward)	Total
EH1	121	167 (103/64)	288
EH2	121	167 (103/64)	288
EH3	160	224 (128/96)	384

Table 3.3: Numbers of PMTs installed in each water pool of near and far halls, EH1, EH, EH3.

PMT signal processing followed the same design as in the case of ADs which will be described in Section 3.5. Readout of signals from the PMTs of each detector was triggered if either PMT multiplicity, a number of PMT signals over threshold (set to an equivalent of 0.25 p.e.), was above preset level, or if the total charge seen by the detector crossed a preset threshold. The trigger conditions are listed in Table 3.4.

Hall	Pool	Multiplicity threshold ( $\geq$ )	Total charge threshold
EH1	IWS	6	8.9 mV (1.8 pe)
	OWS	7	10.0 mV (2.0 pe)
EH2	IWS	6	8.9 mV (1.8 pe)
	OWS	7	10.0 mV (2.0 pe)
EH3	IWS	6	12.2 mV (2.4 pe)
	OWS	8	14.4 mV (2.9 pe)

Table 3.4: Conditions for trigger of data readout from the Cherenkov detectors.

The purpose of the Cherenkov detectors is to detect cosmic rays which pass through or near by the antineutrino detectors. Their efficiency in doing so is therefore an important quantity.

Data from the period where only 6 ADs were installed in total, from December 2011 through July 2012, were analyzed and the performance of the WS detectors evaluated[45]. Figure 3.5 shows distribution of PMT multiplicity in each hall. There is a steep slope below multiplicity of 20 which is attributed to noises in electronics and natural radioactivity from the PMTs themselves and from the surrounding rock. Above the multiplicity of 20, triggers from cosmic rays become dominant.

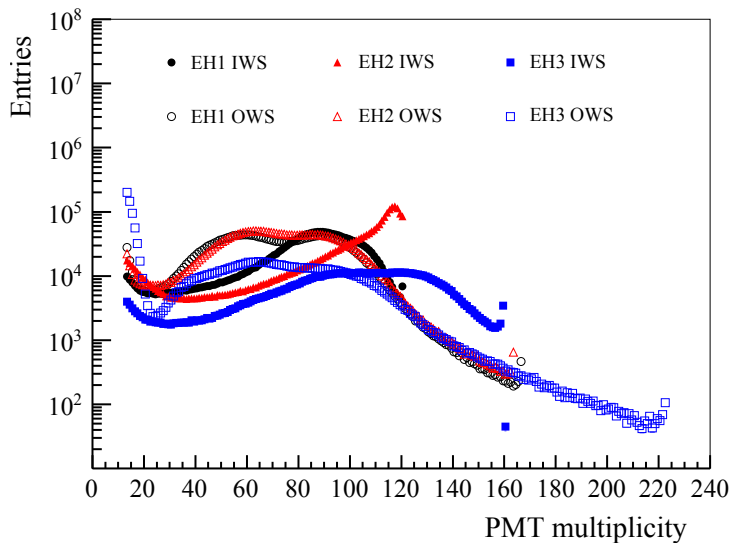


Figure 3.5: Distribution of PMT multiplicity per trigger of Cherenkov detectors in all three halls.

Efficiency of the water pool was determined based on measurements of muons which also triggered readouts in AD. This AD-muon efficiency was defined as ratio of the number of coincident muon triggers in Cherenkov detector and AD to the number of all muon triggers in AD. The AD trigger was called an AD muon if reconstructed energy in AD was greater than 20 MeV. In water shield detectors, the muon trigger was defined as having multiplicity greater than 12 PMT.

IWS efficiency of detecting the AD muons was consistent among all three

halls and was identified as being  $99.98 \pm 0.01\%$ . Although simulations suggested that it should be 100% for true AD muons. This slight decrease in measured efficiency is attributed to fast neutrons that were generated outside the water pool and deposited substantial amount of energy in AD without leaving signal in the water shield.

OWS efficiency to the AD muons was measured lower, at around  $\sim 97\%$  in the near halls and  $\sim 99\%$  in the far hall. This is mainly due to the geometry of the outer pool region. It does not cover the top of the pool, therefore, muons traveling from the top and stopping in the AD or in the IWS do not produce any signal in the OWS. This effect was confirmed with MC simulations. The relatively higher measured efficiency in the far hall is due to the higher mean energy of the muons. Majority of the muons pass completely through the water pool and leave signals in both veto detectors.

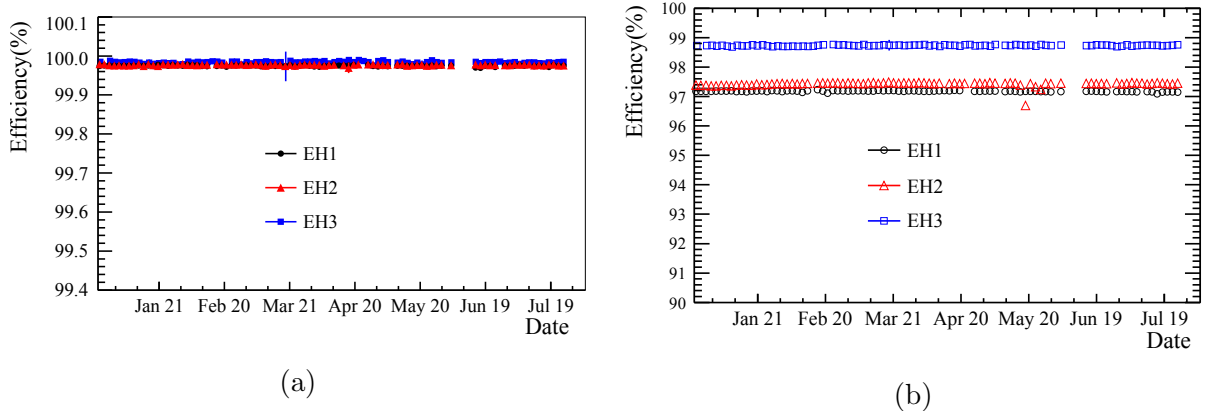


Figure 3.6: Efficiencies of Cherenkov detectors to AD muons as they were measured from December 2011 through July 2012 when the experiment was running in the configuration with only 6 ADs. IWS (a) has higher measured AD muon detection efficiency due to the fact that every muon, which passed AD must have passed IWS too. OWS (b) exhibit different efficiencies in the near and far halls because of higher mean energy of muons in the far hall.

### 3.4.2 RPC

Resistive plate chambers (RPCs) are gaseous particle detectors that consist of two resistive planar electrodes separated by a gas gap. RPCs were chosen as complementary cosmic ray detectors because of their capability to cover large areas at relatively low cost as compared to, for example, plastic scintillators.

The whole detector system is built from modules with area of about 2.2 m by 2.2 m and with 8 cm in height. Each module contains 8 bare RPCs stacked in four layers. The bare-RPC layers are read out utilizing copper readout strips which are cross-aligned in different layers allowing two-dimensional reconstruction. Strips are 26 cm wide. More details about the bare chambers and the built of modules will be discussed in Chapter 4.

The RPC modules were laid on a steel support structure in a staggered pattern such that there is 10 cm overlap between neighboring modules to minimize dead regions. To allow the overlap, RPC modules are tilted in  $3^\circ$  angle. The RPC

support structure (in Figure 3.7a) is installed on rails, so that the system can be rolled away to allow access to the pool. There are  $6 \times 9$  modules in each of the near halls, and  $9 \times 9$  modules in the far hall. The whole platform exceeds each side of the pool by 1 m.

Two RPC modules were specially installed in each experimental hall to form RPC telescopes. These modules are about 2 m above the RPC array in the middle of opposing sides of the pool, and partially overlap the RPC array. The height and vertical overlap vary from hall to hall. Muons that pass through both, the telescope and the main RPC array, can be tracked. The two RPCs installed in the far hall are shown in the photo in Figure 3.7b.

Although RPCs were not directly used as veto detectors in oscillation analyses, they were used in supplemental studies of cosmic ray induced backgrounds.

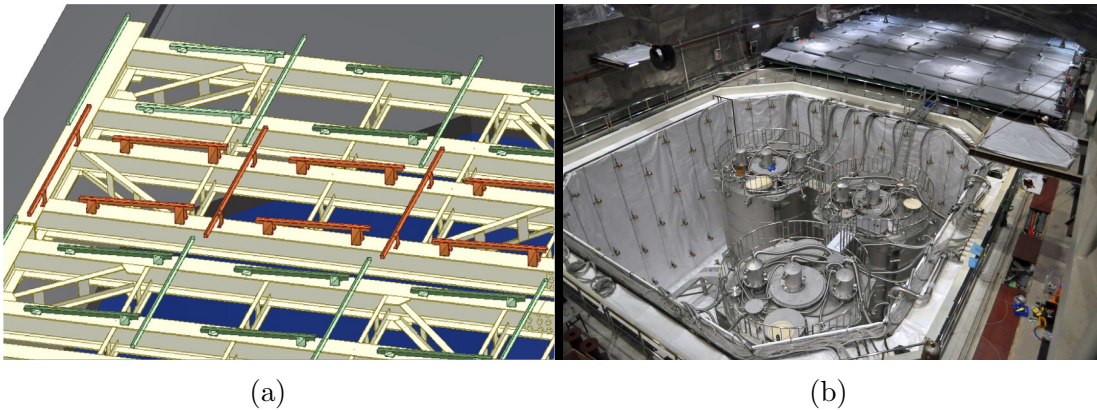


Figure 3.7: (a) Support frame for RPC modules. The supporting rails have  $3^\circ$  tilt and alternating height from column to column so they allow staggering of the modules with overlaps. (b) Photo of the far hall during installations. RPC system is moved away from the water pool. Two telescope RPCs are installed on each side of the hall on suspended platforms.

Readout of RPC data is triggered when at least 3 out of 4 layers in a module have signals. I will denote this trigger condition as “3/4 trigger” and, similarly, I will denote trigger where all four layers had hits as “4/4 trigger”. 4/4 triggers therefore create a subset of 3/4 triggers. Integration of the data acquisition of RPC system with the PMT-based systems will be discussed in Section 3.5. Detailed discussion of RPC triggering will be covered in Chapter 4.

Efficiency of each module can be calculated from real data utilizing the layer structure. Layer efficiencies are first calculated from comparison of rates of 3/4 and 4/4 triggers. These efficiencies are then combined and efficiency of the module can be calculated for each trigger condition.

Efficiencies of RPCs varied over time due to their sensitivity to the environmental conditions. The conditions underground followed seasonal variations of humidity and pressure. Both have impact on RPC performance. In order to improve stability of the performance, modules were flown with dry air.

Another indicator of performance of RPC is noise rate, i.e. rate of signals above threshold which were not initiated by the cosmic rays. Noise rate of each layer was calculated from random triggers, where RPC system in each hall was readout randomly and module layers were searched for signals. Figure 3.8 shows

calculated average layer noise rate in each hall. An overall decrease can be observed which is attributed to stabilization of the bare chambers. The large jump in March 2012 is due to an increase of applied HV. After noise rate and currents settled at low enough values, the voltage was increased from 7.4 kV to 7.6 kV in order to improve the system’s muon detection efficiency.

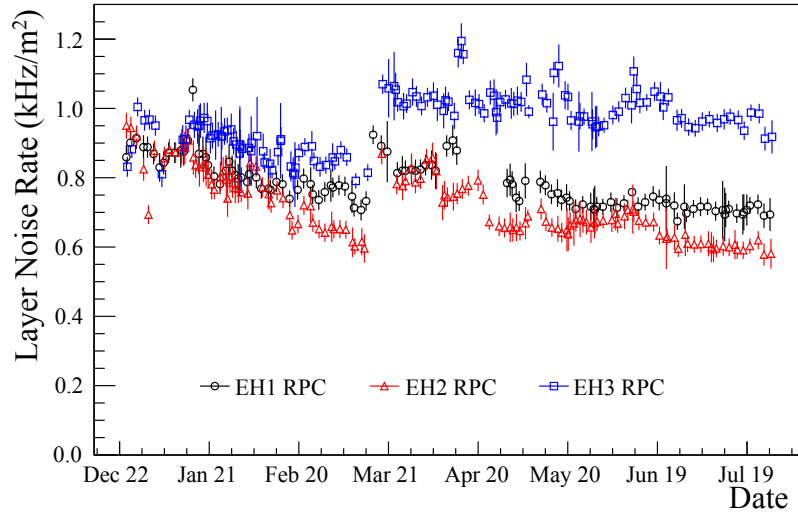


Figure 3.8: Average noise in RPC modules’ layers in each hall. Jump in the end of December 2011 is a result of dry air flow through the RPC modules. Jump in March 2012 is due to increase of applied HV from 7.4 kV to 7.6 kV.

## 3.5 Data Acquisition and Trigger

The experiment’s data acquisition (DAQ) system is partitioned at two levels. The lowest division is by the detector types. Each AD, IWS, OWS, and RPC manage their data readout separately. In each hall, data from each subsystem are merged. PMT-based systems—ADs, IWS, and OWS—share the same readout design, whereas RPCs implemented their own.

### 3.5.1 PMT-based detectors

Raw PMT signals are processed by front-end-electronics modules (FEE) which are located in a designated area in each hall. Each FEE module can process 16 PMT channels. The output of each FEE module is the number of channels over a preset threshold, analog sum all 16 channels, and pairs of digitized amplitude (ADC) and time information (TDC) for each PMT.

Number of hit channels and the analog sum of the signals is sent to a local trigger board (LTB) which combines the information from all used FEE modules of an AD and makes decision whether to read the data out. If either the combined analog charge  $E_{\text{sum}}$  or the total number of channels with signal  $N_{\text{hit}}$  exceeded predefined limits (equivalent to 65 photo-electrons for  $E_{\text{sum}}$  and 45 channels for  $N_{\text{hit}}$ ) a trigger was sent back to FEE and the data are read out.

The detector system and its readout electronics is described in more detail in [46].

### 3.5.2 RPC

Each RPC module is equipped with front-end-electronics card (FEC) which is responsible for: 1) digitization of signals from individual readout strips; 2) decision on local trigger condition; 3) preparation of the digitized data for sending out to the acquisition system. An analog signal of each readout strip is translated into binary data, either it crossed a predefined threshold or it did not.

Each FEC is connected to readout transceivers (ROT). ROT serves as a communication station which collects data from up to 15 FECs via twisted pair electronic cables and transmit them via optical fiber to master electronics boards, readout module (ROM) and readout-trigger module (RTM). There is one RTM and one ROM in each hall and they provide an interface with the global acquisition system.

FEC processes signals in its 32 channels and sends out local triggers if 2, 3, or all 4 layers in the module have hit. The information on how many layers were hit is sent to RTM. It is configured to trigger data readout in corresponding module if the 3/4 trigger condition was satisfied.

## 3.6 Antineutrino Signal

As mentioned in Section 3.3.1, reactor antineutrinos have been detected via inverse  $\beta$ -decay reaction (3.1), where two signals are generated in the detector. Positron carries most of the neutrino energy lowered by the difference between the masses of neutron and proton and the recoil of the neutron:

$$E_{e^+} = E_{\bar{\nu}_e} - 1.293 \text{ MeV} - E_{\text{recoil}}. \quad (3.2)$$

After depositing all of its kinetic energy in the detector, the positron annihilates and gives out another energy in the form of the annihilation gammas. Total energy deposition in this prompt part of the event is then

$$E_p = E_{\bar{\nu}_e} - 0.782 \text{ MeV} - E_{\text{recoil}}. \quad (3.3)$$

The delayed signal comes from the capture of the neutron on gadolinium after which the gadolinium de-excites with a cascade of gammas totally releasing about 8 MeV. There are two isotopes of gadolinium naturally occurring with significant cross section for neutron capture, they are  $^{157}\text{Gd}$  and  $^{155}\text{Gd}$ , with the former one having about four times larger neutron capture cross section. The natural abundance of the isotopes, the neutron capture cross sections, and the amount of energies released after the capture are listed in Table 3.5. For comparison, values for hydrogen are also added. The Daya Bay experiment also provided results of the antineutrino oscillations analyzing a sample of inverse beta decays (IBD) where the delayed signal originated in neutron capture on hydrogen [28].

Different methods were used for the oscillation analysis over time in order to provide ground for cross-check. Each of the methods used slightly different selection criteria. In the following, I will give an overview of the selection basics. The criteria are summarized in Table 3.6 with the concrete values as published in [21].

The mean capture time of neutrons in GdLS with 0.1% of gadolinium is  $\sim 30 \mu\text{s}$ . Pairs of signals in AD were required to have time separation in the

isotope	abundance	$\sigma_{(n_{th},\gamma)}$	$E_\gamma$
$^1\text{H}$	$\sim 100\%$	0.329 b	2.22 MeV
$^{155}\text{Gd}$	14.80%	60,700 b	8.54 MeV
$^{157}\text{Gd}$	15.65%	254,000 b	7.94 MeV

Table 3.5: List of neutron capture cross sections of two gadolinium isotopes with highest capture rates. Natural abundance of each is listed together with full de-excitation energies. For comparison, hydrogen is also listed.

interval from 1  $\mu\text{s}$  to 200  $\mu\text{s}$ , which I will call  $\Delta T$  cut. Distribution of prompt and delayed energies is plotted in Figure 3.9. Region of IBD events where the neutron was captured on gadolinium is well visible around 8 MeV in delayed energy. IBD events with neutrons captured on hydrogen are also visible as a band at around 2.2 MeV in delayed energy. These are, however, overwhelmed by accidental backgrounds at low prompt energies.

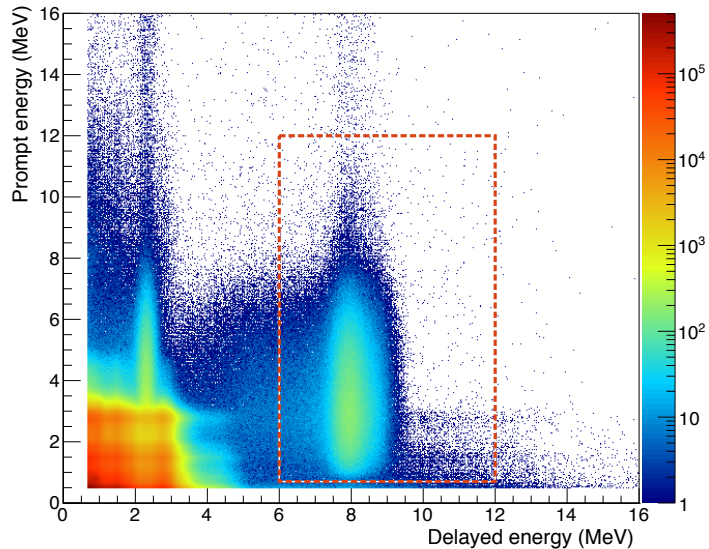


Figure 3.9: Distribution of prompt and delayed reconstructed energies for pairs of signals within the selection time window (1,200)  $\mu\text{s}$  and after application of muon veto and multiplicity cut. The energy based selection of IBD events is highlighted with the red dashed-line rectangle.

The high energy deposit of gadolinium capture of neutrons allows to remove most of accidental coincidences by application of cut on the delayed energy. The rate of non-IBD events which produce signals with energies around 8 MeV reduces dramatically. Figure 3.10 shows the distribution of delayed energy of IBD events. Delayed energy selection criterion of 6–12 MeV is chosen so that reasonable efficiency is kept while accidental background stays low. Types of backgrounds will be discussed in the following section.

The selection criterion for the prompt energy is set to 0.7–12 MeV range, in order to cover the full spectrum of energies of the IBD interaction. The lower

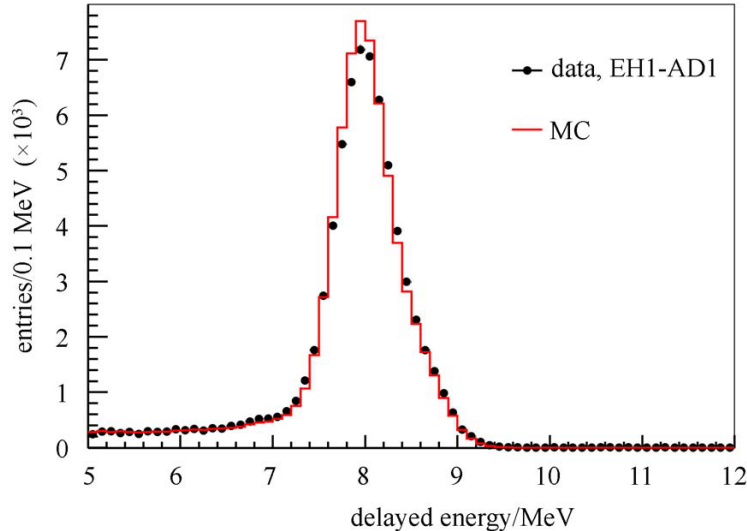


Figure 3.10: Example distribution of delayed energy of the selected IBD events, after application of  $\Delta T$  cut, muon veto, and multiplicity cut. Accidental backgrounds were subtracted. The peak at around 8 MeV from de-excitation of gadolinium nucleus after neutron capture is prominent. The tail at low energies is also visible, which is due to the escape of gammas out of liquid scintillator. The shape of the peak and of the tail agrees well with the MC simulations plotted here in red line. The plot was taken from [47].

bound is below the minimal energy deposition through the annihilation gammas to include signals with energy losses out of the scintillating region and distorted by the resolution of the detector.

In order to reduce backgrounds related to cosmic rays, which are muons or muon induced particles, IBD candidates are rejected if the delayed signal is close to the identified cosmic ray. Majority of muons passing through AD produced signals with mean reconstructed energy around 1 GeV. Any event with reconstructed energy above 20 MeV is considered a muon interaction in AD and the veto time for any IBD delayed signal candidate is set to 1 ms. Small fraction of cosmic ray events produce large amount of light in the detectors. These are interpreted as cosmic ray-induced showers. These showers are more likely to produce backgrounds and therefore a longer veto time of 1 s is applied after events with reconstructed energy above 2.5 GeV.

Even when muons do not deposit energy in the scintillator, they can interact in the neighborhood and produce neutrons. These neutrons then find their way into GdLS and contribute to the background. These muons are effectively identified by the water shield detectors. Veto time is set to  $(-1,600) \mu\text{s}$  around a signal in either the inner or outer water shield which caused more than 12 PMT signals to cross a preset threshold. The allowance for the signal in AD to come even before the signal in the water shield is due to different detector latency.

Sometimes, an accidental overlap of uncorrelated events with an IBD signal occurs. In order to prevent ambiguity in selection of the prompt and delayed signal, the pair is required to be isolated from any other candidates, i.e. no other prompt-like signal occurs in  $200 \mu\text{s}$  before the prompt signal, between the prompt and delayed signal, or  $200 \mu\text{s}$  after the delayed signal.

The criteria described above are summarized in Table 3.6.

	Selection criterion
$\Delta T$	(1, 200) $\mu\text{s}$
Prompt energy	(0.7, 12) MeV
Delayed energy	(6, 12) MeV
AD muon veto	Veto (-2 $\mu\text{s}$ , 1 ms) after $> 20$ MeV signal
AD shower veto	Veto (-2 $\mu\text{s}$ , 1 s) after $> 2.5$ GeV signal
Water shield veto	Veto (-2, 600) $\mu\text{s}$ after $N_{\text{hit}} > 12$ in OWS or IWS
Multiplicity veto	No signal $> 0.7$ MeV 200 $\mu\text{s}$ before prompt No signal $> 0.7$ MeV 200 $\mu\text{s}$ after delayed

Table 3.6: IBD selection criteria as applied in [21].

## 3.7 Backgrounds

The signal background of the Daya Bay experiment can be divided into 2 main categories—uncorrelated and correlated. Uncorrelated background consists of an accidental coincidence in time of two unrelated events which can together mimic the antineutrino signal. Correlated background is caused by one event with two signals of correlated origin separated in time similarly to the antineutrino signal.

### 3.7.1 Uncorrelated Background

Although the rate of uncorrelated individual signals is relatively high, only small fraction created a pair which satisfies the antineutrino selection criteria. Most of these signals that satisfy the delayed energy selection are  $\beta$ -decays of isotope  $^{12}\text{B}$ . The isotope is abundantly created in the detector by interactions of cosmic rays and it escapes veto because of its long half-life of 20.2 ms. In total, the uncorrelated background contributes only about 1% of the signal in the detectors of the near halls and about 2% in the far hall. The contribution is estimated precisely using measured rates of individual uncorrelated signals and is subtracted from signal with minor uncertainty.

### 3.7.2 Correlated Background

The correlated backgrounds are dominantly caused by interaction of cosmic rays in the detectors or in their vicinity. They can produce free neutrons and unstable isotopes. Signals from the cosmic rays themselves, decays of the unstable isotopes, and captures of the free neutrons can combine to create an IBD-like event. However, the cosmic rays which cause them, leave a trace in the ADs and the veto system, and, therefore, such events can be effectively vetoed.

Another background caused by cosmic rays are so called fast neutrons. Cosmic rays can interact outside the antineutrino detectors and create neutrons with large energies. These neutrons can penetrate into AD and their collisions with protons of the scintillator can create a prompt-like signal. They lose their energy

in these collisions and consequently are captured creating a delayed-like signal. Efficient identification of the cosmic rays by the veto system allows to reduce this background to events where the neutrons are created in the rock surrounding the water pool of each hall.

Some of the unstable isotopes created by the cosmic rays in the detectors are rare  ${}^9\text{Li}$  and  ${}^8\text{He}$ . They have relatively long half-life, 178.3 ms and 119.1 ms for  ${}^9\text{Li}$  and  ${}^8\text{He}$ , respectively. Either of them can undergo  $\beta$  decay with subsequent emission of neutron. The combination of the  $\beta$  decay and the neutron capture gives the same signature as the IBD event. The long half-life makes it difficult to effectively veto these events while maintaining low dead time.

There are other contributors to the correlated backgrounds. The Am-C neutron source is observed to create a pair of gammas correlated in time and with energies sufficient to pass the strict criterion on the delayed signal. In short, the mechanism is as follows. Neutrons from the source collide inelastically with the iron nuclei of the surrounding stainless steel vessel, which then emits prompt gamma rays. The neutron is then captured either on iron of the vessel or on gadolinium in the overflow tanks that are close to the ACUs. When these prompt and delayed gammas penetrates into the scintillator they can be misidentified as IBD events. As mentioned earlier, this background is negligible in the near halls, but contributes to the signal significantly in the far hall, and two out of three sources in each AD were removed in EH3.

The last background considered is coming from interactions of  $\alpha$  particles from natural radioactivity. They can interact with nuclei in the scintillator with release of neutron. The dominant interaction is  ${}^{13}\text{C}(\alpha, n){}^{16}\text{O}$ . Energy released from either neutron slow-down or from de-excitation of the produced  ${}^{16}\text{O}^*$  constitute the prompt signal and the delayed capture of the neutron complement the correlated pair of signals.

The backgrounds, which are considered after the application of veto, are summarized in Table 3.7 where I also list their approximate relative contribution to the signal in the three halls. The fractional contribution may vary from AD to AD and the stated number for each hall is an average for each hall. The uncertainties are typical uncertainties that do not change much from AD to AD. The latest estimates of the actual rates used in the oscillation analysis can be found in [21].

	EH1	EH2	EH3
Accidental	$1.35 \pm 0.01$	$1.15 \pm 0.01$	$2.06 \pm 0.03$
fast neutrons	$0.12 \pm 0.02$	$0.09 \pm 0.03$	$0.07 \pm 0.01$
${}^9\text{Li}/{}^8\text{He}$ isotopes	$0.42 \pm 0.23$	$0.29 \pm 0.15$	$0.36 \pm 0.19$
Am-C calibration source	$0.04 \pm 0.02$	$0.05 \pm 0.02$	$0.29 \pm 0.14$
8AD period*	$0.03 \pm 0.02$	$0.03 \pm 0.02$	$0.07 \pm 0.04$
${}^{13}\text{C}(\alpha, n){}^{16}\text{O}$	$0.01^{**}$	$0.01 \pm 0.01$	$0.07 \pm 0.04$

Table 3.7: List of backgrounds in  $\bar{\nu}_e$  detection. The contributions are in percent of the measured rate of antineutrino interactions. Background rates are taken from [21]. (\*) Two out of three Am-C sources were removed from each AD in EH3 during the installation of additional detectors in the summer of 2012. (\*\*) Uncertainty in the fraction is insignificant relative to the other uncertainties.



# 4. RPC Testing

Resistive plate chamber(RPC)-based detectors are part of the Daya Bay experiment's muon system. For its construction, around 1600 bare chambers were produced. They are assembled into modules which cover the water pools in each experimental hall.

This chapter reports results of training and testing of individual RPCs and of the performance tests of the assembled modules. The first section describes the design of the RPC detector system. Procedures and results of training and testing of the bare chambers are described in the second section. Third section covers the evaluation of performance of the RPC modules.

A small scale test setup for RPC measurements was built at the Institute of Particle and Nuclear Physics, Charles University in Prague. Its design and the first test measurements are described in the last section of this chapter.

## 4.1 The RPC System

The system of RPCs of the Daya Bay experiment works as a part of the detection system of cosmic muons. It reconstructs the position of the crossing of the RPC plane. It is designed as an array of planar modules each of which consists of 4 layers of bare RPC.

The arrays of RPC modules are placed on top of a retractable steel structure above the water pool in each experimental hall (EH). Altogether 56 modules are installed in each of the near halls (EH1 and EH2) and 83 modules are installed in the far hall (EH3), totaling 195 modules. Two additional modules are placed above the main array at two sides. Tracks of the muons that pass through the extra modules and the main array can be reconstructed. Details of layout of the RPC modules in each hall is described in Chapter 3.

Design and production of the bare chambers and modules are described in the first two of the following sub-sections, followed by two sub-sections on signal readout electronics system and the gas composition of the filling of the RPCs.

### 4.1.1 Bare chambers

RPCs are gaseous particle detectors which were introduced in 1981 by Santonico and Cardarelli[48]. They consist of two resistive planar electrodes separated by a gas gap. Bare RPCs of the Daya Bay experiment are made of two Bakelite sheets that are fixed parallel to each other creating a 2 mm gap. Outer surfaces are covered with graphite paint which is connected to high voltage (HV) and creates uniform electric field throughout the gas gap.

The most critical properties of the RPC electrode plates are their resistivity and surface smoothness. Both of these properties affect significantly its performance qualities.

The RPC design used in the Daya Bay experiment is similar to the one used by BESIII[49] and differs from commonly used RPC detectors mainly in the materials used. The chambers are built out of two parallel Bakelite sheets. The sheets are not treated with linseed oil in order to ensure its surface smoothness, which is

widely applied to Bakelite RPCs in various experiments[50, 51, 52, 53, 54]. The oil treatment proved to be problematic, causing long-term stability issues and ageing of the detectors, [55]. Instead, the Bakelite sheets, which are made of sheets of paper laminated with a mixture of phenolic and melamin resins, use coarser paper sandwiched in between sheets of finer quality paper with modified composition of the resins. The paper laminates are heat-compressed in between mirror-quality polished stainless steel press plates. The usage of the finer laminate outer layers and of the highly polished steel press plates ensures the smoothness of the surface of the Bakelite sheets and the application of the linseed oil is not necessary. The Bakelite sheets were required to have resistivity in the range of  $0.5 - 2.5 \times 10^{12} \Omega\text{cm}$  at  $20^\circ\text{C}$ .

The Bakelite sheets are cut into two sizes of dimensions  $1 \times 2.10 \text{ m}^2$  and  $1.10 \times 2.10 \text{ m}^2$ , and a graphite paint is applied to one side of each sheet. The surface resistivity of the graphite coating was measured and it was required to be in the range of  $400 - 1000 \text{ k}\Omega/\square$ .

The cut sheets are assembled in pairs of the same dimensions with their graphite-coated sides facing outwards and with a 2-mm gap in between. The two plates are separated at the edges by a frame made of acrylonitrile butadiene styrene polymer. The segments of the frame are 2 mm high and 10 mm wide. To ensure uniform spacing small button spacers were glued to the sheets in a  $10 \times 10 \text{ cm}^2$  grid. This way, the Bakelite sheets are prevented from bending inwards, or outwards. The spacers are of cylindrical shape with disk-shaped mid-section. The mid-section has larger diameter of 12 mm which provides larger surface area and decreases the surface leakage current. The cylindrical part of the spacer has a diameter of about 10 mm.

A special hubs are placed near the corners on each of the shorter side of the RPC. They provide a feedthrough for a gas flow into the gap between the plates and they are also used as connectors of high voltage to the graphite coatings. The chambers have a  $100 \mu\text{m}$  polyethylene terephthalate (PET) film on each side which covers the graphite painting and insulates the high voltage of the electrode.

Signal from each RPC is readout by pair of copper sheets that sandwich the chamber. Schematic drawing of a cross-section of the RPC is in Figure 4.1. Individual layers are indicated, including the Bakelite sheets and readout planes.

A photograph of one built RPC is in Figure 4.2. The inset photo shows a detail of the connector hub. The copper tape on the picture runs from the HV connector connector to the graphite coating.

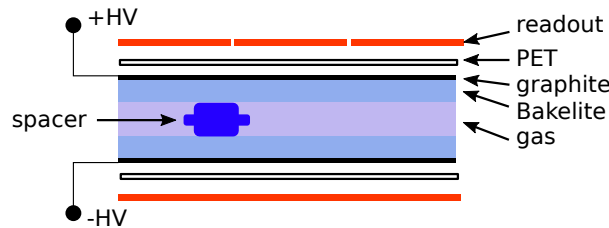


Figure 4.1: Schematic drawing of cross-section of bare RPC. Individual layers and a plastic spacer are indicated.

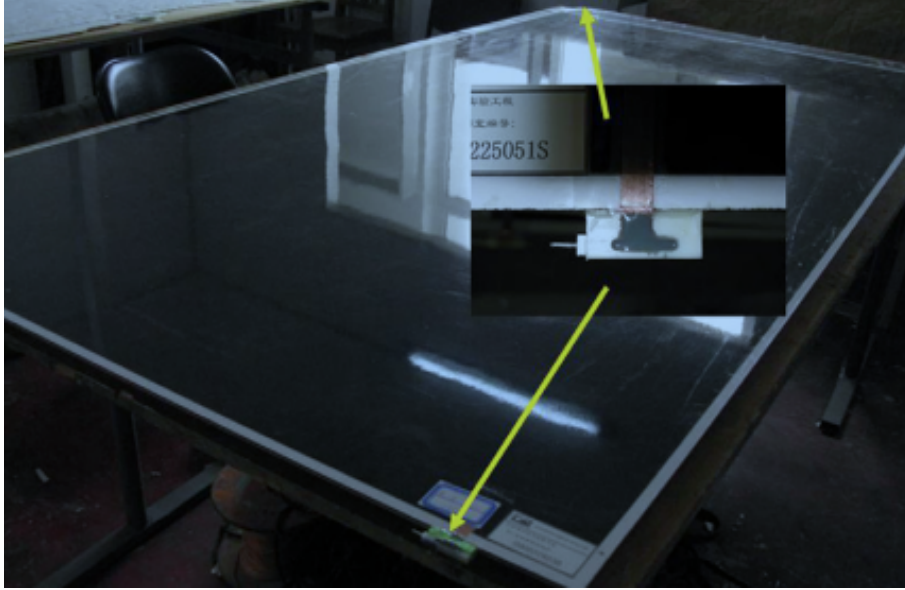


Figure 4.2: Photograph of an assembled RPC with a detail of the hub which serves as gas inlet/outlet and provides high-voltage connector pin.

#### 4.1.2 RPC modules

The bare chambers are assembled into modules of dimensions of  $2.17 \times 2.20 \text{ m}^2$ . A module is designed as an aluminum box with the RPCs stacked in 4 layers, each layer containing two chambers. RPCs of two sizes are used in each layer. As described in previous subsection, the smaller one has dimension of 1 m by 2.1 m and the larger one is 1.10 m by 2.12 m. Their order is switched in neighboring layers so that the dead area in the middle of each layer does not overlap vertically. The staggered layout of the RPCs in the layers is visible in the top-view and cross-sectional drawing in Figure 4.3. There are 8 RPCs used in a module in total from which half are small- and half are large- size RPCs.

Signals from the detectors are readout by external copper sheets placed on both sides of each layer, copper-clad FR-4 (flame resistant glass epoxy sheet) is used. Sheets at one side have machine-cut strips in a zig-zag design, with two turns at one side and one turn at the other side. This way the length of a strip is effectively 4 times longer and 4 times narrower. Total dimensions of the zig-zag strip are  $26 \text{ cm} \times 2.10 \text{ m}$  and the equivalent strip dimensions are  $6.5 \text{ cm} \times 8.4 \text{ m}$ . This zig-zag design provides shorter induced pulses of higher amplitude than a single 26-cm wide strip. Copper sheets on the other side of a layer serve as a grounding electrode and are left without divisions. The ends of the readout strips—outer most divisions at the side of one turn of the zig-zag strip—are connected to the ground plane via  $27\text{-}\Omega$  resistors to prevent signal reflections. The induced signal is read out via twisted-pair cables soldered to one end of the strip and to the ground electrode. The layout of the strip is shown in Figure 4.4. There are altogether 8 readout strips per layer yielding 32 readout channels per module.

Layers are stacked in two pairs, and the top and bottom neighboring layers share a common ground copper sheet. The readout strips of the neighboring layers are aligned perpendicular to each other. The top and bottom pairs of layers are

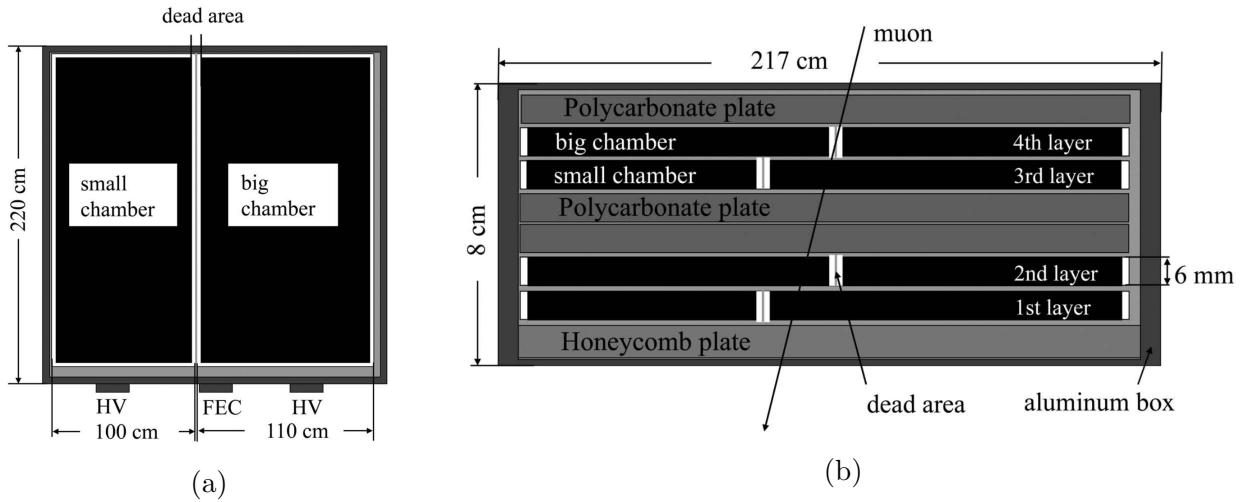


Figure 4.3: A schematic drawing of a module structure with highlighted dead areas. The location of high-voltage boxes and a FEC card is shown in the top view (a). Staggering of the bigger- and smaller-size RPCs in the module is depicted in the cross-sectional view (b).

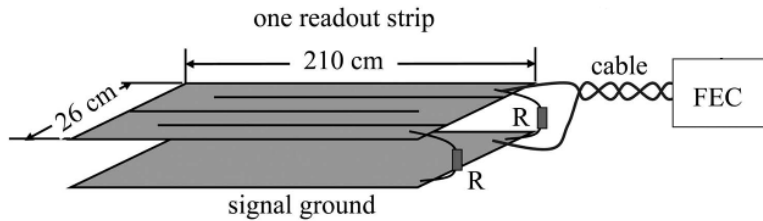


Figure 4.4: A schematic drawing of a readout strip. Zig-zag design is demonstrated together with end terminations with  $27\text{-}\Omega$  resistors. A twisted pair readout cable connects one end of the strip to the front-end-electronics card (FEC).

separated by an insulating layer. The layer consists of copper sheet sandwiched in between two 1-cm thick polycarbonate plates. The additional copper layer electrically separates the middle two layers and their readout strips. The same polycarbonate plate insulates the top layer from the aluminum box. The bottom layer is insulated by a 2-cm thick FR-4 fiber glass honeycomb plate which is more rigid and prevents the module deformation. A diagram of layering inside the module is shown in Figure 4.5. The figure also shows the changing alignment of the readout strips.

Steady flow of operational gas mixture is needed for a continuous operation of the RPCs. This is ensured by two inlets and two outlets on the outside of a module. The gas is then distributed to each bare RPC as indicated in Figure 4.6. Each gas-flow branch supplies 4 bare RPCs in series. This way, if a gas channel fails to work properly, two layers with X- and Y-direction readouts remain operational.

Each layer of the module is supplied by two individual high-voltage channels, positive high voltage is applied to the side of RPC which faces readout strips, negative high voltage is applied to the side facing the grounding plane. Two HV

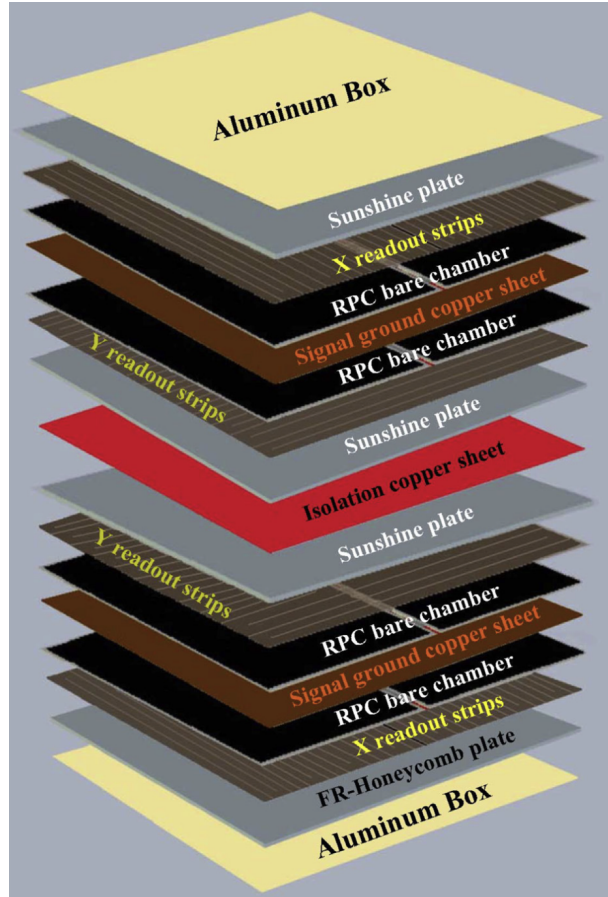


Figure 4.5: A schematic drawing of layers inside an RPC module. Readout strips of neighboring layers are aligned perpendicular to each other. The isolation copper sheet in the middle (red) electrically isolates the two readout strips facing each other.

boxes are mounted on each RPC module, they provide total of 8 HV connectors.

The 32 readout strips of the module are connected via twisted-wire cables to a front-end-electronics card (FEC) placed in an aluminum casing mounted from outside of the module.

### 4.1.3 Front-end-Electronics Card

The RPC detectors are relatively simple and they do not require multiplication of the signal when operated in streamer mode. However, they have large dark noise rate, that is, rate of signals that do not result from interaction of cosmic ray in the detector. Coincidence of more layers is required in order to suppress the high rates of unwanted signals. Designated front-end electronics processes signals of each module.

Custom FECs were designed. The input signals are discriminated and digitized. The digital version of signals is processed on a dedicated FPGA chip which is capable of distinguishing coincidences in between module layers at different levels—2, 3, or 4 layers with signal over threshold in at least one readout strip. Processed data are then buffered and ready to be serially transmitted to the next step in the DAQ chain.

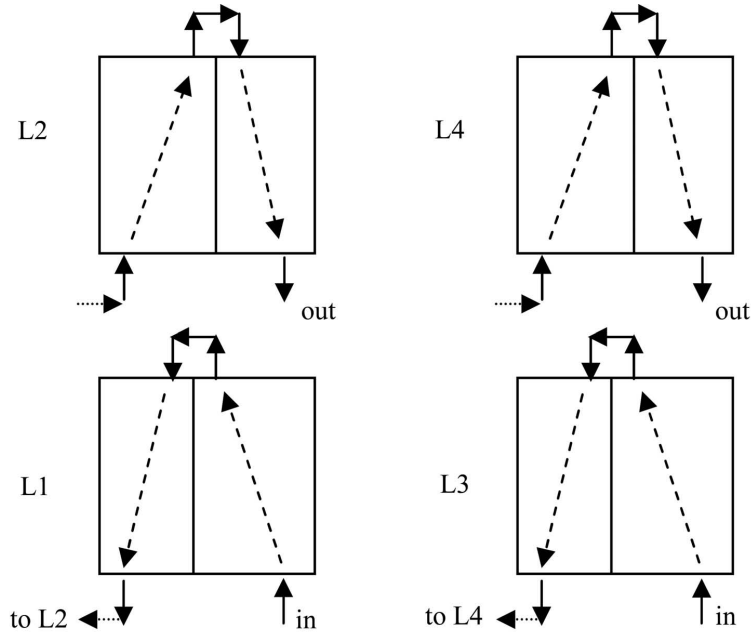


Figure 4.6: A schematic drawing of flow of the filling gas mixture through the individual bare RPC in the module. Layers L1 and L2, and layers L3 and L4 are supplied by separate gas inputs, respectively.

Data from each module's FEC are sent through transmission stations, readout transceivers (ROT), to RPC trigger module (RTM) and readout module (ROM). RTM decides which modules are readout and sends a readout trigger signal to each of them. ROM collects data from the triggered modules and pass them to the experimental data acquisition system (DAQ). A schematic view of the data flow is depicted in Figure 4.7.

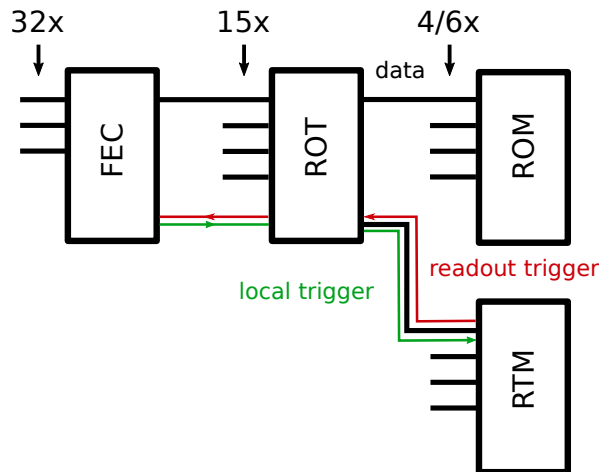


Figure 4.7: Diagram of the RPC DAQ system. The system consists of the front-end electronics card, FEC, the readout transceiver, ROT, and the readout and trigger modules, ROM and RTM, respectively. Signals from RPC readout strips of each module are fed via 32 twisted-pair cables to the FEC. 15 FECs are connected to one ROT with multi-wire serial cables. 4 (6) ROTs connect to the ROM and RTM with optical fibers in near (far) halls.

#### 4.1.4 Filling gas composition and flow rate

RPCs at Daya Bay operates in streamer mode. This mode requires proper gas composition. The most common mixture used is Argon–R134a–iso-butane. Each of the components has specific role. Argon as an inert gas with low mean energy for ion-electron pair production, R134a (1,1,1,2-tetrafluoroethane) is an electronegative gas which serves as a quencher for produced electrons, and iso-butane effectively absorbs x-rays emitted during the deexcitation of the gas during the streamer discharge.

When sufficiently high voltage is applied to the electrodes of RPC, electrons from the primary ionization of the detected radiation start avalanche which then multiplies by x-ray emission, and the streamer is initiated. The streamer has significantly higher charge than a single avalanche and is observed to appear with a delay after the initial avalanche [56]. The x-ray quenching by iso-butane prevents the streamer from spreading spatially over wider areas, preventing the RPC from complete discharge and controlling the amount of charge transfer and dead time of the detector.

Apart from requirements on performance of RPCs there are also safety concerns which lead to decision on the final mixture. Due to its flammability, iso-butane fraction is limited to 4% which is considered safe in underground environments.

Large discharges in RPCs tend to decompose R134a and produce HF acid which erodes surface of the resistive plates [57] and accelerates aging of the detectors. An addition of a small amount of SF<sub>6</sub> into the mixture allowed to reduce the amounts R134a.

A study of various mixture compositions showed that Daya Bay RPCs can operate well with iso-butane fraction in range 2–4% and R134a fraction around 20% after addition of 0.2% of SF<sub>6</sub> [58]. The nominal gas composition for Daya Bay RPCs is Ar–R134a–iso-butane–SF<sub>6</sub> in the ratio 65.5:30:4:0.5.

## 4.2 Training and testing of bare RPC chambers at IHEP

New RPCs need a special treatment called training before use in order to achieve good and stable performance. During training, high currents cause burning of impurities of the inner surfaces of the resistive electrodes. These impurities cause non-even electric fields in the gas gap and produce spots with often spontaneous discharges.

Before assembly into the modules, each RPC was tested with cosmic muons. Only RPCs that satisfied specific requirements on their performance were then used in the modules.

The production of RPCs started in 2008, and training and testing of 1600 RPCs in total was performed at the Institute of High Energy Physics of Chinese Academy of Sciences in Beijing, China, and finished in 2009.

### 4.2.1 Training of RPC

RPCs were trained in batches where 8 RPCs at a time were put on shelves of a training stand. They were connected to one supply of filling gas in series, so that the top most RPC received fresh gas and the bottom one was connected to the gas exhaust. The purpose of training was to expose RPC to high currents for relatively long time. They were flushed with pure argon, which ensured there was no quenching elements. Total gas flow rate was set to  $100 \text{ cm}^3/\text{min}$  which is approximately 1 full volume of all 8 RPCs in about 5.5–6 hours. The high voltage was set to about 10 kV. This way continuous self induced streamer discharge occurred and currents up to 1 mA were passing through the RPCs. The currents were limited by the capability of the used HV modules. HV of each RPC was adjusted so that the cap of 1 mA was not crossed.

Each batch of 8 RPCs was trained for about 48 hours. Throughout the training period, currents in individual RPCs and environmental data (room temperature and humidity, and atmospheric pressure) were recorded. During the first 20 to 30 hours all RPCs exhibit increase in current. Then the current starts decreasing again and appears to stabilize after about 50 hours of training. Typical current variation of 7 RPCs is shown in Figure 4.8.

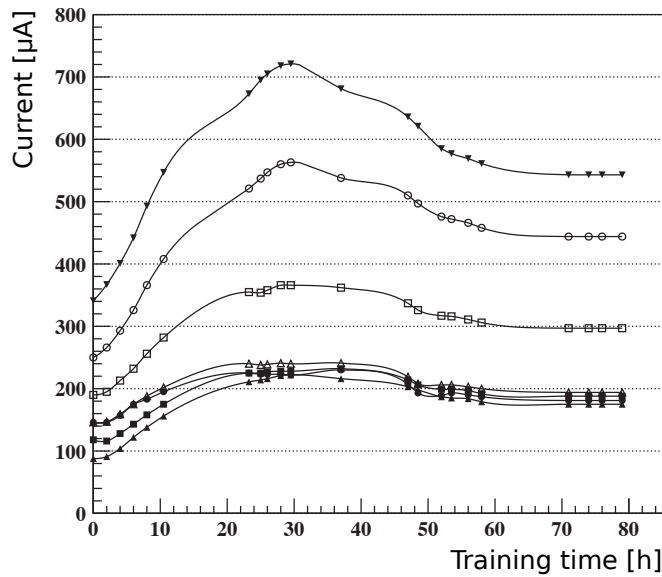


Figure 4.8: Monitored currents of 7 RPCs during the training period. All RPCs exhibit increase of current in the first 20 hours and stabilization of the current after 50 hours of training.

### 4.2.2 Tests of RPC performance

After training, RPCs were moved to an air-conditioned room for testing by cosmic ray muons. The aim of the testing was to quantify performance of each RPC in terms of its muon detection efficiency, dark current, and the rate of signals not correlated with any passing muon, the so called singles count rate (SCR).

Although the room's conditioning system had limited capabilities, the variation of ambient temperature was suppressed to a standard deviation of  $1^\circ\text{C}$

around its mean value of 20°C. Due to large differences in humidity between the winter and summer season in Beijing, relative humidity in the room varied with deviation of 9% around its mean value of 33%. Pressure varied through the year by about 1 kPa around a mean value of 101.5 kPa. Time dependent variations of all three quantities are plotted in Figure 4.9. One can immediately notice that while temperature was relatively stable, humidity and atmospheric pressure had large seasonal fluctuations.

The performance tests of bare chambers were done before final decision on the filling gas composition. A simpler mixture was used for the evaluation which consisted of argon, R134a, and isobutane in relative amounts of 53:43:4. The difference in performance with this mixture as opposed to the Daya Bay nominal has no major impact on the decision about chamber's quality.

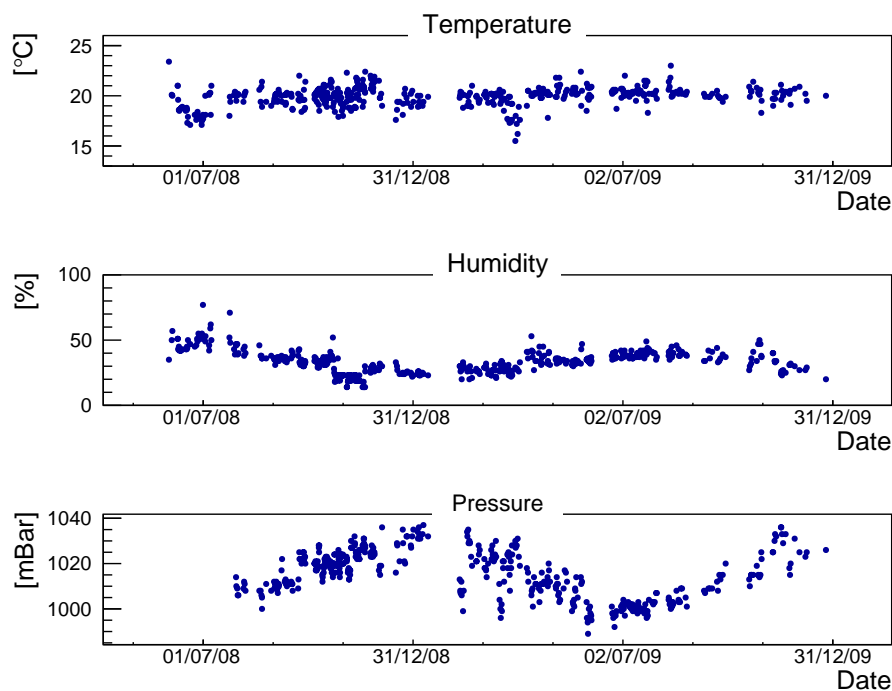


Figure 4.9: Time variations of room temperature, relative humidity, and atmospheric pressure in testing room during tests of RPC with cosmic muons. Seasonal variations of humidity and pressure are observed.

Up to six RPCs were stacked at a time into stand shelves for measurements. There were 3 blocks of plastic scintillator. They served as cosmic muon telescopes. One of the scintillators was stacked on top of the shelves, above all RPCs, and the other two scintillators were placed at the bottom shelf, underneath the RPCs. Layout of the measurement stand shelves is depicted in Figure 4.10. Each scintillator block was a 1 m by 1 m panel about 10 cm thick. Scintillation light from each panel was detected by a photomultiplier tube (PMT). Amplified and discriminated signals from the photomultipliers were connected to a coincidence module which produced an output signal when all 3 scintillators were traversed by a muon. Every muon detected by this coincidence passed through the tested RPCs.

Each RPC under test was sandwiched by two FR-4 copper-clad sheets where

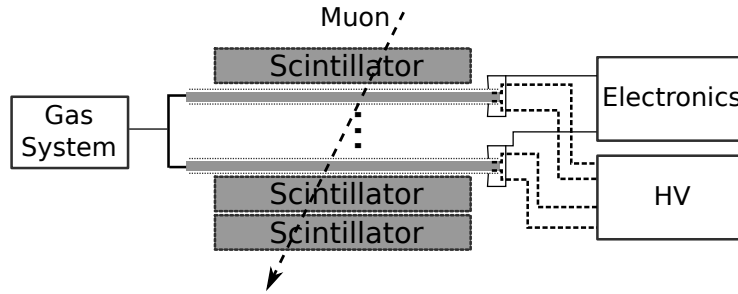


Figure 4.10: Schematic drawing of layout of RPC tests with cosmic muons.

the top one was connected to ground and the bottom one had 4 zig-zag strips cut out, as described in Section 4.1.2 on RPC modules. One end of each strip was terminated with a  $24\text{-}\Omega$  resistor connected to the ground sheet. Signals were readout from the other end of the strip. Signals from each of the 4 strips were fed to a discriminator and were discriminated at 50-mV threshold. The discriminated signals were then summed and the resulting sum was a representation of any hit in the RPC. One output of the summed signal was sent to a counter module which recorded the so called single events, i.e. signals without a requirement to be caused by the muon selected by the telescope scintillators. Another output of the summed signal was fed into a coincidence module together with the signal from the 3 scintillators. Efficiency was then determined from the ratio of the number of these four-coincidences over the number of all muons detected by the telescopes.

The 6 RPCs were prepared for the measurements in the evening of the preceding day, and were flushed with the operational gas mixture over night. This way the chambers were allowed to reach thermal equilibrium with the environment and the argon filling from training was flushed out by the testing-gas mixture. With the flow of  $200\text{ cm}^3/\text{min}$  the total volume of gas in all 6 RPCs was exchanged about 6 times over night.

High voltage of opposite sign was brought to each electrode of each chamber from separate channels. Actual voltage and current was measured and stored for each measurement. Total voltage drop between electrodes of each RPC was changed between 6 and 9 kV in steps of 100 V. Measurements over the full range of applied voltage were repeated in cycles with 100 s at each voltage.

The series of measurement at each HV was repeated at least 5 times. With the average rate of the scintillators' 3-fold coincidence of about 20 Hz, the accumulated number of muons for each applied HV was approximately  $5 \times 100\text{ s} \times 20\text{ Hz} = 10000$ , and therefore the statistical precision of the efficiency measurement was at the level of 1% or better.

The typical efficiency curve of an example RPC is shown in Figure 4.11a. At around 7 kV, the efficiency increases quickly to its high value around 95% where it plateaus and does not change much with further voltage increase. The transition region is related to the streamer production from the primary ionization. The higher the voltage is the higher probability of creation of the streamer is and also the larger charge is transferred during the streamer. Higher charge transfers induce larger signals in the readout strips and therefore increase the probability of its discrimination-threshold crossing.

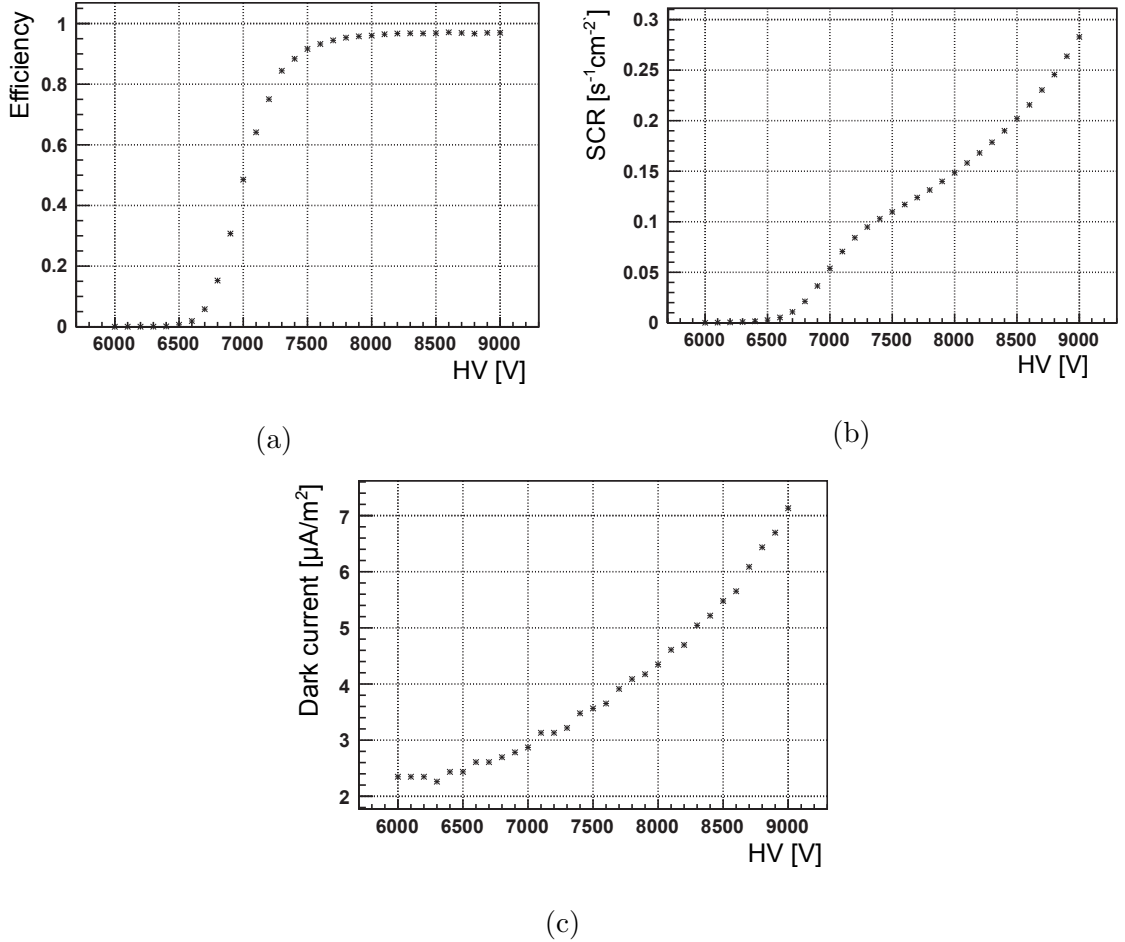


Figure 4.11: Example of measured characteristics of RPC with respect to applied HV. Efficiency (a) follows typical shape with fast increase at around 7 kV with plateau for voltages above about 7.5 kV. Singles count rate (b) and dark current(c) also shown.

Figure 4.11c shows the typical dependence of singles count rate with respect to the applied high voltage. Similarly to the efficiency curve, fast increase is observable in the same region, caused by increasing probability of a primary ionization (not necessarily from a cosmic muon in this case) to produce signal which would cross the threshold. Unlike the efficiency curve, the SCR curve does not plateau with increasing voltage due to increasing probability of spontaneous emission of an electron from the inner surface in presence of high electric field.

The current through the chamber which is partially caused by the surface currents, but the dominant part is from the charge transfer during the streamer production. Its dependence on the applied high voltage is plotted in Figure 4.11c. Since the streamer production is largely due to spontaneous electron emissions, independent of cosmic muon rates, I refer to it as dark current. It exhibits continuous growth without any apparent changes to the shape.

Rejection criteria for each RPC were set for applied HV of 8 kV and with discriminator threshold set at 50 mV. Figure 4.12 shows the distribution of the measured efficiencies of all tested RPCs. The average efficiency is 95.34%. RPC was required to reach at least 94% efficiency. This requirement was motivated by

the requirement that the total efficiency of the muon veto system was greater than 99.5%. Based on simulations, 94% efficiency of an RPC translates to approximately 96.5% efficiency of a module triggered by at least 3 layers. The average efficiency of the accepted chambers is 96.05%.

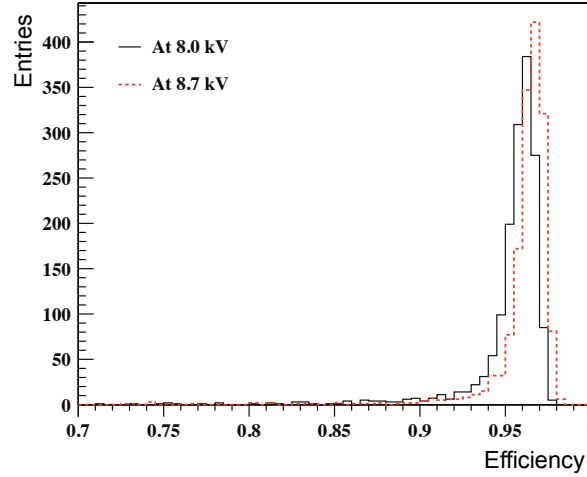


Figure 4.12: Distribution of efficiencies of tested RPCs. Distribution is higher and narrower for efficiencies measured at 8.7 kV (red dashed line) than for efficiencies at 8 kV (black line)

Figure 4.12 also shows distribution of efficiencies at 8.7 kV. The average efficiency is higher and the spread is lower than for the distribution at 8 kV. This suggests that some RPCs reached their highest efficiency at voltages higher than 8 kV. This “late” reach of the plateau is attributed to large gas gap which effectively lowers the electric field across the gap.

To reflect the shift of the efficiency curve, the HV of 50% efficiency is a good measure of the position of start of the plateau. Figure 4.13 shows the distribution voltages needed to reach 50% efficiency for RPCs accepted and rejected by the efficiency criterion. Since the voltage drop over the gas gap depends on resistivity of the Bakelite sheet and also on the density of the gas filling, effective voltage varies between RPCs and also with the ambient temperature and air pressure. Voltages in Figure 4.13 are corrected for the climate variations and voltage drops across the Bakelite sheets.

The average value of the 50% efficiency of the accepted chambers is 6861 V and the distribution has a spread of about 132 V. If the changes in the position of the plateau are caused by the variations in the sizes of the gas gaps, the variation of about 2% corresponds to variation of 40  $\mu\text{m}$  in the gap size.

There was no intrinsic requirement for the dark current and singles count rate. Their limits were established in order to reject outlying RPCs which would be strong candidates for future failures. Figure 4.14 shows histograms of measured SCR and dark current at 8 kV. The statistics are divided to sets of RPCs accepted by the efficiency criterion and of those rejected by it. Sample of detectors rejected based on the efficiency appears to have longer tails in both histograms, although this cannot be confirmed due to limited statistics. RPCs were required to have SCR lower than 0.8 Hz/cm<sup>2</sup> and dark current lower than 10  $\mu\text{A}/\text{m}^2$ .

In total, 171 RPCs out of 1600 tested ( $\sim 11\%$ ) had efficiency lower than 94%

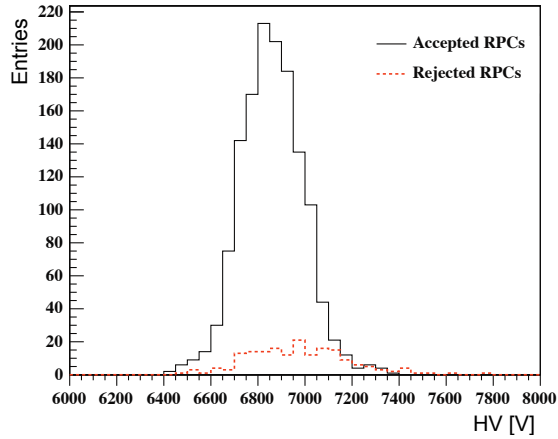


Figure 4.13: Distribution of applied HV for which the tested RPCs reached efficiency 50%. Rejected RPCs (red dashed line) became 50% efficient at higher HV than accepted RPCs (black line)

at 8 kV and with 50 mV threshold. Further 13 chambers failed the SCR criterion and one did not pass the dark-current criterion.

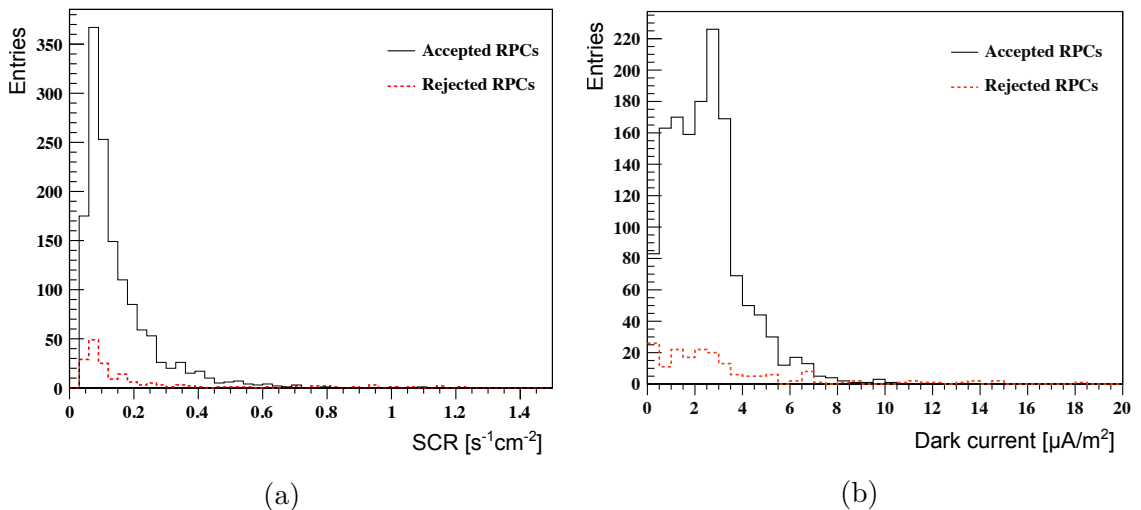


Figure 4.14: Distributions of singles count rates and dark currents of the tested RPCs at applied voltage of 8 kV. RPCs rejected by the requirement of at least 94% efficiency are plotted in red dashed line.

### 4.3 RPC Module Performance

After each RPC bare chamber had been tested it was used for the module assembly. The design of the RPC module was described in Section 4.1.2. Each assembled module was first tested for possible gas leaks and then transported to a testing room.

Eight modules were stacked in shelves, vertically aligned, as can be seen on the photo in Figure 4.15. Modules were connected to separate branches of gas inlets and outlets. Composition of used gas was the same as the experiment's

nominal, i.e. Ar, R134a, iso-butane, and SF<sub>4</sub> in the proportions 65.5:30:4:0.5. Total flow of about 600 cm<sup>3</sup>/min was supplied to the system. All the modules were connected to a common high voltage supply with 7.6 kV applied.

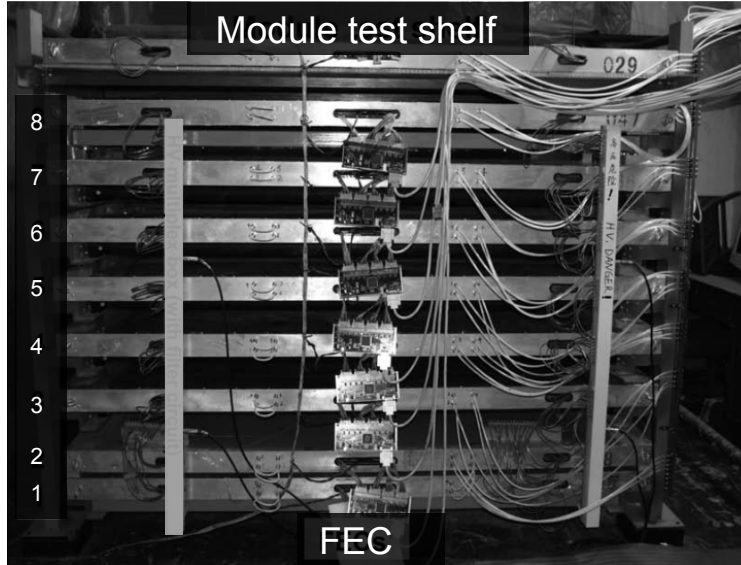


Figure 4.15: Photograph of RPC modules in the test shelves. The module on top, labeled 029, was not used in the tests.

FEC boards were connected to the signal lines of each module and were read-out by a custom built bench-top readout module. Readout of each module was triggered when at least two layers of the modules registered signals, I will denote this situation as 2/4 trigger. In the offline analysis of the data, readout triggers with signals in at least 3 layers were marked as 3/4 triggers.

The performance of each module was tested by cosmic muons. Muons were identified by the modules themselves. For each detector under test (DUT), three neighboring modules were used as muon telescopes, one above, and two below DUT. Only 5 of 8 shelved modules could be tested at a time. The top most module and the two modules at the bottom of the shelves were kept in place during the testing of all modules. Therefore, if the modules are numbered 1 to 8 from bottom to top, as indicated in Figure 4.15, then module 3, for example, was tested with muons identified by modules 1, 2, and 4.

The design of the modules with perpendicular readout strips across the layers allows determination of location of the muon crossing. Therefore, modules could be tested for efficiency in different segments which we call patches. One patch is determined by a signal in at least two layers with opposite directionality of their readout strips. There is 8 strips per layer, therefore a module is divided into 64 patches.

The muon passage was identified when the three muon telescope modules neighboring DUT had coincident signal in the same patch. Therefore, efficiency was measured for mostly vertical muons with zenith angle not larger than about 30°. Coincident readout triggers of type 2/4 and 3/4 of DUT were recorded and two types of efficiencies of a particular patch of DUT were defined depending on the trigger type, 2/4 or 3/4 efficiency.

Figure 4.16 shows the patch efficiencies for an example module. Each patch is

numbered according to its position beginning with 0 at the corner of first X- and Y- strip and ending with 63 at the diagonal corner. There is a significant drop of about 5% in 3/4 efficiency for a group of patches right in the middle. These patches overlap with the middle dead area between the two bare RPCs composing each layer. The 2/4 efficiency is not as sensitive to the dead area because of the alternate assembly of large and small bare RPCs. The dead spaces in two layers of the same readout strip directionality do not overlap vertically. Therefore, if the vertical muon passes through the dead area of one X layer, it avoids passing it in the other X layer.

Smaller dips are also visible in Figure 4.16 for both patch efficiencies. These correspond to the reduction of efficiency in patches along the edges of the module.

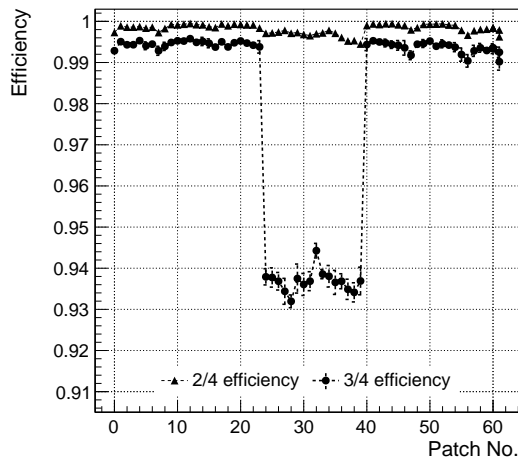


Figure 4.16: Efficiencies of individual patches of an example e module. Efficiencies of the module in 2/4 (triangles) and 3/4 (circles) trigger mode are plotted. The 3/4 mode is more sensitive to the dead area in the middle of the module at the border line of the two bare chambers of each layer. Patches are numbered from 0 to 63 as  $X \times 8 + Y$ .

Module efficiencies were also estimated based on the measured efficiencies of bare RPCs. Designated MC simulations of passage of muons through modules were performed. Module efficiencies were calculated for different scenarios where the module was assembled with bare chambers of given efficiency.

The results are summarized in Table 4.1 and Table 4.2. For different bare chamber efficiencies the corresponding module efficiency is included for the two different trigger types. The former table lists efficiencies of the patches along the middle dead area. The large difference between the 2/4 and 3/4 efficiencies agree with the measurements in Figure 4.16. Table 4.2 lists estimated overall module efficiencies. There is stronger dependence of the 3/4 efficiency on the efficiency of individual bare chamber.

The aforementioned MC simulation assumed ideal bare chambers without the polycarbonate spacers which supported the gas gap in a uniform grid every 10 cm. They cover about 5% of the full area of an RPC. From different simplified simulations it was estimated that they contributed about 0.1% and 0.3% inefficiencies

chamber eff.(%)	patch 2/4 eff.	patch 3/4 eff.
92	98.93	90.21
94	99.28	91.97
96	99.57	93.44
98	99.80	94.58
100	100.00	95.38

Table 4.1: Efficiencies of patches over central dead areas of a module from MC simulations.

chamber eff.(%)	module 2/4 eff.	module 3/4 eff.
92	99.61	95.11
94	99.77	96.66
96	99.89	97.79
98	99.95	98.57
100	100.00	98.93

Table 4.2: Module overall efficiency from MC simulations.

in the 2/4 and 3/4 trigger modes, respectively.

Acceptance criteria were set for RPC module patch efficiencies. Based on simulations, the expected patch 3/4 efficiency which corresponds to the bare chamber efficiency of 94% was determined to be about 92% for the middle (less efficient) patches, and about 95% for the rest. These values were set as minimal requirement for the modules.

Figures 4.17a and 4.17c show distributions of the patch efficiencies of 199 tested modules. The 2/4 patch efficiency (top plot) has one narrow peak with a mean value of 99.8%. The 3/4 efficiency (bottom plot) has a broader peak at 99.3% and another one at around 94%. The latter peak corresponds to the less efficient patches over the dead area.

The overall module efficiencies are plotted in Figures 4.17b and 4.17d, and they follow the expectations from the measured patch efficiencies. The mean module 3/4 efficiency 97.9% agrees with the expectation based on average bare chamber efficiency of 96.05%.

## 4.4 RPC Testing Setup in Prague

We have built a smaller scale RPC testing setup at the Institute of Particle and Nuclear Physics, Faculty of Mathematics and Physics, Charles University in Prague. The purpose of this setup is to study mechanisms behind creation of the RPC signal and to determine its amplitude and spatial evolution. Moreover, it serves as a platform for training new students for work in laboratory and to have first touch at the experimental instrumentation.

The RPC testing setup consists of gas system, HV and signal readout electronics, and scintillator detectors for selection of cosmic muons. We have two small 50 cm  $\times$  25 cm RPCs of design similar with RPCs used in the Daya experi-

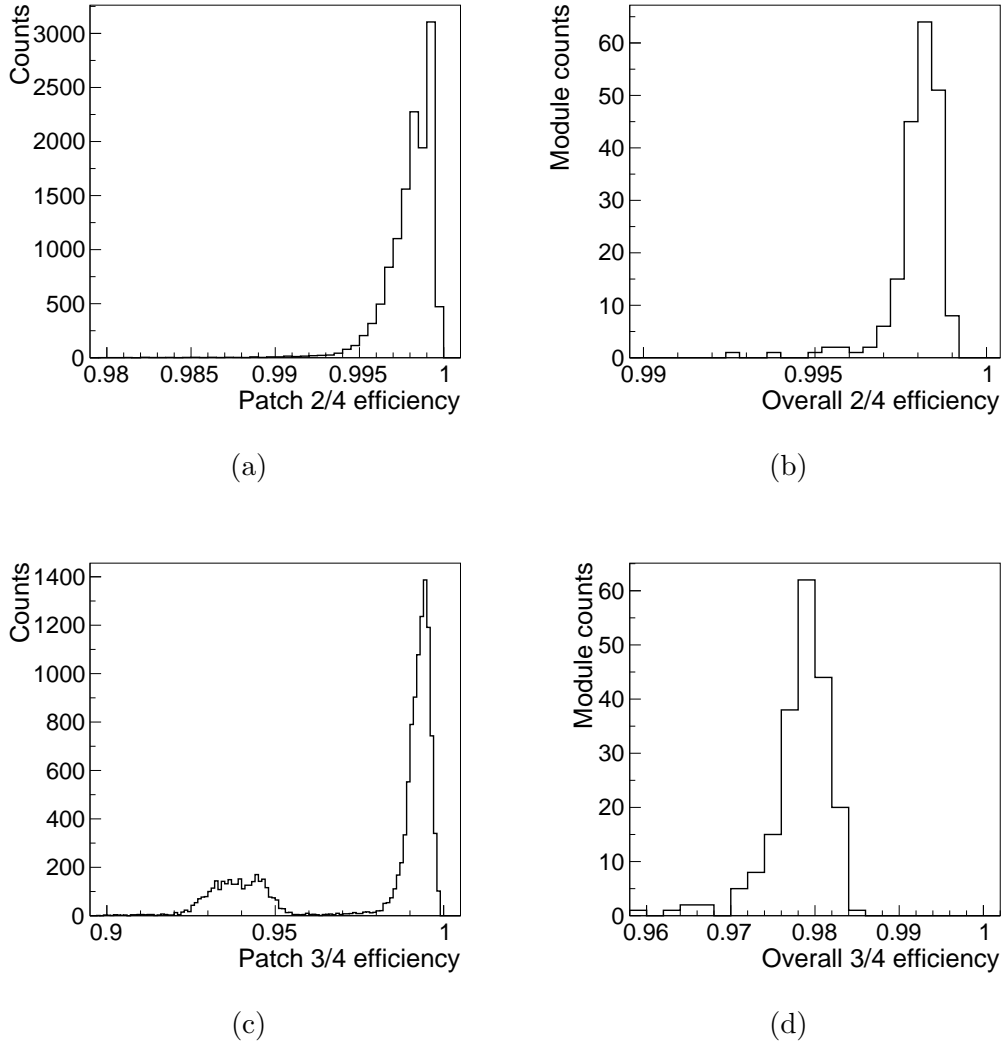


Figure 4.17: Distribution of RPC modules' patch (a), (c), and overall, (b), (d), efficiencies in 2/3 and 3/4 trigger modes. Decrease of efficiency in patches across the middle dead area of the module are visible in 3/4 mode of patch efficiencies (c).

ment. The RPCs and the scintillators are placed in a testing stand with shelves, in Figure 4.18.

The gas system is designed to prepare the desired gas mixture and supply it to the tested RPCs. Individual component gases, argon, R134a, and isobutane, are filled into two cylindrical gas containers (15 litres each) with preset proportions. The amount of each component is controlled by precise MKS[59] flow controllers calibrated for the particular gas. After filling, the mixture is supplied to the RPCs with flow controlled by another MKS flow controller. The flow of the argon gas into the containers can be set up to about  $1400 \text{ cm}^3/\text{min}$ . Flow of other components scales down according to their proportion. The typical flow of final mixture to the RPCs is around  $2 \text{ cm}^3/\text{min}$ .

Three scintillation blocks are used as cosmic muon telescopes. The scintillators have dimensions  $45 \text{ cm} \times 20 \text{ cm} \times 5 \text{ cm}$ , and each is equipped with one PMT. One



Figure 4.18: Photograph of RPC test setup built at our institute in Prague. The gas system is visible in the green steel rack. Shelves with tested RPCs and telescope scintillators is in the middle of the photo. Signal processing electronics and HV supply modules are placed in NIM and CAMAC crates in the blue rack on the right. Measurement is controlled from a PC.

scintillator is placed on the top of the testing shelf and two are at the bottom. This setup is the same as on previously shown in Figure 4.10. Signals from the PMTs are fed to a coincidence logic module and 3-fold coincidence selects muons that pass through the tested RPCs.

Top and bottom electrodes of RPCs are connected to precision high voltage supply modules that can provide up to 5 kV at each channel with positive or negative polarity. Therefore, RPCs can be operated at voltage difference up to 10 kV. RPCs are sandwiched in between two copper sheets of size  $50 \text{ cm} \times 25 \text{ cm}$ , where one of them have carved out two zig-zag strips. Signals from the readout strips are discriminated and connected to a coincidence module with the signal of the muon selected by the scintillator telescopes. Discriminated signals from each RPC and their coincidences with the selected muons are counted in a scaler module. The scaler module is automatically read out via a CAMAC-to-PC interface.

With student Tadeáš Dohnal, we commissioned the setup and measured basic properties of two small RPCs. Efficiency vs HV curves were tested for one RPC untrained (RPC1) and one RPC trained properly (RPC2). The purpose and method of training is described early in this chapter in section 4.2. The curves are plotted in Figure 4.19, and they are similar except that the efficiency of trained RPC2 starts rising at slightly lower HV than efficiency of RPC1.

In fact, although RPC1 had not been trained, it had been connected to HV and tested for efficiency before and the similarity of the efficiency vs HV curve is not too surprising. The work is described in more detail in diploma thesis by Dohnal[60].

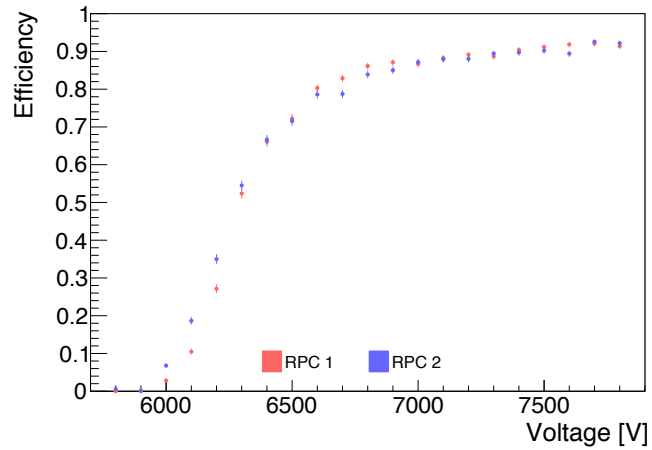


Figure 4.19: Measured efficiency vs applied HV for untrained (RPC1) and trained (RPC2) small RPCs.



# 5. Muon Decay

Muons decay dominantly via weak interaction into electron/positron and a pair of neutrino and antineutrino

$$\mu^- \rightarrow e^- + \bar{\nu}_e + \nu_\mu, \quad \mu^+ \rightarrow e^+ + \nu_e + \bar{\nu}_\mu$$

Part of muons decay with additional radiation of a photon:

$$\mu^- \rightarrow e^- + \bar{\nu}_e + \nu_\mu + \gamma,$$

and similarly for  $\mu^+$ . As will be discussed later in this chapter, the fraction of radiative decay to non-radiative depends on the minimal energy of the photon that can be registered.

Since the life time of the muon is relatively long, mean lifetime of muon in vacuum is 2.197  $\mu\text{s}$  [20], it predominantly decays at rest. Therefore, the energy deposition in a detector is given only by the decay process itself, independently of muon's initial energy.

Decays of  $\mu^-$  are influenced by the chemical environment because they can pair with nuclei of surrounding atoms the same way electrons do. Moreover, their binding is much stronger than binding of the electron, and they always quickly attach to the nucleus and create a muonic atom.

Goal of this chapter is to describe spectrum of energies from decays of cosmic muons in the Daya Bay detectors. I first introduce simple calculation of the spectrum of electrons or positrons in the Born approximation. I also address a question of effect of the radiative muon decay in combination with radiative corrections to the simple formula. In the last part of this chapter, I describe how I modeled spectrum of electrons from  $\mu^-$  decays in orbit. I conclude with combination of models for  $\mu^+$  and  $\mu^-$  decays.

## 5.1 Spectrum of $e^-/e^+$ in Born approximation

A generic formula for a decay of a fermion into three fermions was first developed by L. Michel in [61, 62]. A four fermion contact interaction is used as depicted by a simplified Feynman diagram in Fig. 5.1. Within the Fermi model and using the V-A structure of the Standard Model, the formula for differential decay width of unpolarized muon with respect to the electron energy can be written in the form[63]

$$\frac{d\Gamma^{\text{Born}}}{dx} = 2\Gamma_0 x^2 \beta f^{\text{Born}} \quad (5.1)$$

$$f^{\text{Born}}(x) = \left[ 3 - 2x + \frac{x}{4} (3x - 4) (1 - \beta^2) \right]. \quad (5.2)$$

Here I denote electron energy in accordance with frequent use in literature as a fractional energy  $x = 2E_e/m_\mu$  where  $m_\mu$  is the mass of the muon and  $m_\mu/2$  is approximately the maximal energy of the electron in the limit of massless electrons and neutrinos. The total muon decay width in Born approximation is

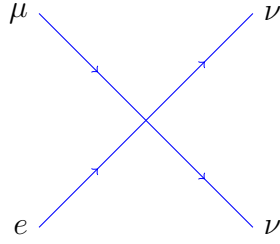


Figure 5.1: Simplified Feynman diagram for amplitude of muon decay process which uses only four-fermion contact interaction.

$\Gamma_0 = G_F^2 m_\mu^5 / 192\pi^3$ , and  $\beta = \sqrt{1 - m_e^2/E_e^2}$  is the electron's relativistic  $\beta$  factor.  $G_F$  is the Fermi coupling constant and  $m_e$  is the electron mass.

For illustration, the resulting differential decay width vs. the fractional energy of the electron is plotted in black line in Figure 5.4.

## 5.2 1st order radiative corrections

In the 50s of the last century, first calculations of radiative corrections to the muon decay were published [64, 65, 66]. The Feynman diagram of the Fermi model interaction is then augmented by virtual photon lines. New diagrams contribute to the amplitude of the process, see Figure 5.2.

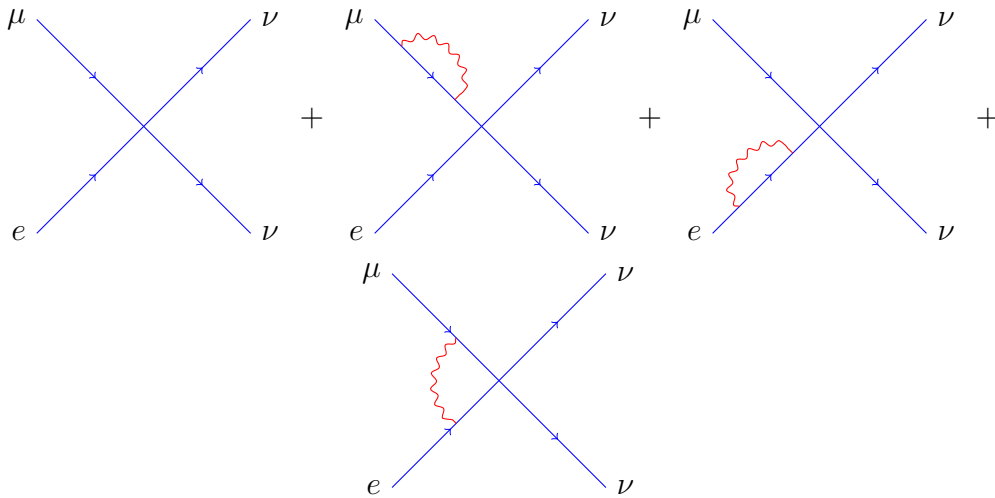


Figure 5.2: Simplified diagrams for calculation of the amplitude of muon decay process with radiative corrections.

The calculations of the amplitude in the 1st order of electromagnetic coupling constant  $\alpha$  are divergent. In order to suppress the divergence, concurrent process in the same order of  $G_F$  and  $\alpha$  must be added. The added process is muon decay with radiation of a gamma photon, which is referred to as radiative decay, and the radiation of the photon as apart of the decay process is often called inner bremsstrahlung. The corresponding new diagrams, shown in Figure 5.3, cancel out the divergence at the level of the decay width.

The formula for the total muon decay width which includes the non-radiative and radiative decay channels in the first order of  $\alpha$  and for unpolarized muon can

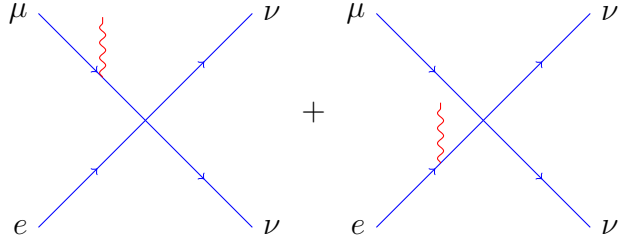


Figure 5.3: Simplified diagrams for calculation of the amplitude of radiative muon decay process.

be rewritten [63, 67] as

$$\frac{d\Gamma}{dx} = \frac{d\Gamma^{\text{Born}}}{dx} + \frac{d\Gamma^{(1)}}{dx} = 2\Gamma_0 x^2 \beta \left( f^{\text{Born}}(x) + \frac{\alpha}{2\pi} f^{(1)}(x) \right) \quad (5.3)$$

The explicit form of the correction  $f_1(x)$  can be found in the Appendix A.1.

The resulting corrected energy spectrum of electron is plotted in Figure 5.4 in red curve, overlaid over the spectrum calculated in the Born approximation (5.1). The two formulas, (5.1) and (5.3), share the same decay constant  $\Gamma_0$  and therefore do not give the same total decay width  $\Gamma$  in the figure.

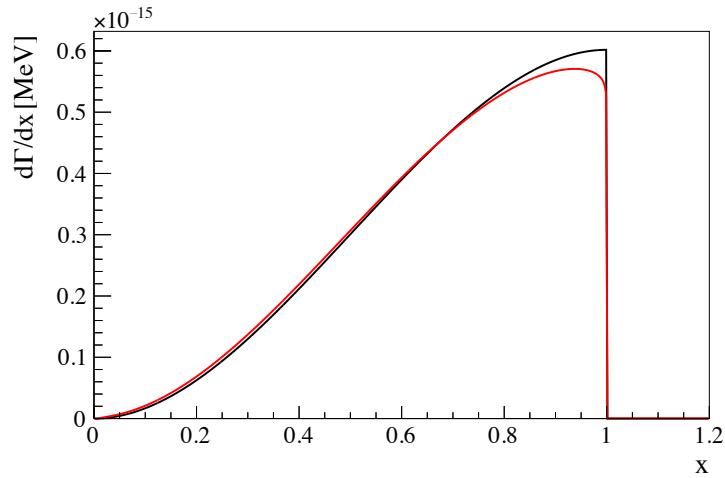


Figure 5.4: Calculated differential decay width with respect to the energy of electron from muon decay. Born approximation (black) is compared to result of formula (5.3) which includes radiative corrections (red). I used the same coupling constant  $G_F$  ( $G_F/(\hbar c)^3 = 1.1663787 \times 10^{-5} \text{GeV}^{-2}$ [20]) in both cases, therefore the total decay widths, or the integrals of the curves, do not match.

### 5.3 Inner bremsstrahlung and radiative muon decay

The energy distribution presented in the previous section does not, in general, represent energy from the muon decays observable in the Daya Bay antineutrino

detectors. When the decay process radiates a gamma photon, it must be included to the total energy deposited in the detector. I will call the total energy which can be deposited in the detector visible energy  $E_{\text{vis}}$ .

In order to calculate the differential decay width of the muon with respect to  $E_{\text{vis}}$ , contributions of the two decay modes need to be separated in (5.3) and the part describing the radiative process must be expressed with respect to the visible energy  $E_{\text{vis}}$ , i.e. the sum of energies of electron and photon.

The procedure can be described as follows. The separation of  $d\Gamma/dx$  from (5.3) reads

$$\frac{d\Gamma}{dx} = \frac{d\Gamma_{0\gamma}}{dx} + \frac{d\Gamma_{\gamma}}{dx}, \quad (5.4)$$

where the first term on the right hand side of the equation is the contribution of the non-radiative part of the process and the second term comes from the radiative process. As I mentioned earlier, the divergences in the two terms cancel each other. The radiative term goes to infinity when the energy of the radiated photon goes to zero. The separation can be done consistently by limiting the second term to energies of the photon larger than a cut-off energy.

The differential decay width with respect to  $E_{\text{vis}}$ ,  $d\Gamma/dx_{\text{vis}}$ , can than be written as

$$\frac{d\Gamma}{dx_{\text{vis}}} = \frac{d\Gamma_{0\gamma}}{dx}(x = x_{\text{vis}}) + \frac{d\Gamma_{\gamma}}{dx_{\text{vis}}}. \quad (5.5)$$

The visible energy is given as fractional energy  $x_{\text{vis}}$ . The first term represents decays with no photon radiated or with photons radiated with energies below the cut-off energy, which is defined by (5.4). The electron energy than approximately equals the visible energy in this case, equaling exactly with limit of zero cut-off energy. The second term is the partial differential decay width of the radiative branch with respect to the visible energy.

The differential decay widths  $d\Gamma_{0\gamma}/dx$  in (5.4) and  $d\Gamma_{\gamma}/dx_{\text{vis}}$  in (5.5) can be calculated from differential branching ratio of the radiative decay process. Calculations from several authors, Kinoshita and Sirlin [67], Eckstein and Pratt [68], and Fronsdal and Überall [69], are nicely summarized by Kuno and Okada in [70].

Differential branching ratio of the radiative process with respect to the energies of the electron and photon has the following form:

$$\begin{aligned} \frac{d^2B}{dx dy} &= \frac{\alpha}{8\pi} \beta \frac{1}{y} \int_{-1}^{\cos\theta_{\text{min}}} F(x, y, d) d \cos\theta \\ &= \frac{\alpha}{8\pi} \beta \frac{1}{y} [F^{(0)}(x, y) + rF^{(1)}(x, y) + r^2F^{(2)}(x, y)]. \end{aligned} \quad (5.6)$$

Here,  $y = 2E_{\gamma}/m_{\mu}$  is the fractional energy of the outgoing gamma photon,  $\theta$  is the angle between the directions of electron and gamma photon,  $d \equiv 1 - \beta \cos\theta$ ,  $\beta$  is the electron's standard relativistic factor, and  $r = (m_e/m_{\mu})^2$ . I derived the formula from Equation (49) in [70], where I considered the muon to be unpolarized. Integrals over the angle  $\theta$  of the individual parts of  $F(x, y, d)$ ,  $F^{(i)}(x, y)$ , are listed in Appendix A.2.

The resulting two dimensional differential branching ratio is plotted in Figure 5.5. The corresponding spectra of individual gamma photon and electron energies are plotted in Figure 5.6. I cross-checked correctness of the calculations

by comparison of the calculated energy spectrum of radiated photons with the the same distribution presented in [70]. The distribution extracted from the publication is also plotted in Figure 5.6a, and it matches the derivation presented here.

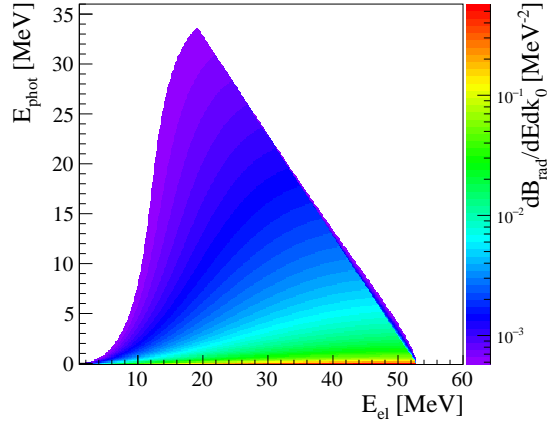


Figure 5.5: Differential branching ratio of the radiative muon decay with respect to the photon energy  $E_{\text{phot}}$  and the electron energy  $E_{\text{el}}$ .

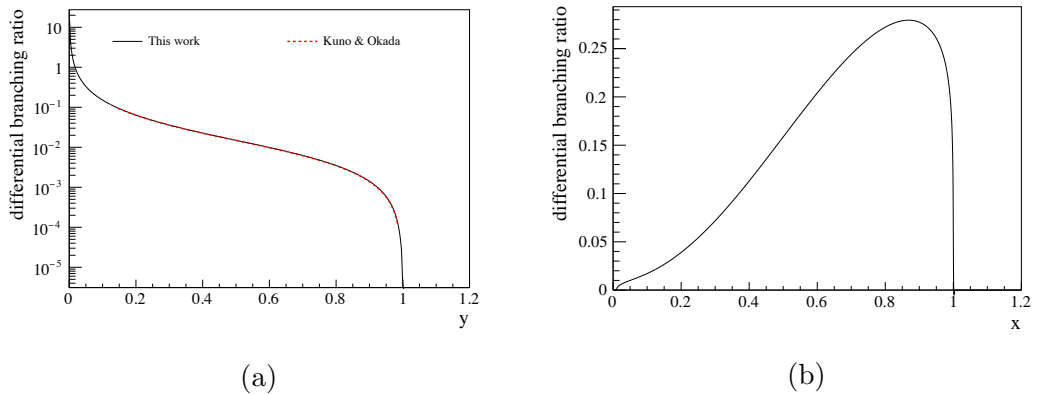


Figure 5.6: Differential branching ratio of the radiative muon decay with respect to the photon energy (a) and electron energy (b). The photon energy spectrum is compared to calculations presented by Kuno and Okada in [70] (red dashed line). For plot (b), photon cut-off energy of 50 keV is used.

## 5.4 Spectrum of visible energy

Using the results of the previous sections, Equation (5.5) can be written as

$$\frac{d\Gamma}{dx_{\text{vis}}} = \frac{d\Gamma_{0\gamma}}{dx} (x = x_{\text{vis}}) + \Gamma \frac{dB_{\gamma}}{dx_{\text{vis}}}. \quad (5.7)$$

$dB_{\gamma}/dx_{\text{vis}}$  is the differential branching ratio of the radiative decay with respect to total fractional energy of the decay electron and photon  $x_{\text{vis}} = x + y$ .

The first term can be calculated as subtraction of the radiative process contribution from (5.3):

$$\frac{d\Gamma_{0\gamma}}{dx} = \frac{d\Gamma}{dx} - \Gamma \int_{y_{\text{cut-off}}}^{y_{\text{max}}} \frac{d^2 B_\gamma}{dx dy} dy, \quad (5.8)$$

where the maximal photon energy  $y_{\text{max}}$  is given by kinematic constraint and the  $y_{\text{cut-off}}$  is the photon cut-off energy which can represent minimal energy of a photon the detector can register. The marginalized differential branching ratio in the second term is plotted in Figure 5.6b.

The second term in Equation (5.7) is obtained from a reordered integral of (5.6):

$$\frac{dB_\gamma}{dx_{\text{vis}}} \equiv \int_{y_{\text{cut-off}}}^{y_{\text{max}}} \frac{d^2 B_\gamma}{dx dy}(x = x_{\text{vis}} - y, y) dy = \int_{x_{\text{min}}}^{x_{\text{max}}} \frac{d^2 B_\gamma}{dx dy}(x, y = x_{\text{vis}} - x) dx \quad (5.9)$$

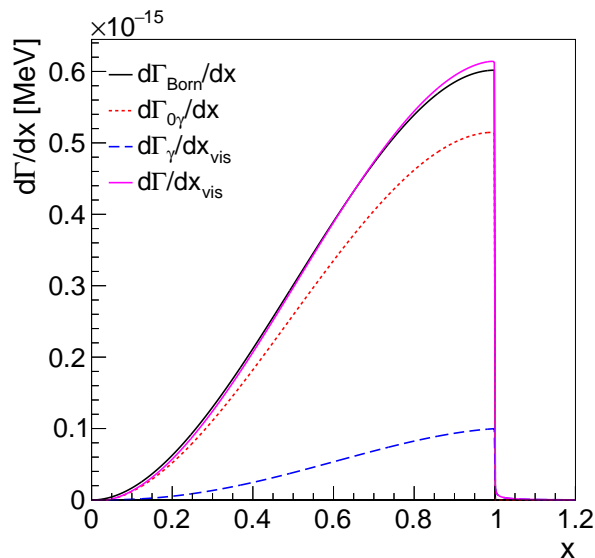


Figure 5.7: Spectrum of total visible energy in muon decay  $\frac{d\Gamma}{dx_{\text{vis}}}$ . Added are parts relevant to the two decay channels considered, non-radiative  $\frac{d\Gamma_{0\gamma}}{dx}$  and radiative  $\frac{d\Gamma_\gamma}{dx_{\text{vis}}}$ .

I performed the integration in (5.8) and (5.9) numerically. The final spectrum of visible energies of (5.7) is plotted in Figure 5.7 together with contributions of the non-radiative and radiative processes. Inclusion of the photon energy to the total visible energy changed the shape of the spectrum of only electrons to match again the simple spectrum of electrons in the Born approximation. There is only minor difference around below and above the edge where the four-body radiative decays can produce more visible energy than is kinematically allowed in the three-body non-radiative decay. As a result, there is a small tail behind the sharp edge.

## 5.5 Decays in orbit

The energy spectra introduced in the previous section apply to decays of the free unpolarized muon. When the muon stops in a medium, however, the situation

is different for negatively charged muons. The muon  $\mu^-$  is quickly captured by surrounding atoms and molecules, taking place of an orbiting electron. The spectrum of energies of the electron from the decay in orbit is different from the spectrum of free-muon decay.

The binding of the muon in orbit affects it in two ways. The muon, due to its large mass and relatively close approach to the atom's nucleus, can be captured by the nucleus, similarly to the electron capture. Such process decreases muon's mean life time. The energy spectrum of the decay electrons is changed due to non-negligible kinetic energy of the orbiting muon, electromagnetic interactions with the nucleus, and recoil of the nucleus.

The binding of the muon to the orbit also changes its apparent decay rate due to the relativistic time dilatation and due to smaller phase space for the decaying products lowered by the binding energy. It slows down the decay rate and therefore influences muon's life time in opposite direction than the nuclear capture does.

Spectrum of electrons from muon decay in orbit—DIO—have been calculated by several authors [71, 72, 73, 74, 75, 76, 77]. I use numerical calculations by Watanabe et al. in [77], which are based on formalism in [76]. The authors solve the problem of the muon decay in the coulomb field of a nucleus, including modeling of spatial distribution of the electric charge of the nucleus.

All the literature, to my best knowledge, presents calculations for oxygen or heavier atoms.<sup>1</sup> The Daya Bay detectors, however, are filled with organic liquid scintillator and mineral oil, and majority of the decays inside the detector happens from the orbit of carbon. Figure 5.8 presents comparison of spectra calculated for DIO of three different atoms. One can see that the spectra of decays from the atom orbits of  $^{28}\text{Si}$  and  $^{27}\text{Al}$  nuclei are, to a good approximation, similar. I will assume that electron spectrum of the decays from the orbit of  $^{12}\text{C}$  is similarly close to the spectrum of the decays from  $^{16}\text{O}$ 's orbit, and under such assumption the calculated spectrum of DIO of oxygen can be used as an approximation to the spectrum of carbon.

In the materials such as organic liquid scintillators, atoms of hydrogen and carbon constitute complex molecules and are of similar abundance. In a very nice review of the topic of muon capture [78], Measday reveals that in organic molecules, the live time of a muon is so long that even when it is initially captured in an orbit of hydrogen, it is eventually caught on the S-orbit of carbon before decaying or capturing.

Czarnecki et al. provide formalism for and calculate energy spectrum of DIO with radiative corrections, [80]. In Figure 5.9 I re-plot their fit to the TWIST[79] data of muon decay in orbit of aluminum. The DIO spectrum without radiative corrections and the spectrum of free muon with radiative corrections are shown, for a comparison. I consider the difference between the DIO with and without corrections to be relatively small and after taking into account that possible radiated photons are also detected in the Daya Bay's detectors,  $\mu^-$  decay can be treated without radiative corrections.

---

<sup>1</sup>Tenaglia [73] gives prescription for calculations for low  $Z$  elements. The prescription, however, is rather complex and no numerical results are given.

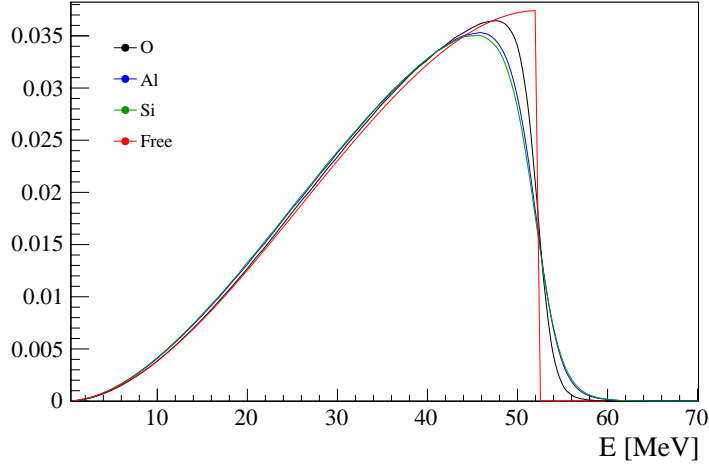


Figure 5.8: Electron spectrum from muon DIO as calculated by Watanabe et al., [77]. Calculation of decays from orbit of oxygen, aluminum, and silicon are compared to the spectrum of free muon decay.

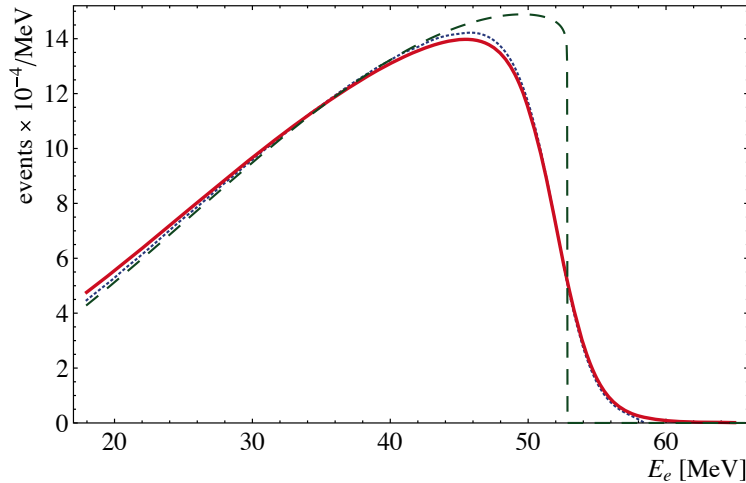


Figure 5.9: Example of spectrum of energies of electrons from muon-decay in orbit of aluminum with the radiative corrections (red), compared to calculations without the corrections (dark blue dotted) and the spectrum of the free muon decay (dark green dashed). The former two curves are extracted from a fit to TWIST[79] measurements. The plot is modified reproduction of the same figure in paper by Czarnecki et al.[80]. I removed the the data points.

## 5.6 Combined $\mu^-$ and $\mu^+$ decay spectrum

Two models of spectrum of visible energy from muon decays were described in the previous sections. Muon  $\mu^+$  decays were described by a simple four-fermion contact interaction and by the same interaction with radiative corrections in the first order of fine-structure constant  $\alpha$ . After inclusion of the process of radiative decay the spectrum of visible energies of the extended model and the spectrum of positron energies of the simple model become very similar.

Spectrum of electrons from decays of  $\mu^-$  in orbit of carbon atoms is modeled

by calculated spectrum of decays in orbit of oxygen.

Muons from cosmic rays have mixed composition of  $\mu^-$  and  $\mu^+$ . The spectrum of visible energies from decays of muons stopping in an underground detector is therefore a combination of free-like muon decays of  $\mu^+$  and decays of  $\mu^-$  in orbit. The combined differential decay width can be expressed as

$$\frac{d\Gamma^\pm}{dx_{\text{vis}}} = \frac{R_\mu}{1 + R_\mu} \frac{d\Gamma^+}{dx_{\text{vis}}} + (1 - f_{\text{cap}}) \frac{1}{1 + R_\mu} \frac{d\Gamma^-}{dx_{\text{vis}}}, \quad (5.10)$$

where  $R_\mu = F_{\mu^+}/F_{\mu^-}$  denotes the ratio of fluxes of positively and negatively charged muons.  $R_\mu$  depends, in general, on energy of muons of interest.  $f_{\text{cap}}$  is the fraction of  $\mu^-$  which does not decay but undergoes the nuclear capture. I discuss both parameters more in Chapter 6.  $d\Gamma^+/dx_{\text{vis}}$  represents the spectrum of visible energy from the free muon decay as described in Section 5.4 and  $d\Gamma^-/dx_{\text{vis}}$  represents the spectrum of  $\mu^-$  decays from carbon S-orbit as described in the previous section.



# 6. Analysis

## 6.1 Rate of Muon Decays

The experimental halls of the Daya Bay experiment are well shielded against cosmic rays by the massive rock overburden above each hall. Mostly only muons created in interactions of primary cosmic rays in the atmosphere can penetrate such bulk of matter. Some of the muons that reach the detectors underground have small energies and stop inside the detector. They can subsequently decay, or, in case of  $\mu^-$ , capture on a nucleus of surrounding matter. The fraction of these low-energy muons is relatively small, about 3% in the near halls and about 1% in the far hall. Different depths of each experimental hall allow to measure the dependence of the rate of stopped-muon decays on the depth of vertical overburden.

In this section, I describe what signals the muon decays produce in the antineutrino detectors and how I selected them. Efficiencies of two main selection criteria are determined. Small fraction of background events is estimated from distribution of time delays between muon and its decay signal. In the final part I present the measured rates of muon decays in antineutrino detectors of each hall.

### 6.1.1 Event Selection

#### Muon Decay Event Topology

Muon decays in the sensitive volume of the antineutrino detectors can be selected based on a delayed coincidence of two signals. The first signal comes from the cosmic muon which stops in the detector and its kinetic energy is converted into scintillation light. The second signal is created by its decay which is delayed in average by about  $\sim 2 \mu\text{s}$ . Up to about 53 MeV of energy is released in the form of kinetic energy of produced electron/positron and more energy is also deposited after positron annihilation and absorption of the produced gamma photons. This energy is then fully converted into the scintillation light.

Pairs of signals coincident in a specific time interval can be studied to obtain clean sample of muon-decay events. Figure 6.1a shows distribution of energies of the prompt and delayed signals of such pairs. The coincidence window for the two signals was set to  $1 \mu\text{s}$  through  $30 \mu\text{s}$ . The prompt signal was required to be coincident with a signal in the inner water shield (IWS). A muon veto was applied to the delayed signal by requiring that there was no coincident signal in any of the muon system detectors (RPC, IWS, OWS). I will describe muon selection and application of muon veto in the following section.

There is region of muon decays in the plot, where the reconstructed energy of the first signal spans up to about 1 GeV and the reconstructed energy of the second signal goes to about 60 MeV. Given that the longest distance a muon can travel in a scintillator volume is about 5.5 m and that minimum-ionizing particle loses approximately 2 MeV per cm, the expectation is that a passing muon deposits about  $5.5 \times 10^2 \times 2 \text{ MeV} = 1.1 \text{ GeV}$ . The observed maximal reconstructed energy does not equal the expected energy deposition due to various reasons, namely nonuniform response of the detector, electronics nonlinearity, and

reconstruction method not optimized for long muon tracks with large deposited energies.

The line corresponding to energy of the delayed signal of about 8 MeV is related to a neutron capture on gadolinium. These neutrons are associated with the detected muon and they originate either in a spallation process initiated by the muon or in a capture of stopped  $\mu^-$  on carbon nucleus. Similar line around  $E_{\text{delayed}} = 2$  MeV from neutron captures on hydrogen is hidden in events caused by electronics effects soon after the large prompt signals in AD.

Figure 6.1b shows the same distribution, but the pairs of signals were required to be separated in time by at least 10  $\mu\text{s}$ . The 2 MeV line is visible.

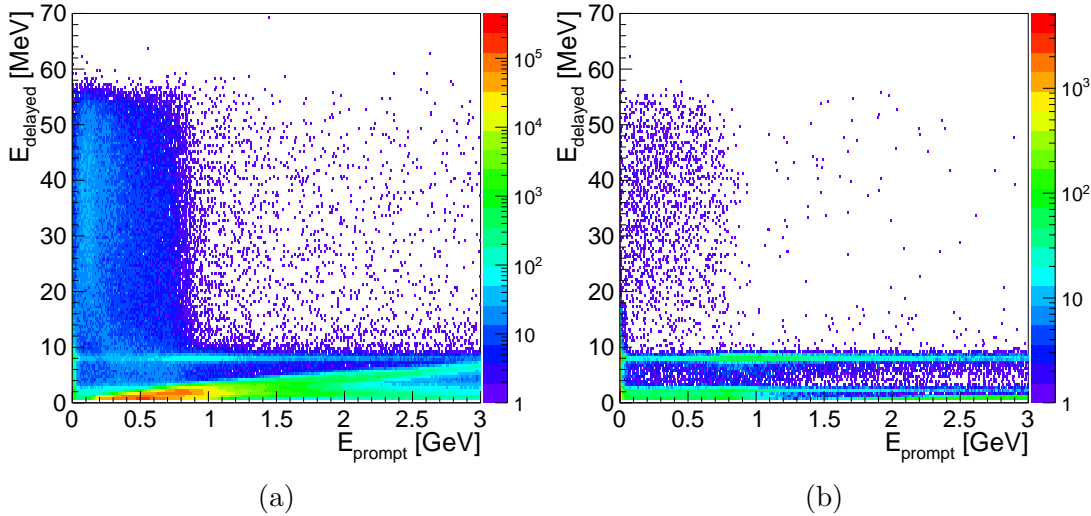


Figure 6.1: Distribution of energies for pairs of signals correlated in time interval 1  $\mu\text{s}$  through 30  $\mu\text{s}$  (a). The delayed signal was vetoed if there was a coincident signal in any of the muon system detectors. Muon decay events are visible in the region up to 1 GeV of the prompt signal and they reach to about 60 MeV in the delayed signal energy. Signals which were separated by at least 10  $\mu\text{s}$  are plotted on the right hand side of the figure (b). Horizontal lines from captures of neutrons associated with the detected muon are visible at  $E_{\text{delayed}} \approx 8$  MeV and  $E_{\text{delayed}} \approx 2$  MeV. Signals from retriggering of the detector after very luminous event are no longer present after 10  $\mu\text{s}$ .

## Muon Selection

The muon signal is selected as a two-fold coincidence between triggers in AD and IWS. The IWS trigger is required to arrive in a window of  $[-350 \text{ ns}, 350 \text{ ns}]$  around the AD trigger. This requirement suppresses noise in AD signals and allows to study events with low reconstructed energy.

Coincidences with other detectors were not required as they are assumed unnecessary and they would bring geometrical bias to the muon selection. The RPC system lies above the water pool and it would not see muons arriving from the sides. The OWS does not cover the top of the pool, therefore it could only see muons coming from the sides. Moreover, many vertical muons which stop in AD, never reach the OWS.

Muons that stop in the AD can have various path lengths in the scintillator. The maximal length in scintillator is given by the diagonal in the outer acrylic vessel and data suggest that this distance corresponds to maximal reconstructed energy of  $\sim 1$  GeV. However, more energy can be deposited in the detector, leading to signals with reconstructed energy larger than 1 GeV. Very energetic muons can interact via photo-nuclear interactions and they can generate energetic nuclear fragments or a shower of particles. The shower can be initiated in the detector or outside, but if it reaches the detector it produces large signals. Events with reconstructed energies above 2.5 GeV are in analyses of Daya Bay generally considered as coming from these cosmic ray-induced showers.

I require the muons to be only ionizing and stop in the detector. I therefore chose only signals with reconstructed energy below 1 GeV.

The showering muons that create large signals in AD also produce large signals in IWS. Effects related to electronics and PMTs can cause re-triggers of IWS as well as of AD. These re-triggers can then overlap thanks to the similar time profile for both detectors, or the re-trigger of IWS overlaps with a physical signal in AD. In both cases, they appear as muon events. A special veto was applied where no other muons were selected in the time of 100  $\mu$ s after showering muons. Although I consider this veto conservative, as most of the effects were observed in the first 10  $\mu$ s after a shower, it has marginal impact on the live time or the final selection.

## Decay Signal Selection

Any signal which followed the prompt muon signal was rejected if it was in coincidence with any of the veto detectors, RPC, IWS, and OWS. The triggers from IWS and OWS were required to have at least 13 PMTs hit, whereas any trigger from RPCs was used as a veto. The time windows in which the signals from the veto detectors were considered coincident are listed in Table 6.1.

Detector	Coincidence time window	veto condition
IWS	−350 ns, 350 ns	>12 PMT
OWS	−350 ns, 350 ns	>12 PMT
RPC	−600 ns, 600 ns	any 3/4 or 4/4 trigger

Table 6.1: Table of requirements on coincidence of a signal in AD with signals in muon system detectors—RPC, inner water shield (IWS), and outer water shield (OWS). Signal in the muon detector should be within the time interval listed in second column. Third column lists condition on the signal to be considered a veto to the signal in AD.

The actual decay of the muon was recognized as a signal in AD with reconstructed energy in between 20 MeV and 60 MeV. I selected the lower bound to avoid any contamination from captures of neutrons on gadolinium. Such neutrons are commonly associated with muon events and the signals from the captures are dominant in the region around 8 MeV. The tail from the capture peak extends above 10 MeV. There is also a small fraction of events with pile-up of 2 neutron captures on Gd that contaminate the energy spectrum of the muon decays around 16 MeV.

The higher bound cuts off a very small fraction of events that extend this energy. The only known source of these signals are cosmic rays. Since signals from muons are rejected by the veto detectors, these signals are attributed to fast neutrons that originated outside the pool and penetrated into AD.

As already mentioned, large signals in AD generate multiple effects in the PMT readouts. There is always ringing after a PMT pulse. Its amplitude decays approximately exponentially in time. Then there is PMT after-pulsing which is seen to take place at around 6–8  $\mu\text{s}$  after the large signal.

These effects produce readout triggers of the system even though there was no physical event in the detector. These triggers may completely hide any possible physical event in the AD, or they can distort its reconstructed energy due to baseline distortion or due to limits of readouts of individual PMTs.

When looking at the time distribution of selected events after detected muons, in Figure 6.2, one can see the distortion it up to about 9  $\mu\text{s}$ , with small residual distortions lasting throughout the full range. I chose to discard events with  $\Delta T < 10 \mu\text{s}$ . Muon decays were then selected as a coincidence of the muon signal and subsequent decay signal in time window 10–30  $\mu\text{s}$ .

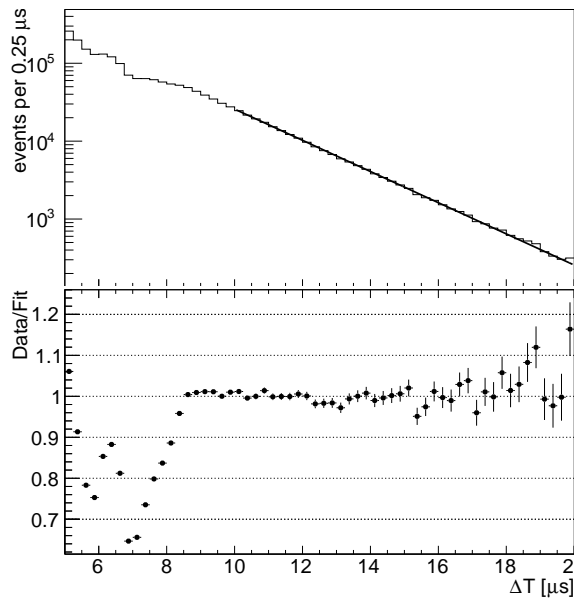


Figure 6.2: Distribution of time difference  $\Delta T$  between prompt and delayed signal for selected pairs of muon-decay candidate events. Both signals satisfy individual selections described in this section. The distribution is fitted with simple exponential function from 10  $\mu\text{s}$  through 20  $\mu\text{s}$ . Bottom plot represents ...

### Additional selection requirements

In addition to the basic criteria outlined in the previous paragraphs, events with more candidates for either muon signals or muon-decay signals were discarded. In particular, a successful decay candidate was removed if there was another muon identified closer than 20  $\mu\text{s}$  prior to the candidate muon. This requirement prevents double counting of muon-like events correlated with large signals in AD and IWS.

## Accidental-coincidence Background

Since the rates of muons in ADs are relatively small the probability of an accidental overlap of a muon signal with a decay signal of another muon is very low. Rates of muon-like signals in each AD in EH1, EH2, and EH3 are around  $\sim 20 \text{ s}^{-1}$ ,  $\sim 15 \text{ s}^{-1}$ , and  $\sim 1 \text{ s}^{-1}$ , respectively. Probability, that an accidental muon signal occurs in the time interval of  $[-30 \mu\text{s}, 10 \mu\text{s}]$  before actual decay of another muon can be estimated as the product of the muon rate and the width of the time interval. For EH1, this is  $20 \text{ Hz} \times 20 \mu\text{s} = 4 \times 10^{-4}$ . This means that less than a half per-mile of all the muon decays happened in the short interval after another muon signal. The pairs of signals from the accidental muon and the muon decay are accepted by the selection criteria since they pass the requirement on  $\Delta T$ . The decay is not counted twice, because either the decaying muon created a signal in less than  $10 \mu\text{s}$  before the decay signal or the time difference between the two muons is less than  $20 \mu\text{s}$ .

Assuming the efficiency of the  $\Delta T$  selection is around 1%, which reduces the number of selected decays, but does not reduce the estimated accidental overlap of two muons, the contamination of the sample of muon decays in EH1 with the accidental coincidences is then around  $\sim 4\%$ . Correspondingly, the accidental background is  $\sim 3\%$  and  $\sim 0.2\%$  in EH2 and EH3, respectively.

Actual contamination of the selected samples is determined from  $\Delta T$  distribution and the results are described later on in this section.

### 6.1.2 Selection Efficiency

Each of the data selections described above introduces inefficiency which needs to be taken into account when calculating the final rate of muons decaying in the detector. Due to the short mean muon lifetime  $\tau_\mu \simeq 2.2 \mu\text{s}$  as opposed to the used time window for selection of the decay signal and which starts at  $10 \mu\text{s}$ , inefficiency of this selection is the largest one. The inefficiencies of the respective requirements on the energy of the muon and its decay signals are much smaller, and the inefficiency of the requirement that there was no other muon  $20 \mu\text{s}$  prior to the current muon event has negligible contribution. I will first discuss differences of mean lifetimes of  $\mu^+$  and  $\mu^-$  and how they impact distribution of time between the muon signal and the muon-decay signal,  $\Delta T$ . Then, I will describe estimations of the time and energy selection efficiencies and corresponding uncertainties.

### Muon Mean Lifetime, Capture rate, and Charge Ratio

The sample of selected events consists of decays of  $\mu^+$  and  $\mu^-$ . The mean lifetime of the muon in vacuum is measured  $\tau_\mu = 2.19698 \mu\text{s}$ [20]. In matter, this value applies to decays of the positively charge muons. However, the negatively charged muons have lifetime slightly modified in the scintillator due to their captures on atomic orbits of the compounds of the material and possibility of being capture by the nucleus. The effective decay rate  $\lambda_{\text{tot}} = 1/\tau_\mu^-$  can be expressed as

$$\lambda_{\text{tot}} = \lambda_{\text{cap}} + Q \times \lambda_{\text{dec}}, \quad (6.1)$$

where the  $\lambda_{\text{cap}}$  is the rate of muon capture,  $\lambda_{\text{dec}} = 1/\tau_\mu^+ = 455.17 \text{ ms}^{-1}$  is its decay rate in vacuum and  $Q$  is the so called Huff factor[74]. In [78] Measday discusses

effect of binding energy and relativistic time dilatation of orbiting muons. These effects reduce the decay rate of a muon and are commonly corrected for by the Huff factor  $Q$ . However, the measurements listed by Measday in the same publication suggest that this correction can be neglected for light nuclei like that of carbon. The author also notes that any capture on a nucleus in organic compounds, which is the case of Daya Bay scintillator, happens on the carbon nucleus. The reason is that if the muon created a muonic atom with the hydrogen nucleus, the charge neutrality of the atom would allow it to come close to a carbon atom and the muon is then transferred to the higher  $Z$  nucleus due to its stronger binding energy.

The Daya Bay liquid scintillator is mainly made of LAB (linear alkylbenzen) which is pure organic compound of hydrogen and carbon. There are also other admixtures, like PPO (2,5-diphenyloxazole) and dissolved gadolinium salt (compound of Gd and 3,5,5-trimethylhexanoic acid), which may change the effective capture rate. These admixtures are of low concentrations and therefore their effect is small.

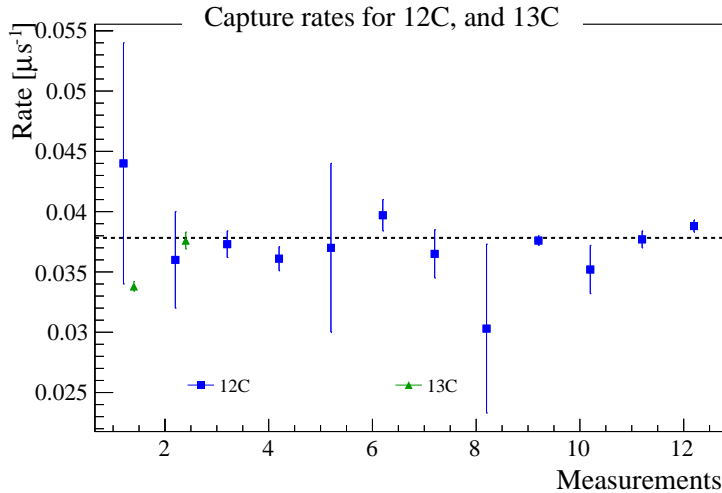


Figure 6.3: Measurements of  $\lambda_{\text{cap}}$  as listed in [81]. A weighted average of the values for  $^{13}\text{C}$  (blue squares) is represented by the dashed line. Two measurements of  $^{13}\text{C}$  are also shown (green). They were not included in the estimation of  $\mu^-$  capture rate on carbon.

The capture rate on carbon has been measured by various experiments and the results are listed in [81]. Figure 6.3 shows the measurements and their errors for  $^{12}\text{C}$  and  $^{13}\text{C}$ . Since the natural abundance of  $^{13}\text{C}$  is very low and the measured capture rates do not differ much, I only consider the measurements of  $^{12}\text{C}$ . The weighted average of the  $^{12}\text{C}$  points in the plot is  $\lambda_{\text{cap}} = 37.8 \pm 0.3 \text{ ms}^{-1}$ .

Ratio of charge of muons in cosmic rays  $R_\mu$  has also been measured by several experiments. Its variation with cosmic muon momentum measured by BESS-TeV[82], CMS[83], L3[84], and MINOS[85] is plotted in Figure 6.4. The results of these measurements are translated to momenta of muons at surface. The ratio is relatively stable around 1.3 through out two orders of magnitude in the muon's momentum. CMS collaboration reports[83] average value of  $1.2766 \pm 0.0032(\text{stat.}) \pm 0.0032(\text{syst.})$  between 5 GeV/c and 100 GeV/c and they state that the value is independent of the muon momentum.

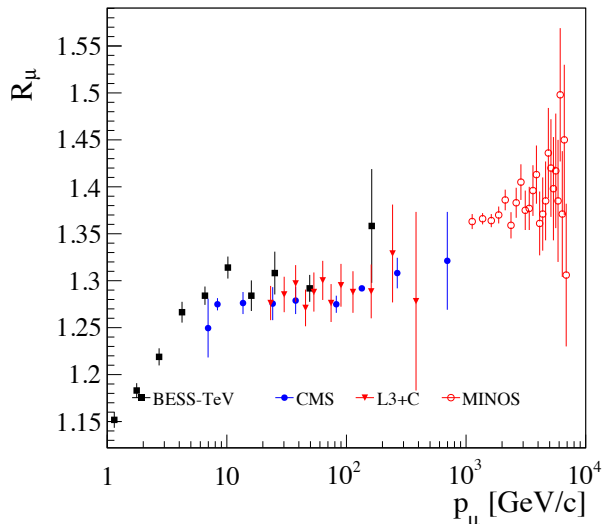


Figure 6.4: Charge ratio of muons on the surface as measured by various experiments. The ratio is plotted with respect to the muon momentum  $p_\mu$ . Figure is reproduction of similar plot in [20]. Data are processed from [82, 83, 84, 85]. Equivalent momenta of muons stopped in ADs of Daya Bay’s three experimental halls are indicated.

In order to be able to identify muon energies at the surface level of the muons which can stop in the Daya Bay underground detectors, I used data from simulations. My colleagues Guan Mengyun et al.[40] simulated muons from the surface at the Daya Bay site through the mountains above the experimental halls. Detailed topographical maps of the hilly environment were taken into account. Muons with initial energies distributed according to a modified formula of Gaisser[39] were propagated through different slant depths of the rock. The modification of the classical formula for muon flux enlarged the region of its validity to larger zenith angles. Transportation through the rock was simulated via specialized software package MUSIC[86, 87] which is designed specifically for simulation of muon interactions.

The final data of the simulation, which consists of samples of one million simulated muons in each experimental hall, includes the muon’s initial and final energy and incident angle. I selected muons which had final energies below 5 GeV after reaching the experimental hall. These muons are most likely to stop inside or near to the antineutrino detectors. Distributions of their corresponding initial energies at the surface level are plotted in Figure 6.5. The peak energies of these muons are indicated in Figure 6.4 and are all well within the range of apparent stability of  $R_\mu$ .

I will use a constant value of the charge ratio  $R_\mu = 1.3 \pm 0.1$  in the following. The large assigned uncertainty is based on the small deviation of MINOS data above  $10^3$  GeV/c from the trend for momenta below  $10^3$  GeV/c and on the deviations of measurements by different experiments. Although they appear to be consistent within the stated errors, there still seems to be systematic offset between each data set.

Due to the different lifetimes of  $\mu^+$  and  $\mu^-$ , the composition of a sample of decays depends on selected time  $\Delta T$  since the muon signal. The number

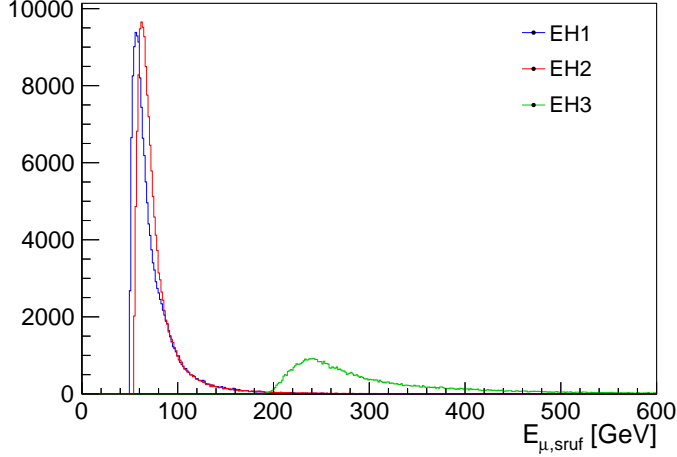


Figure 6.5: Distribution of surface energies of muons with energies lower than 5 GeV in each experimental hall. Data are from MC simulations which propagated muons through the overburden surrounding the Daya Bay experimental halls.

of stopped muons that survived  $\Delta T$  after stopping can be expressed with the following formula:

$$N(\Delta T) = N_0^+ e^{-\lambda_{\text{dec}} \Delta T} + N_0^- e^{-\lambda_{\text{tot}} \Delta T}. \quad (6.2)$$

$N_0^\pm$  is the total number of stopped muons of respective charge and  $R_\mu = N_0^+ / N_0^-$ . The ratio of  $\mu^+$  and  $\mu^-$  in the events selected with  $\Delta T > \Delta T_{\text{cutoff}}$  is then

$$R_\mu(\Delta T_{\text{cutoff}}) = R_\mu e^{\lambda_{\text{cap}} \Delta T_{\text{cutoff}}} \quad (6.3)$$

The observed spectrum of reconstructed energies of the muon decays differs for decays of  $\mu^+$  and  $\mu^-$ . Therefore the combined spectrum will change depending on the selection of  $\Delta T$ .

### Prompt and Delayed Signal Time Difference

The efficiency of selection of time difference  $\Delta T$  between the prompt muon signal and the delayed decay signal is defined as ratio of number of decays selected in the given time window to the total number of decays  $\epsilon_{\Delta T} = N_{\text{dec}}^{10\mu\text{s}} / N_{\text{dec}}$ .

Using relation (6.2), the number of decays after time  $\Delta T$  for  $\mu^+$  and  $\mu^-$  can be expressed as follows:

$$\begin{aligned} N_{\text{dec}}^+(\Delta T) &= N_0^+ e^{-\lambda_{\text{dec}} \Delta T} \\ N_{\text{dec}}^-(\Delta T) &= N_0^- \frac{\lambda_{\text{dec}}}{\lambda_{\text{tot}}} e^{-\lambda_{\text{tot}} \Delta T} \end{aligned} \quad (6.4)$$

Here the factor  $\lambda_{\text{dec}} / \lambda_{\text{tot}}$  stands for the fraction of  $\mu^-$  which decay.

Taking into account that  $N_0^\pm = f^\pm N_0$  where  $N_0$  is the total number of stopped muons and  $f^\pm$  is the fraction of muons with the respective charge, efficiency of the  $\Delta T > 10 \mu\text{s}$  selection is then calculated as

$$\epsilon_{\Delta T} = \frac{f^+ e^{-\lambda_{\text{dec}} 10 \mu\text{s}} + \frac{\lambda_{\text{dec}}}{\lambda_{\text{tot}}} f^- e^{-\lambda_{\text{tot}} 10 \mu\text{s}}}{f^+ + \frac{\lambda_{\text{dec}}}{\lambda_{\text{tot}}} f^-}. \quad (6.5)$$

I performed test of agreement of the  $\mu^-$  capture rate in the Daya Bay liquid scintillator with the measurements of capture on carbon described in the previous section. I fitted an expected distribution of  $\Delta T$  to data.

The expected distribution of events with respect to the time difference  $\Delta T$  between the muon signal and its delayed decay is derived from (6.2):

$$\begin{aligned}\Delta N_i &= \Delta N_i^+ + \Delta N_i^- + B \\ &\doteq N_0^+ \lambda_{\text{dec}} \Delta_{\text{bin}} e^{-\lambda_{\text{dec}} t_i} + N_0^- \lambda_{\text{dec}} \Delta t e^{-\lambda_{\text{tot}} \Delta T_i} + B \\ &= N_0 \lambda_{\text{dec}} \Delta_{\text{bin}} e^{-\lambda_{\text{dec}} \Delta T_i} (f^+ + f^- e^{-\lambda_{\text{cap}} \Delta T_i}) + B.\end{aligned}\quad (6.6)$$

$\Delta N_i$  is the number of events detected in a time interval  $[\Delta T_i - \Delta_{\text{bin}}/2, \Delta T_i + \Delta_{\text{bin}}/2]$  and  $\Delta_{\text{bin}}$  is the width of the bin. The approximation used on the second line is valid for bin widths smaller than the decay time of the muon,  $\lambda_{\text{dec}} \Delta_{\text{bin}} \ll 1$ .  $N_0^\pm$  are defined in Equations (6.4) and  $N_0$  is a the total number of muons stopped in the detector before they decayed or were captured.  $B$  is additional background from accidental coincidence of uncorrelated signals.

I used two samples of muon decay events in ADs of EH1. The first one was with the nominal selection described in the Section 6.1.1 and I performed the fits in the  $\Delta T$  range from 10  $\mu\text{s}$  to 29  $\mu\text{s}$ . In the second sample, I changed the requirement on the reconstructed energy of the prompt muon signal and I limited the energy to be in between 6 MeV and 20 MeV, instead of the nominal range between 20 MeV and 1 GeV. These events showed much smaller distortions in the signal after the detected muon. This data sample allowed me to test the expected  $\Delta T$  distribution at times between 2  $\mu\text{s}$  and 20  $\mu\text{s}$ .

While events from the nominal selection are distributed relatively uniformly throughout the detector volume, the second sample with strict limits on muon energy contained events whose decay signals were reconstructed by the edge of the liquid scintillator. This is demonstrated in Figure 6.6.

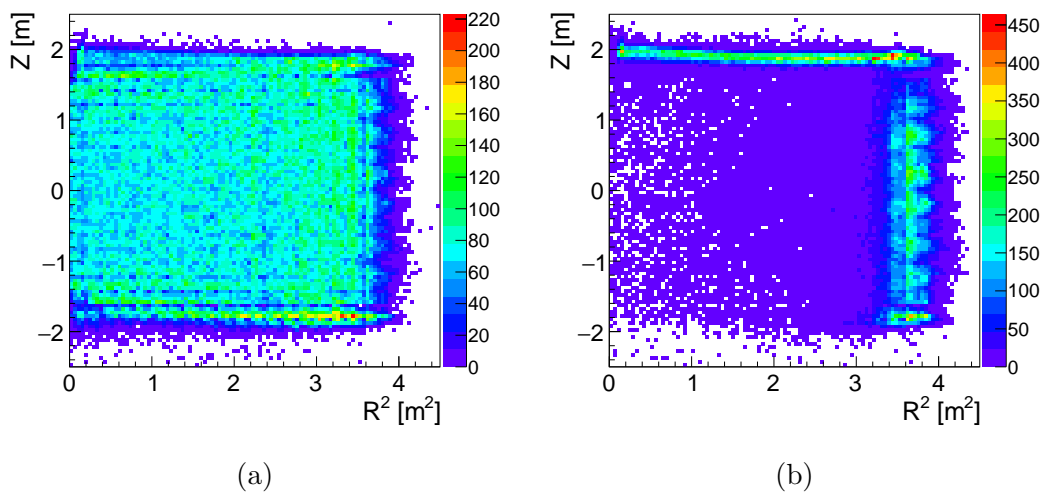


Figure 6.6: Spatial distribution of muon decays in the detector. Decay vertex is reconstructed from the delayed signal from nominal selection (a) and from the selection with strict limits on muon signal energy (b).

I performed the fits using a binned maximum-likelihood method implemented

in ROOT analysis package[88]. I left the  $\mu^-$  capture rate  $\lambda_{\text{cap}}$ , the overall normalization  $N_0$  and background  $B$  as free parameters and I fixed the muon charge ratio and muon decay rate to  $R_\mu = 1.3$  and  $\lambda_{\text{dec}} = 455.17 \mu\text{s}^{-1}$ . The  $\Delta T$  distribution of events from EH1 are shown in Figures 6.7 and 6.8 together with the best-fit function (6.6). Events from AD1 and AD2 are combined together.

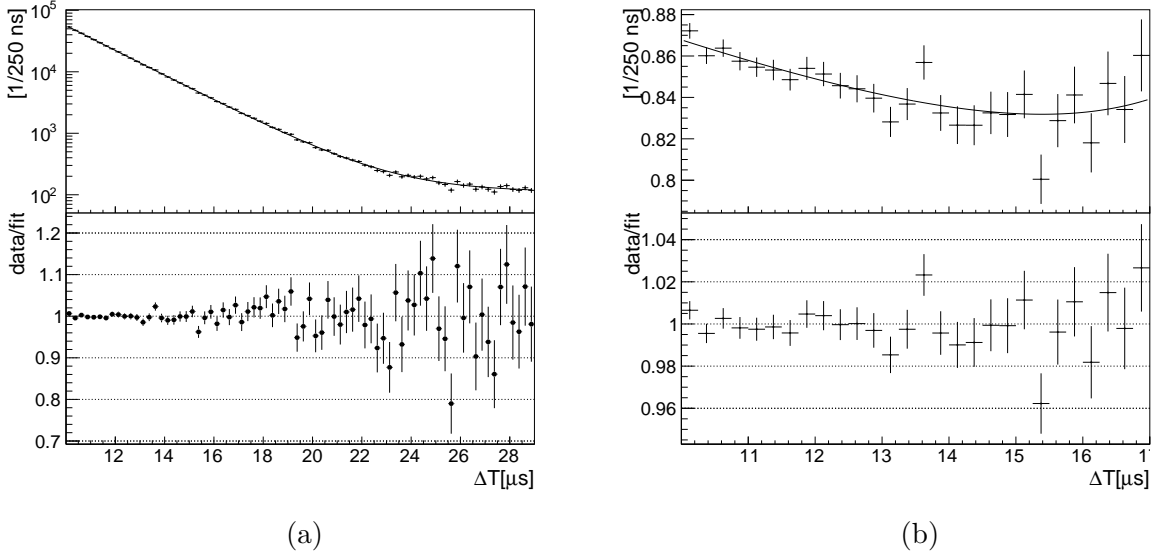


Figure 6.7: Distribution of the time of the second signal since the detected muon for events from nominal selection. Data were fitted with composed exponential distribution defined in (6.6).

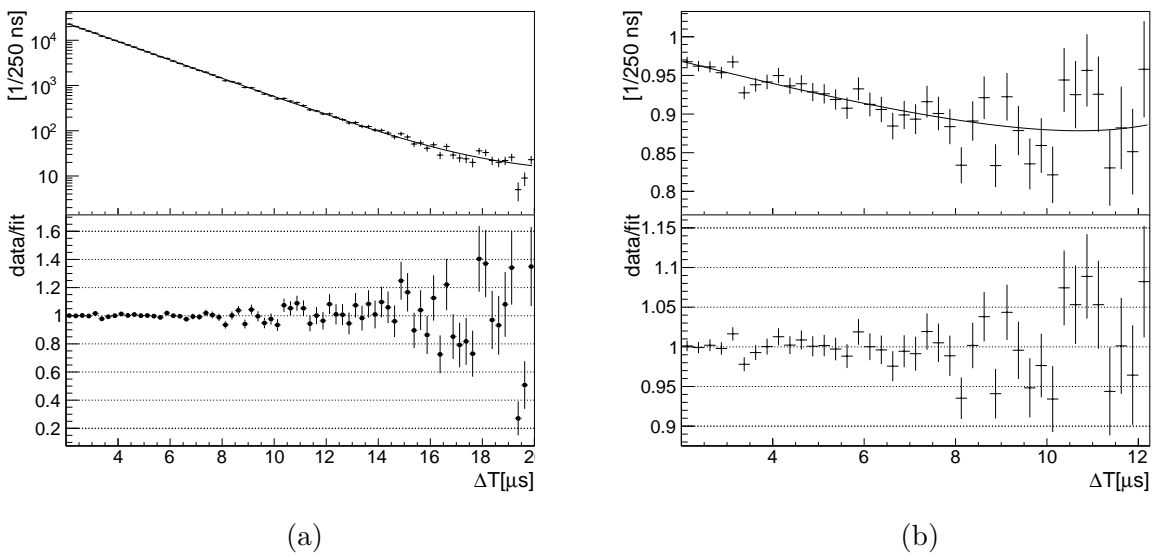


Figure 6.8: Distribution of the time of the second signal since the detected muon for events from selection with strict limit on muon signal. Data were fitted with composed exponential distribution defined in (6.6).

For a better visualization of the effect of  $\mu^-$  capture, I also plotted the histograms and the corresponding function divided by all the common factors for  $\mu^+$  and  $\mu^-$  parts in Equation (6.6),  $N_0\lambda_{\text{dec}}\Delta_{\text{bin}}$ . The corresponding function which describes the content of each bin is then expressed as

$$\frac{\Delta N_i}{N_0\lambda_{\text{dec}}\Delta_{\text{bin}}}e^{\lambda_{\text{dec}}\Delta T_i} = (f^+ + f^-e^{-\lambda_{\text{cap}}\Delta T_i}). \quad (6.7)$$

The slope in both figures, 6.7b and 6.8b, is given solely by the capture rate of negatively charged muons and their initial fraction  $f^-$ .

I repeated the fit procedure and fixed  $R_\mu$  to the estimated maximal and minimal values 1.4 and 1.2, respectively, and compared how the estimated capture rate shifted. Best-fit values of  $\lambda_{\text{cap}}$  based on data from EH1 and EH2 are plotted in Figure 6.9.

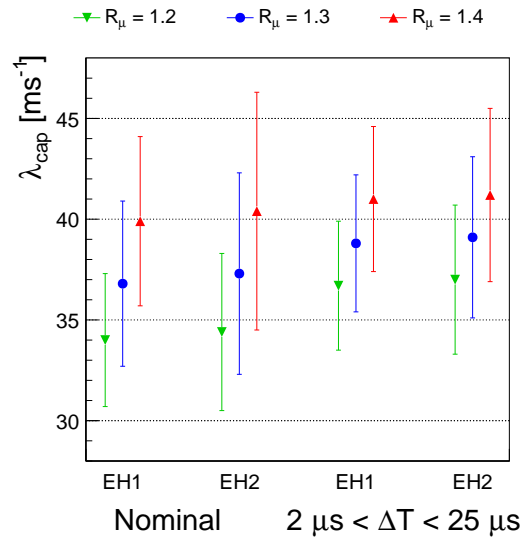


Figure 6.9: Best-fit parameter  $\lambda_{\text{cap}}$  from fits to data from EH1 and EH2. Fits were performed with different fixed values of muon charge ratio  $R_\mu$  and for the nominal-selection data sample and sample with muon-signal energies limited below 20 MeV. The latter data sample was fitted in  $\Delta T$  range from 2  $\mu\text{s}$  to 25  $\mu\text{s}$ .

I calculated the  $\epsilon_{\Delta T}$  efficiency using the nominal values of the parameters  $R_\mu$  and  $\lambda_{\text{cap}}$  and I estimated its uncertainty from differences of calculated  $\epsilon_{\Delta T}$  with  $R_\mu = 1.2, 1.4$  and the corresponding best-fit  $\lambda_{\text{cap}}$ . On top of this systematic uncertainty I also added a statistical uncertainty of the best-fit  $\lambda_{\text{cap}}$ . I therefore determine efficiency of the  $\Delta T$  selection as  $\epsilon_{\Delta T} = (0.917 \pm 0.005 \pm 0.018)\%$ .

## Background

The fit procedure in the previous section also estimated the background contamination of the sample. The total contamination in the selected time interval as well as the relative contribution to the selected sample are listed in Table 6.2.

In Section 6.1.1, I described possible contamination of accidental coincidence of muon with another decaying muon. The estimates of relative contributions of this background are also listed in Table 6.2. The observed background in

EH1 and EH2 is about 2 times lower than predicted in Section 6.1.1. This is to be expected, since the source of the second signal is a real decay and it mostly happens immediately after the corresponding muon stops. Many of these decay signals, however, miss being reconstructed properly, either due to a dead time of the electronics readout of  $\sim 1 \mu\text{s}$  or due to the distortions of signals after events with large light emission.

The observed background in EH3, however, appears to be about 4 times higher than estimated which points to other mechanisms of creation signals either uncorrelated in time or correlated with large characteristic time difference. Although the origin of this background in EH3 is unknown, the observed contribution is very low and I assign it 100% relative uncertainty.

Hall	Bkg.[ $\mu\text{s}^{-1}$ ]	Rel. bkg.[%]	Est. bkg. [%]
EH1	$446.6 \pm 9.7$	$1.81 \pm 0.04$	4
EH2	$240 \pm 11$	$1.38 \pm 0.06$	3
EH3	$3.1 \pm 1.1$	$0.3 \pm 0.1$	0.2

Table 6.2: Background estimation based on fit to distribution of time differences  $\Delta T$  between the prompt muon signal and its decay signal. Contamination per  $1 \mu\text{s}$  of the selected interval is in the second column. Fraction of the total count of events in the interval  $10 \mu\text{s}$  through  $30 \mu\text{s}$  is listed in the third column. Simple estimates from Section 6.1.1 are in the last column.

### Delayed signal energy selection

The delayed signal energy selection criterion,  $20 \text{ MeV} < E_{\text{dec}} < 60 \text{ MeV}$ , discards primarily muon decays in which the kinetic energy given to the produced electron or positron was below the 20 MeV threshold. If the muon decay happened near the edge of a scintillator volume or outside of it, part of the energy of the electron or positron was lost in non-scintillating material like the acrylic vessels or mineral oil in the outer most layer. Such events may have not passed the selection even though the initial kinetic energy of the electrons or positrons was sufficient. Response of the detector nonuniform in volume, and energy resolution brought small effect into the inefficiency of the  $E_{\text{dec}}$  selection.

Only negligible amount of muon decays would be reconstructed with energies above 60 MeV. This can be seen on the energy spectrum of selected events in Figure 6.10. There may be very small number of muon decays where the deposited energy could exceed 60 MeV due to the inner bremsstrahlung, where there was a gamma photon emitted together with the decay electron or positron. Some electrons from decay of  $\mu^-$  in orbit could also cross the 60 MeV limit. Both effects are described in Chapter 5. Due to the lack of evidence of such events I assign 100% efficiency to the upper limit on the muon-decay signal reconstructed energy,  $E_{\text{dec}} < 60 \text{ MeV}$ .

I used two methods to estimate the efficiency of the  $E_{\text{dec}} > 20 \text{ MeV}$  selection. The first method relies on MC simulations and the second method estimates the efficiency from real data. The MC simulation addresses the issue of loss of energy to insensitive regions and it better estimates overall detector response to the

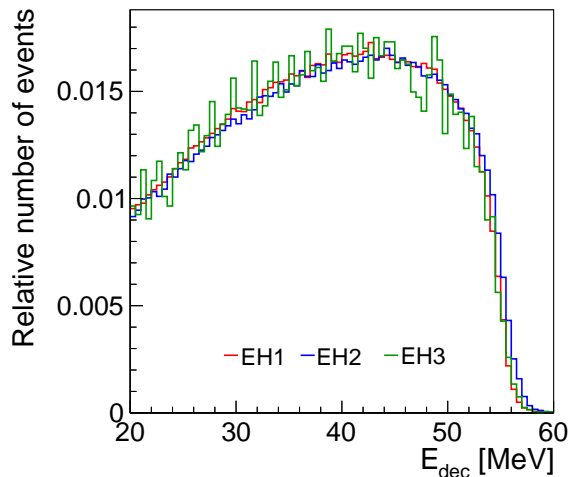


Figure 6.10: Spectrum of reconstructed energies of muon-decay signals. Data from all three halls with nominal selection are plotted.

muon-decay signal. Disadvantage of this method is that it relies on simulation software which was optimized mainly for processes at the energy scale relevant for the neutrino oscillation analysis, i.e. up to 12 MeV. Moreover, a simplified model is used for the muon decays which does not consider inner bremsstrahlung and it only considers relativistic boosts of  $\mu^-$  decaying in the orbit of an atom, neglecting the effect of electromagnetic field and recoil of the atom. This simplification of the decay process affects the calculated efficiency very little and its contribution was completely neglected.

A fit to data allows to tune the model of the muon-decay process to best match the observed energy spectrum. However, the shape of the spectrum is in large given by the detector related effects as described in the previous paragraphs.

**MC simulation of muon decays:** A dedicated MC simulation study was performed to address the question of how many decay events can be selected in the given range of reconstructed energies. The simulation was performed using Daya Bay’s simulation software framework in which particle interactions and propagation is simulated by Geant4 toolkit[89]. The full geometry of the antineutrino detector is replicated in the framework. The simulation included tracking of scintillation and Cherenkov photons. The response of the photomultipliers to the light was then simulated from initial hit of the photons to creation of electronic signal and its digitization. Energies of the simulated events were reconstructed using the same methods that were used for processing of the real data.

I created two batches of simulations, one for negatively charged muons and one for positively charged muons. Muons with 1 keV/c momentum were generated through out the full volume of AD. Decays of positively charged muons are implemented in the Geant4 code such that they decay immediately after stopping, releasing two neutrinos and a positron. The kinetic energy of the positron is generated from the standard formula of of muon decay in Born approximation, discussed in Chapter 5.

Negatively charged muons are captured on an atom orbit after they stopped. About 92% of them decayed, the rest of them were captured by the nucleus. Geant4 code calculates energies of the decay electrons in three steps. First, the kinetic energy of  $\mu^-$  at the lowest atomic shell is calculated. Second, kinetic energy of the decay electron in the rest frame of the muon is generated from the same distribution as in the case of  $\mu^+$  decay. In the third step, the energy is transformed to the lab frame, assuming uniform random direction of the electron relative to the original direction of orbiting muon.

I have combined the two simulated samples in the expected ratio of  $\mu^+$  and  $\mu^-$   $R_\mu$ . As discussed in Section 6.1.2, the charge ratio changes with time due to the different lifetimes of  $\mu^+$  and  $\mu^-$ . Selection applied to data limits the second decay signal to happen at least 10  $\mu\text{s}$  after the muon signal. The expected charge ratio  $R_\mu = 1.3$  which is valid for muons entering the detectors, changes after 10  $\mu\text{s}$  to  $R_\mu \approx 1.9$ . I added the  $\mu^-$  sample to the  $\mu^+$  sample with a weight reflecting their expected ratio and the size of each sample.

The simulations do not show the same energy response to the muon-decay events as seen in data. Figure 6.19a shows comparison of energy spectrum from real data to the spectrum from MC simulation. Many parameters in the detector simulation had been modified so that simulations of regular Daya Bay calibration sources and physics events matched the measurements. This tuning aimed to have best match of detector response at the energies relevant to the neutrino oscillation analysis. There is, however deviation from observations at higher energies.

The comparison to muon-decay data suggested that a simple energy re-scaling would suffice to match simulations to the measurement. I rescaled the original MC reconstructed energy to  $E_{\text{new}}^{\text{MC}} = \text{Scale} \times E_{\text{orig}}^{\text{MC}}$  by minimizing the sum of squared differences between the bin contents of the data and MC histograms weighted by their statistical errors. Figure 6.19b shows the two spectra after the re-scaling to the MC reconstructed energies. The scale which was found to best match the two histograms is  $\approx 0.98$ .

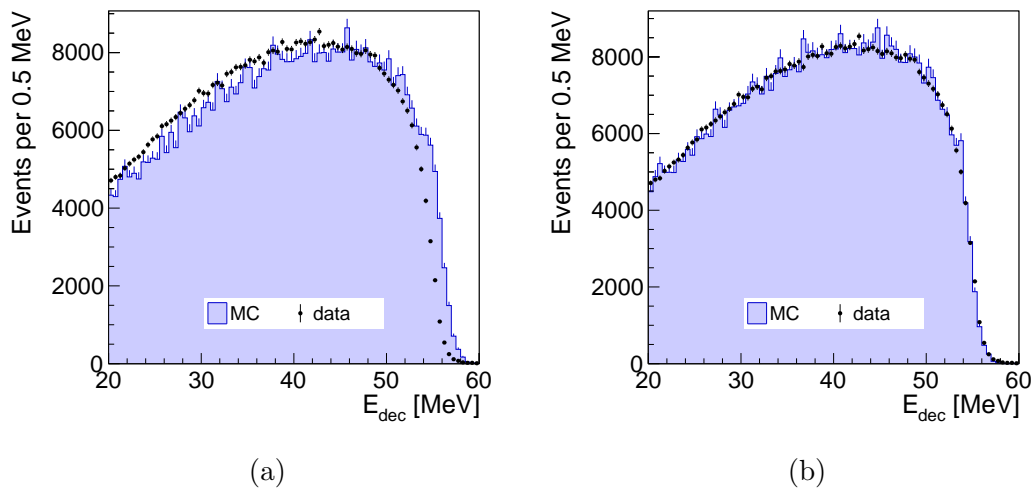


Figure 6.11: MC simulation compared to data. MC exhibit different energy scale (a). MC energies rescaled to better match data (b).

I tested the energy scale of simulated events for different sub-samples of events.

I limited the sub-samples to have the vertex of the decay reconstructed in different layers of the detector. Each layer was a shell defined by two concentric cylinders relative to the center of the detector. This layering is schematically shown in Figure 6.12. Due to a nonuniform response of the detector and greater energy leaks in the outer regions of the scintillator, the observed energy spectrum changes its shape in different volume layers. The scale factor was consistent among the layers with variations within 0.5%.

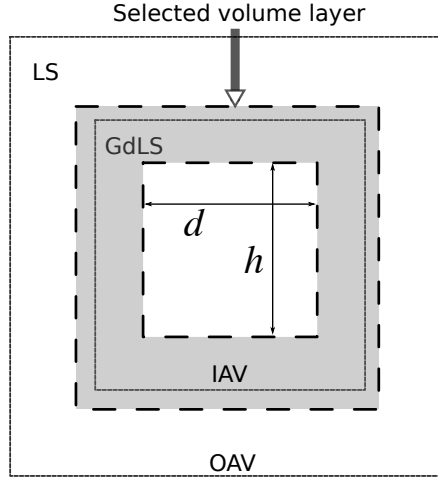


Figure 6.12: Example of a selection of the cylindrical layer centered in AD. The layer is defined by two concentric cylinders of given diameter  $d$  and height  $h$ . The layer in the picture includes the IAV. Only events from the gray area are selected.

After re-scaling of reconstructed energies of the simulated events, I calculated efficiency of the cut on the reconstructed energy as a ratio of the number of simulated events that passed the requirement  $E_{\text{new}}^{\text{MC}} > 20 \text{ MeV}$  to the number of all muons decayed in the detector. The efficiency is  $\epsilon_{E_{\text{dec}}} = (46.2 \pm 0.2)\%$ .

Inconsistencies between MC simulation and real data are pronounced differently at different parts of the detector. I therefore chose to test reliability of the simulation by comparing numbers of real selected events in different detector layers corrected for the efficiency prediction from MC simulation and the total selected volume. Volume layers were selected in the same way as described in the previous paragraph.

I defined the efficiency of the selection of decay-signal reconstructed energy estimated as a ratio of the number of events reconstructed inside the selected volume and with energy greater than 20 MeV to the total number of events reconstructed in the selected volume.

This definition is biased by non-ideal vertex reconstruction. Some events with the muon decay happening in the selected volume may have been reconstructed outside of the volume and some events which occurred outside were wrongly reconstructed inside the volume. I will call these events spill-out and spill-in, respectively. Spill-in and spill-out events determined an effective volume corresponding to the selection. For example, if there were more spill-in events, the effective volume is larger than the one selected, and if there were more spill-out events, the effective volume is smaller. The effect of spill-in and spill-out differs

depending on the selected volume and needs to be corrected for when comparing number of muon decays per unit volume.

I calculated the correction for spill-in and spill-out events from MC simulation where I could compare the true and the reconstructed positions of the muon decay. Efficiencies and spill corrections calculated for 5 different volume layers are listed in the third and fourth column of Table 6.3.

Vol. limit[m]		$\epsilon_{E_{\text{dec}}}$ (MC)	spill corr.	Data	Data/ $\epsilon_{E_{\text{dec}}}/V$	Data/ $\epsilon_{E_{\text{dec}}}^{\text{corr}}/V$
Low	Hi	[%]	[%]		$[\times 10^3]$	$[\times 10^3]$
0.0	1.0	8.86 $\pm$ 0.05	9.84 $\pm$ 0.08	62803	5.64 $\pm$ 0.04	5.55 $\pm$ 0.06
1.0	1.3	8.66 $\pm$ 0.05	9.82 $\pm$ 0.10	78590	6.04 $\pm$ 0.04	5.93 $\pm$ 0.07
1.3	1.6	8.06 $\pm$ 0.05	9.01 $\pm$ 0.07	127341	6.62 $\pm$ 0.04	5.97 $\pm$ 0.06
1.6	1.8	7.30 $\pm$ 0.05	7.31 $\pm$ 0.07	125183	7.87 $\pm$ 0.06	5.75 $\pm$ 0.07
1.8	2.0	4.78 $\pm$ 0.05	6.42 $\pm$ 0.06	98585	7.56 $\pm$ 0.08	4.85 $\pm$ 0.07
	none	4.62 $\pm$ 0.02		494115		5.56 $\pm$ 0.03

Table 6.3: Dependence of efficiency of the cut on reconstructed energy of the muon-decay signal  $\epsilon_{E_{\text{dec}}}$  on position in AD. Efficiencies were determined from MC simulation with events selected from different volume layers within two cylinders with respective radii Low and Hi and of total volume  $V$ . Efficiency is applied to data from the same volume selection. Last column compares data after inclusion of correction for spill effects. Stated errors are statistical uncertainties from the limited MC sample or data.

**Comparison of MC simulation with data:** I applied restriction on reconstructed vertex to be in the volume layers as defined previously to the nominal selection of the real data. I combined data of two ADs in EH1. Counts for each selection are listed in the fifth column of Table 6.3. The second last column contains numbers after correction for energy selection and are normalized to unit volume. These numbers should ideally match since the number of decaying muons in a unit volume is independent of place in the detector. They do not agree with each other because of the spill-in/-out effect, which is different for each volume layer and changes the effective volume in which the decays happened.

The last column in the table presents the final numbers corrected for the effective volume. The values are also plotted in Figure 6.13. The first 4 results agree within about 3.5% variation. The last estimate deviates significantly. The selected layer with limits on radius 1.8 m–2 m is right at the border of the volumes with liquid scintillator and mineral oil. I attribute this difference to the limit on  $E_{\mu}$  in the nominal selection of data. Reconstructed energy of the stopping muon is required to be at least 20 MeV. Deposited energy of 20 MeV in the scintillator corresponds to about 10 cm path length. Therefore, muons which stopped by the edge of the scintillator volume and did not deposit enough energy in it are rejected from the data sample. However, their decays can produce signals large enough to pass the requirement on  $E_{\text{delayed}}$ . Such decays are not removed in the simulations because there is no information about the prompt signal from the muon.

The estimated number of decays selected in the boundary layer deviates from

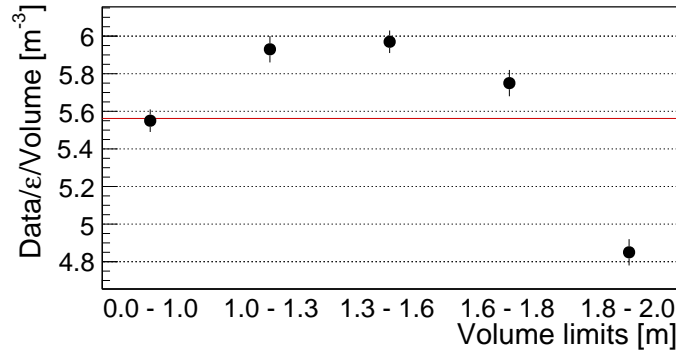


Figure 6.13: Numbers of events from data with nominal selection and with reconstructed position inside 5 layers. The numbers are corrected for the calculated efficiency of the cut on  $E_{\text{dec}}$  and recalculated to unit volume. Red line indicates corrected number of selected events without any requirement on reconstructed position. The volume layers are indicated on the horizontal axis with pairs of limits on radius and half-height of the bounding cylinders.

the inner layers by about 10%. I assume that this difference is solely due to the limit on energy of the muon signal. Number of selected events in this layer constitute 20% of the nominal selection of muon decay events. I therefore estimate that about 2% of the total decays in the detector were able to satisfy the requirement on reconstructed energy of the decay signal,  $E_{\text{dec}} > 20$  MeV, but failed to pass the threshold for energy of the prompt signal,  $E_{\mu} > 20$  MeV.

**Determination from data:** The second method of the energy cut efficiency estimation is based on real data. The idea is to fit data with a model which describes the energy spectrum, and calculate the efficiency from the fit extrapolated below 20 MeV. The model of the spectrum of reconstructed energies is based on calculated distribution of energies of the decay electron or decay positron combined with its annihilation gamma photons. A convolution of true energy distribution with a simple Gaussian model of the detector response is then calculated. Reconstruction non-uniformity and energy losses outside scintillator volume can not be described by this simple model. I restricted the selection of muon decay events to the central region of the detector, where the distortions are expected minimal.

The model of the expected deposited energy is described in details in Chapter 5. The deposited energy consists of kinetic energy of the decay electron or positron, and associated gamma photons in case of  $\mu^+$ . Photons from the annihilation of positron and from radiative muon decay are considered. Energy spectrum of electrons from  $\mu^-$  decay follow calculated distribution of muon decay in orbit. The model combines the two predicted distributions of deposited energy in the ratio of expected decays of  $\mu^+$  and  $\mu^-$ . As already pointed out earlier, charge ratio of not decayed nor captured muons after 10  $\mu\text{s}$  from their stopping is estimated to be 1.9. The model also takes into account that only about 92% of  $\mu^-$  decay.

The energy response of the detector was modeled by linear re-scaling of the

modeled deposited energy to the scale of reconstructed energy. The spectrum is then spread by convolution with Gaussian distribution. The convolution attempts to model the energy resolution of the detector. The variance of the Gaussian distribution is set according to the following formula  $\sigma^2 = \sigma_0^2 + \sigma_1^2 \times E'_{\text{dep}}$ . The first term in the formula,  $\sigma_0$ , stands for electronic noise and its contribution is completely negligible in the considered interval of energies. The second term,  $\sigma_1$  stands for statistical variation of the collected light.

The model was then fitted to the data using maximum binned likelihood method of the ROOT analysis tool. I fixed the expected muon charge ratio  $R_\mu = 1.9$ . I left 3 parameters free: the overall normalization, the energy re-scaling factor, and the statistical term of the detector resolution  $\sigma_1$ . The distribution of reconstructed energies of selected events together with the best-fit model is plotted in Figure 6.14. Data from AD1 and AD2 are combined.

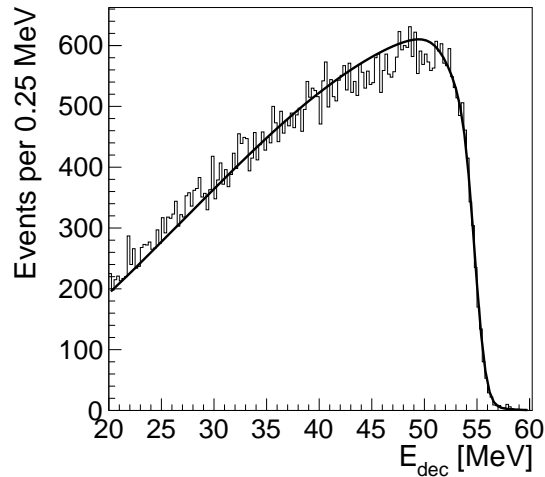


Figure 6.14: Distribution of reconstructed energies of the muon-decay signal  $E_{\text{dec}}$ . Nominal selection is applied with additional limit on reconstructed position to be within cylinder with radius and half-height of 1 m and centered in the AD. Spectrum is combined from AD1 and AD2 from EH1. Data are fitted with my model.

The ratio of area under the model curve in the selection region, from 20 MeV to 60 MeV, to the area in the full range yields efficiency of 91.9%. Statistical uncertainty of this estimate is insignificant. The efficiency did not effectively change when the  $R_\mu$  parameter of the model was modified. A variation of the ratio in the range 1.7 through 2.1 caused changes in the efficiency estimate at the level  $\approx 0.03\%$ .

This number cannot be directly compared to the previously calculated efficiency from MC simulations. The fit to the data does not reflect the effect of spill-in/-out. The efficiency calculated from the best-fit model can be understood as relating the number of decays in the selected volume which were reconstructed in the specific interval of energies, and the total number of decays in the specified volume. Whereas the efficiency based on MC simulation and corrected for the spill-in/-out effect relates the number of events reconstructed in the volume

and energy interval to the total number of events in that volume. Therefore, the difference is in whether the selected events were reconstructed in the volume or actually happened there. For illustration, the definition can be simplified in the following way:

$$\epsilon_{\text{spill-corrected}}^{\text{MC}} = \frac{N_{\text{reconstructed in selected volume, } 20 \text{ MeV} < E_{\text{rec}} < 60 \text{ MeV}}}{N_{\text{decayed in selected volume}}}$$

$$\epsilon_{\text{fit-to-data}} = \frac{N_{\text{decayed in selected volume, } 20 \text{ MeV} < E_{\text{rec}} < 60 \text{ MeV}}}{N_{\text{decayed in selected volume}}}.$$

In order to match the definitions of the efficiencies and to have well defined volume of the selection sample, correction for spill-in and spill-out in the energy region above 20 MeV needs to be applied. This correction needs to be extracted from the simulations. Comparison of events with reconstructed energies above 20 MeV and true decay vertex inside the required volume to those which were reconstructed there yielded correction of  $1.016 \pm 0.008$ .

The data-based efficiency corrected for the spill effects is then  $\epsilon_{\text{data}}^{\text{corr}} = (90.4 \pm 0.7)\%$ . This number can be compared to the efficiency based on MC simulations from Table 6.3 in the row corresponding to the 0–1 m volume selection. The stated efficiency  $\epsilon_{E_{\text{dec}}}$  corrected for the spill effects is  $\epsilon_{\text{MC}}^{\text{corr}} = (90.0 \pm 0.8)\%$ . The uncertainties of both estimates come from the statistical uncertainty of the MC based spill corrections and are necessarily correlated between the two values.

**Determination of uncertainty:** The largest uncertainty in determination of the efficiency of the reconstructed-energy selection comes from the uncertainty of how the MC simulation is capable to reproduce the response of the detector and the reconstructed energy. The disagreement would be pronounced differently at different regions of the detector. The tests performed with event selections in different layers of the detector for MC and real data give consistent results within 3.5% in Table 6.3.

The comparison of the efficiency calculation based purely on MC simulation with efficiency obtained from a fit to data gives difference of 0.4% which I consider as an uncertainty inherent to the methods used and it reflects in part differences in true energy and in part uncertainty in the model of energy response of the detector.

I conservatively combine the two results into the final absolute uncertainty in the energy-selection efficiency  $\epsilon_{E_{\text{dec}}} = 47.8\%$  of  $47.8\% \cdot 0.035 + 0.4\% \doteq 2.1\%$ . I consider this systematic uncertainty to be conservative and I neglect the statistic uncertainty from limited MC sample.

### Selection of muon energy

I have analyzed a special MC simulation data sample which simulated muons in each hall. Muons were generated from energy and angular distribution as obtained from MUSIC simulations[40] already discussed in previous section. They were propagated using Geant4 tool through each hall. Since muons produce large amount of light in detectors, full detector simulation was unfeasible for the purpose. Therefore, Cherenkov and scintillation photons were not simulated, and no information on detector response could be devised.

The simulation provided information about energy deposited by the muons in different parts of detector. I selected only muons which stopped inside the scintillator volume of the AD, that is, in LS or GdLS regions. Figure 6.15 shows spectrum of reconstructed energies of muons of the nominal selection with limit on muon energy lowered from  $E_\mu > 20$  MeV to  $E_\mu > 6$  MeV. The spectrum is compared with distribution of the deposited energies of muons decaying in the detector.

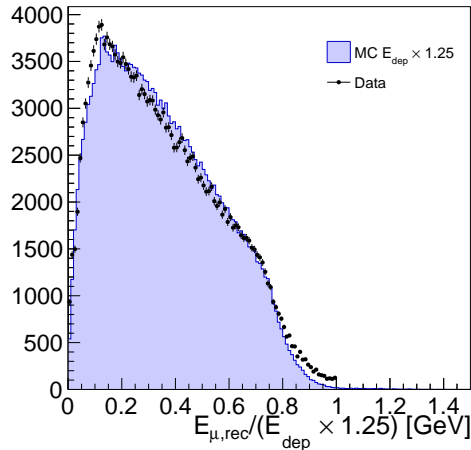


Figure 6.15: Comparison of energies deposited by decaying muon in scintillator of an AD in EH1, from MC simulation (filled area), with reconstructed energies of the muon signal in data from the nominal selection (black markers). The nominal selection of events in data is extended to include energies of the muon signal below 20 MeV. The deposited energies from MC are scaled by factor 1.25 in order to better match the spectrum from data.

Negligible number of muons deposit more than 1 GeV in the scintillator region. The efficiency of the upper bound on energy of the muon signal  $E_\mu$  was assumed to be 100%. Although the difference in the two distributions in Figure 6.15 is mainly due to not ideal reconstruction of energy of large muon signals with muons having long tracks in the detector, the difference in tail between simulation and data pictured in Figure 6.16b suggests that some selected muons deposited their energy apart from ionization through other mechanisms that are not reflected in the simulations. An example of such interactions is photon-nuclear spallation of nuclei in the material.

In the region of low deposited energy, plotted in Figure 6.16a, only about 0.8% of muons deposited less than 20 MeV. Data, however, show increase in number of events. Distribution of time delays  $\Delta T$  of these event have the right characteristic exponential decay, therefore they are related to the decaying muons. I attribute them to muons creating small amount of Cherenkov light in the mineral oil and outer acrylic vessel and decaying in close neighborhood of scintillator, so that the decay electron could create signals that passed the cut on the delayed signal.

I observed this effect also when I compared data from different layers in the detector in Table 6.3. In the discussion related to the table I estimated the effect to be  $\sim 2\%$ . Increasing rate of uncorrelated signals in AD in region below 6 MeV did not allow to lower the threshold of  $E_\mu$  much. Events from the interval 6 MeV

through 20 MeV constitute about 1.2% of total selected events, which is consistent with the previous estimate. I therefore assign efficiency  $\epsilon_{E_\mu} = (98 \pm 2)\%$  to the lower cut of  $E_\mu$  common to all three experimental halls.

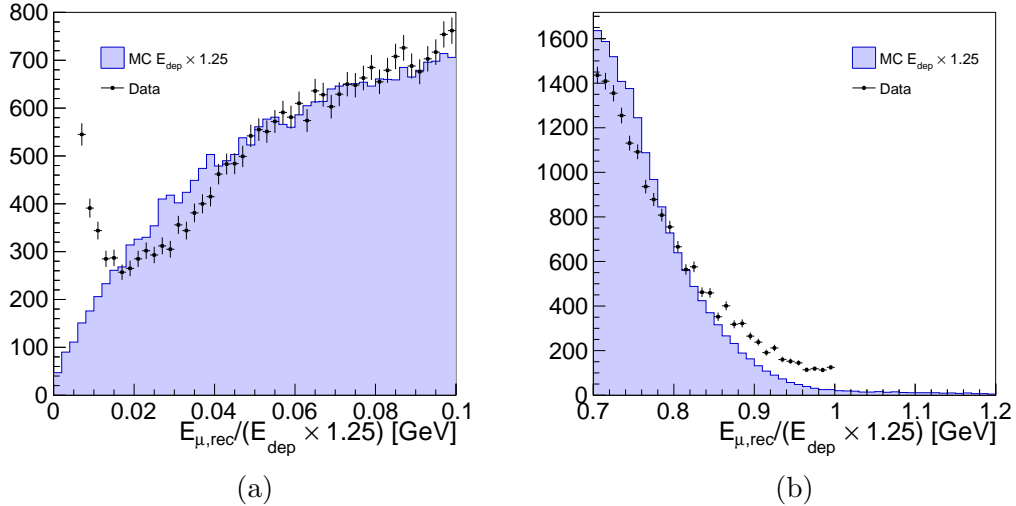


Figure 6.16: Details of comparison of energies deposited by decaying muon in scintillator of an AD in EH1, from MC simulation (filled area), with reconstructed energies of the muon signal in data from the nominal selection (black markers). The nominal selection of events in data is extended to include energies of the muon signal below 20 MeV. The deposited energies from MC are scaled by factor 1.25 in order to better match the spectrum from data.

### Detector live time

The measured numbers of muon decays must be related to the total time of full data taking of the detectors. This number was calculated directly from data. For each recorded file which was used in the analysis, time difference between the last recorded trigger and the first one was added to the total live time. Live times for different periods are summarized in Table 6.4.

### 6.1.3 Rate of Muon Decays from MC Simulation

The sample of simulated muons in experimental halls introduced in the section Selection of muon energy could be used to estimate rate of muon decays in the detector by matching the simulated sample to the muon flux measured in each hall.

Muon fluxes measured by different detectors in each experimental hall were presented in recent publication[45] of the Daya Bay collaboration. Fluxes are measured by individual detector systems, AD, IWS, OWS, and RPC. The average of these measurements is  $1.16 \pm 0.11 \text{ s}^{-1}\text{m}^{-2}$ ,  $0.86 \pm 0.09 \text{ s}^{-1}\text{m}^{-2}$ , and  $0.054 \pm 0.006 \text{ s}^{-1}\text{m}^{-2}$  in EH1, EH2, and EH3, respectively. After recalculating the numbers of simulated muons that decayed in the antineutrino detectors in each hall to match the measured total flux of muons, the estimated decay rates

	EH1		EH2		EH3			
	AD1	AD2	AD1	AD2	AD1	AD2	AD3	AD4
Depth (m.w.e)	250		265		860			
Selected ctounts	246956	247159	177440	171986	5047	4911	5049	5094
	494115		349426		20101			
Live time (days)	927.22		925.69		888.68			
Background (%)	$1.81 \pm 0.04$		$1.38 \pm 0.06$		$0.3 \pm 0.3$			
$\epsilon_{E_{\text{dec}}} (\%)$			$47.8 \pm 2.1$					
$\epsilon_{E_{\mu}} (\%)$			$98 \pm 2$					
$\epsilon_{\Delta T}$			$0.917 \pm 0.023$					
Rate ( $\text{d}^{-1}\text{m}^{-3}$ )	$634 \pm 57$		$451 \pm 41$		$14 \pm 1$			
MC ( $\text{d}^{-1}\text{m}^{-3}$ )	$656 \pm 62$		$479 \pm 50$		$13.3 \pm 1.5$			

Table 6.4: A summary of muon-decay candidate sample. The numbers of selected events in each detector and in each hall, detector live time, estimated background efficiencies of individual selection criteria, and the final calculated rates are listed. Results from MC simulation are also provided for comparison.

are  $656 \text{ d}^{-1}\text{m}^{-3}$ ,  $479 \text{ d}^{-1}\text{m}^{-3}$ , and  $13.3 \text{ d}^{-1}\text{m}^{-3}$  in the three respective experimental halls. These rates agree well with the measured rates presented in Table 6.4.

### 6.1.4 Summary

I selected muon decay events by looking for two signals correlated in time. The first signal was produced by the muon entering and stopping in the detector. The second signal was produced when the muon decayed. Due to distortions in signal up to  $10 \mu\text{s}$  after the usually large 1st signal, I limited the selection to events where the two signals occurred in  $10 \mu\text{s}$  through  $30 \mu\text{s}$  time interval.

I restricted both signals to specific intervals of reconstructed energy. The energies must be in ranges 20 MeV through 1 GeV and 20 MeV through 60 MeV for muon stopping in the detector and the muon decay, respectively. More restrictions which I also applied were described in the Section 6.1 but have minimal impact on efficiency.

I estimated efficiency for the selection of the time-difference between the two correlated signals and of the reconstructed energy of the muon-decay signal. The efficiency of the former restriction was calculated from expected time distribution of muon decay of a mixed sample of  $\mu^+$  and  $\mu^-$ . The parameters of muon decay and muon capture rates were inherited from literature. I estimated the muon charge ratio  $R_{\mu}$  also based on measurements of previous experiments. I tested validity of these parameters on the nominal events selection as well as on a modified sample. Although the nominal values agreed with the observation, the limited sensitivity of the data and strong correlation between the parameters allowed them to vary beyond the assumed uncertainty of the previous measurements. I estimated interval for the calculated efficiency based on its variation with changes  $R_{\mu}$  within the estimated uncertainty.

The selection efficiency of the reconstructed energy of the decay signal was es-

estimated from MC simulation. I tested the simulation results on data for different regions in the detector. I also fitted my model to the distribution of reconstructed energies of the decay signal, and I compared the calculated efficiency for a restricted central region of the detector with the result obtained from simulation.

The final measured rates of decays of stopped muons are summarized in Table 6.4. Rates in each experimental hall are listed together with rates measured for individual ADs. The table also lists the numbers of events of the nominal selection and the estimated efficiencies and backgrounds. The decay rates are also compared with the MC predictions.

## 6.2 Detector Energy Scale at 53 MeV

Spectrum of visible energies of muon decays has very distinct feature at around 53 MeV. This energy is the maximal energy kinematically allowed for the electrons and positrons from muon decay. Sharp edge in the spectrum of electrons from decays of  $\mu^-$  is smeared in the presence of material due to the creation of muonic atoms, but the sharp slope of the spectrum remains. The edge is an opportunity for energy calibration of the detector.

I estimate the scale factor between reconstructed energies in the antineutrino detector and the true deposited energy for electrons and positrons from the muon decays. The energy spectrum of the decays is compared between MC simulations and real data. Both are fitted with a model of distribution of visible energies combined with a simple model of detector response.

I first describe the model of the spectrum of reconstructed energies than I introduce the selection of events in data and then I focus on the results of analysis of MC simulation and data.

### 6.2.1 Model of reconstructed energies of muon decays

The spectrum of visible energies from muon decays was introduced in Chapter 5. Positrons from  $\mu^+$  decays deposit their full kinetic energy and then annihilate, the annihilation gammas are assumed to contribute to the total visible energy. Energies of the decay positrons are generated from the distribution based on calculations with radiative corrections. About 10% of the decays is assumed to be accompanied by a radiated photon with energy higher than 50 keV. Its energy is added to the total sum of visible energy, too. There is only minor difference of this model and the spectrum of electrons calculated in Born approximation, i.e. without the radiative corrections.

$\mu^-$  is modeled to decay from S-orbit of oxygen atom. The spectrum is taken from numerical calculations of decays in orbit which do not, to my best knowledge, exist for carbon. I assumed the spectrum to be a good approximation.

Spectra of the two types of decay are combined in the ratio  $R_\mu$  to match the expected ratio of  $\mu^+$  and  $\mu^-$  in the data sample.

I modeled the energy response of the detector to the visible energy  $E_{\text{true}}$ , i.e. its transformation to reconstructed energy, by scaling it with factor  $A = E_{\text{rec}}/E_{\text{vis}}$ , and then convolving the resulting spectrum with Gaussian function with standard deviation  $\sigma$  representing the detector energy resolution. Denoting the final distribution of reconstructed energies  $F(E_{\text{rec}})$  and the distribution of true visible energies  $f(E_{\text{vis}})$ , the application of energy response is described by the following convolution:

$$F(E_{\text{rec}}) = \int f(E_{\text{vis}}) \frac{1}{\sqrt{2\pi\sigma^2}} \exp\left(-\frac{(E_{\text{rec}} - AE_{\text{vis}})^2}{2\sigma^2}\right) dE_{\text{vis}}. \quad (6.8)$$

This convolution is not valid for energies comparable to the resolution. In practice, the integration is limited to only small region around the energy  $E_{\text{rec}}$ . Real detector response is more complicated due to various effects. The most prominent being energy leakage through radiated gamma photons and spatial extent of deposition of energy. Non-linearity of the scintillator and the electronics, and

non-uniform energy reconstruction also add to these effects. In Figure 6.17, the original spectrum of energies  $E_{\text{vis}}$  is compared to the spectrum after application of the simple detector response function with  $A = 1$  and  $\sigma = 0.8$  MeV. The two spectra disagree only in the narrow region of energies around the edge at 53 MeV.

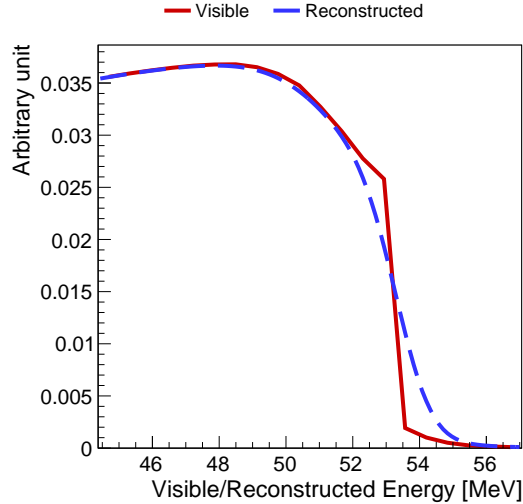


Figure 6.17: Comparison of spectrum of visible energies from muon decay (full red line) to the spectrum after application of the simple detector response function from Equation (6.8) (dashed blue line).

Although this model of the detector response cannot describe well the spectrum in more extended range of energies, it is sufficient in a narrow region around 53 MeV of visible energy, where changes in resolution and energy scale are small. To avoid effects related to the leakage of energy either form bremsstrahlung or annihilation gammas escaping from the scintillator volume, or due to energy loss of the decay electron in the acrylic vessels, this model should be applied to data with events only from the central region.

## 6.2.2 Data Selection

I analyzed the energy scale of ADs in EH1. I used spectrum of reconstructed energies of the muon-decay signal from combined data of both ADs. In addition to the nominal selection described in the previous chapter, I selected only event with the vertex of the decay signal reconstructed in the central region of the detector. The region is defined by a virtual cylinder with diameter and height of 2 m and aligned to the center of the AD.

This additional requirement is needed in order to avoid distortions in the spectrum caused by: 1) partial deposition of energy of the decay electron or positron in the acrylic vessel; 2) escape of one or both annihilation photons from the scintillator region; 3) non-uniform energy reconstruction in the outer regions of the detector.

The spectrum is shown in Figure 6.18.

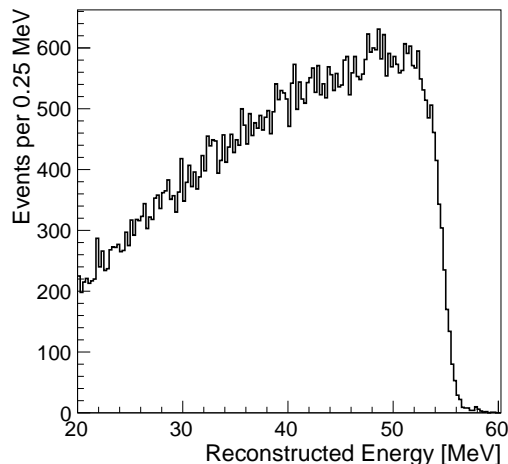


Figure 6.18: Spectrum of reconstructed energies of muon-decay signals. Nominal selection is used with additional requirement on the reconstructed vertex to be contained in a 2 m-by-2 m cylinder in the center of the AD. Data are combined from AD1 and AD2 from EH1.

## 6.2.3 MC Simulations

### Simulation of $\mu^-/\mu^+$ decays

In Section 6.1.2 of the previous chapter, I introduced MC simulation of muon decays in the Daya Bay detectors. Two separate batches negatively and positively charged muons were generated with momentum of 1 keV/ $c$ . Spectrum of decay electrons and positron is simulated by the Gean4 simulation software. The full simulation chain included tracking of individual particles and scintillation and Cherenkov photons, simulation of PMT response, digitization of the signals and finally reconstruction of energy and vertex.

As described in Section 6.1.2, I combined the two samples of  $\mu^-$  and  $\mu^+$  decay simulations in the expected ratio given by the muon-charge ratio  $R_\mu = 1.9$ , equivalent to ratio of muons surviving 10  $\mu$ s after they stopped. I also applied the same limits on the reconstructed vertex of the decay event as in the data selection.

The combined spectrum of reconstructed energies does not match the spectrum of reconstructed energies from data. A simple correction of scale of reconstructed energies in simulation resulted in better match. Figure 6.19 compares energy spectrum from simulation and data before the correction of MC energy and after scaling the energy down by a factor 0.980. I performed the matching by following the same procedure, but the I compared the two histograms only in the region of energies around the edge, 48 MeV through 56 MeV.

I fitted the model described in the beginning of this chapter, and will call it “my model”, to the combined spectrum with 3 free parameters, the normalization of the model  $N$ , energy scale factor which relates the true energy with the reconstructed energy  $A$ , and the energy resolution  $\sigma$ . The parameters of the model of true energies were fixed to their nominal values. The most prominent parameter

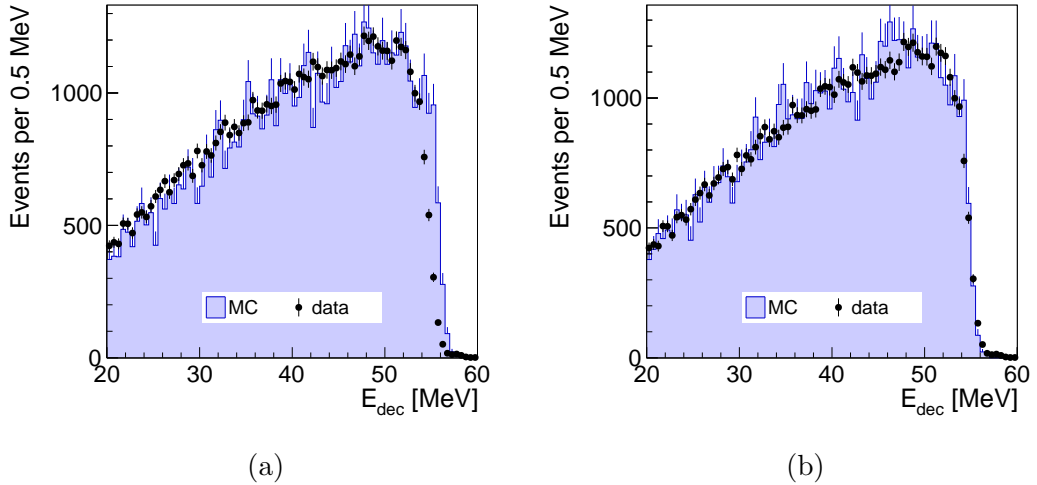


Figure 6.19: Comparison of energy spectrum of muon-decay signals from MC simulation and from data. MC is shown before (a) and after (b) matching the energy scale to data.

is the muon charge ratio which was set to  $R_\mu = 1.9$ .

I limited the fit to range from 48 MeV to 58 MeV. I assumed that the energy resolution  $\sigma$  of the detector and the energy scale factor do not change in the narrow range of energies. This is approximately true for the energy scale factor, but the resolution changes by about 10% in the 10-MeV range. The dependence of these parameters on energy in MC simulations is described in the following section.

The best-fit values of the parameters are  $A = 1.028 \pm 0.001$  and  $\sigma = (0.47 \pm 0.07)$  MeV.

My model of true energies differs from the spectrum of the true energies in the simulations. In the simulations, the spectrum of positrons from the decay of  $\mu^+$  follows the simple distribution in Born approximation described by the formula in (5.1) of Chapter 5. This spectrum does not differ much from the spectrum of visible energies of the model which applies radiative corrections and includes the radiative muon decay, as is shown in Figure 5.7. The spectrum of electrons from decays in orbit of  $\mu^-$ , however, is treated differently in the simulation than in the model. The spectrum in the simulation only reflects relativistic boost of the decay electron due to non-zero kinetic energy of the muon in the orbit. Whereas the model uses a more complex approach described in Section 5.5.

I created a new model, denoted here as G4 model, which uses the true combined spectrum of muon decays in the simulation and applies the detector response function to it, following the prescription in (6.8).

I fitted the G4 model to the spectrum from simulations following the same procedure described previously. The best-fit values of the two parameters  $A$  and  $\sigma$  are  $1.027 \pm 0.001$  and  $(0.56 \pm 0.07)$  MeV, respectively.

The results of the two fits are in relative agreement in the case of the scale  $A$  but disagree in the  $\sigma$  parameter. The possible underestimate of its value by the fit of my model can rise from the fact, that the model of decays in orbit of  $\mu^-$  has slightly broader slope at the edge than the spectrum of the G4 model. Also,

the two parameters are correlated in the fit, and therefore small difference in the models can yield the small shift in parameter  $A$  which is compensated by change of  $\sigma$ .

Both fits are shown in Figure 6.20.

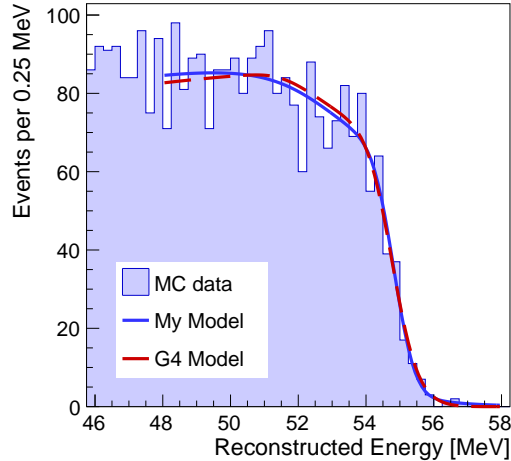


Figure 6.20: Two fits to energy spectrum of muon-decay signal from MC simulation are compared. My model is based on calculations presented in Chapter 5 and G4 model is based on simplified model of electron spectrum used in Geant4 simulations. Simple Gaussian detector response function is applied in both models.

### Simulation of mono-energetic $e^-/e^+$

The dependence of energy scale factor and energy resolution on energy in the simulations can be estimated. For this purpose, I simulated mono-energetic electrons and positrons with selected momenta ranging from 8 MeV/ $c$  up to 55 MeV/ $c$ . The particles were generated uniformly in the full volume of the AD. The full chain of simulation was, again applied, and fully reconstructed events were produced.

I selected only events reconstructed in the same central cylindrical region as was used for the data selection, 2 m in diameter and height, and for the simulation sample of the previous section. I applied the re-scaling factor 0.98 to the reconstructed energies in order to match the scale of real data (also described in the previous section).

Figure 6.21 shows spectra of the re-scaled reconstructed energies of the simulated electrons and positrons with generated momentum 53 MeV/ $c$ . Peaks are visible around mean reconstructed energies,  $(54.19 \pm 0.02)$  MeV and  $(55.03 \pm 0.02)$  MeV respectively for electrons and positrons. Electrons deposit only their kinetic energy whereas positrons produce also annihilation gamma photons and they can deposit 1.022 MeV more energy than electrons. Since the selected sample of events is limited to the central region of the detector, almost all of the annihilation gammas lose their energy in the scintillator.

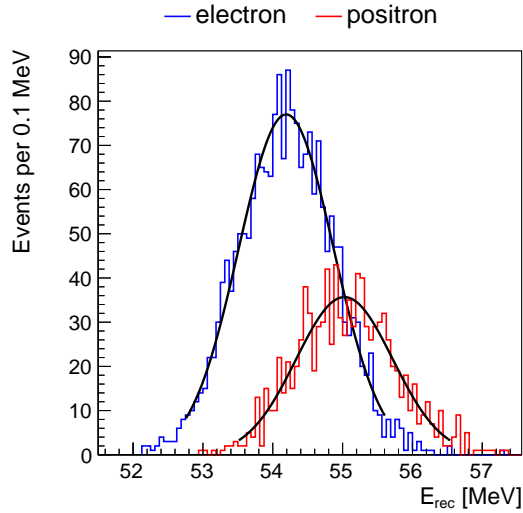
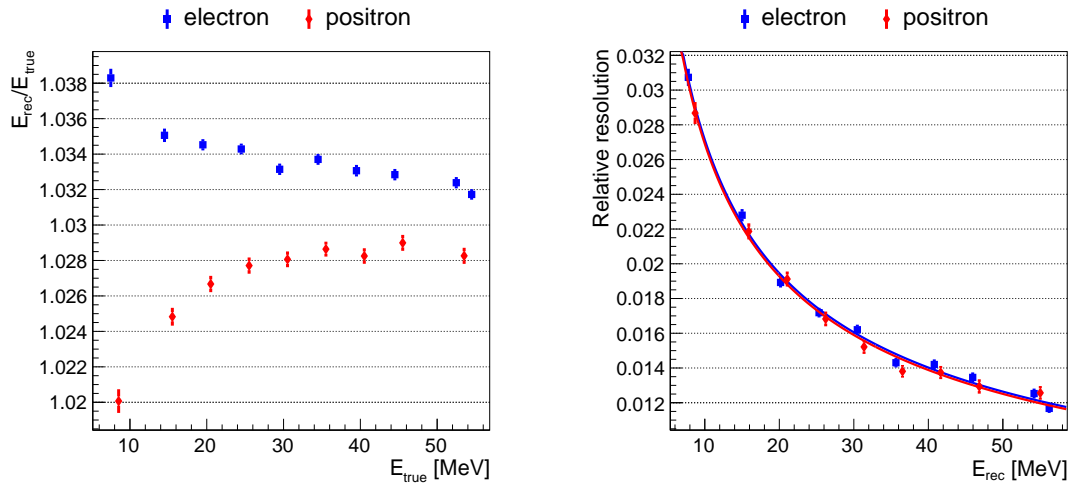


Figure 6.21: Spectrum of reconstructed energies of simulated mono-energetic  $e^-$  (blue) and  $e^+$  (red) with initial momentum of 53 MeV/ $c$ . Events are selected only in if their reconstructed vertex was in the central cylindrical region (2 m in diameter and height). Both peaks are fitted with Gaussian function.



(a)

(b)

Figure 6.22: Nonlinear energy response (a) and relative energy resolution (b) of the Daya Bay antineutrino detector to electron (blue) and positron (red) events, as determined from MC simulations of mono-energetic  $e^-/e^+$ . Plot (a) shows ratio of reconstructed and initial energy of the simulated particles with respect the initial energy. If the response of the detector were linear with energy, points would have lain on a horizontal line. Plot (b) shows ratio of energy resolution to mean reconstructed energy is plotted versus the corresponding mean reconstructed energy. Data points are interleaved with function described in the text.

I fitted the peaks with Gaussian functions and extracted the the mean and standard deviation. Ratio of the mean reconstructed energies and the true de-

posited energy is plotted in Figure 6.22a as a function of the true energy. Non-linear relation between the reconstructed and true energy is visible, as well as the difference between electrons and positrons. The non-linearity is the result of two main effects: particle dependent non-linear light yield of the scintillator and charge-dependent non-linearity in the PMT readout electronics[21], which are also simulated.

The response of the detector differs for the two particles due to additional emission of annihilation gammas in the case of positron. The annihilation gammas produce scintillation light which is quenched separately from the scintillation light from the ionization by the positron.

Approximate scale of reconstructed energy of simulated electron and positron events,  $E_{\text{rec}}/E_{\text{true}}$ , around the true energy 53 MeV is  $1.0320 \pm 0.0004$  and  $1.0285 \pm 0.0004$ , respectively.

Figure 6.22b shows energy resolution relative to the reconstructed energy. It follows approximately  $1/\sqrt{E_{\text{rec}}}$ . The data points are interleaved best fit formulas which both are approximately  $\sqrt{0.086^2/E_{\text{rec}} + 0.004^2}$ , which agrees with energy resolution evaluated in the lower energy range for the oscillation analysis  $\sigma/E_{\text{rec}} \approx 8\%$  at 1 MeV[26].

## 6.2.4 Fit to Data

I took the data sample described in Section 6.2.2. It contains events of muon decays from both ADs in EH1 with the nominal selection applied and with limitation of the reconstructed vertex to the central cylindrical volume.

I fitted the edge in the energy spectrum of the muon decay signals with my model described in Section 6.2.1. I limited the energy range of the fit to 48–58 MeV. As previously discussed, the energy scale  $A$  does not change significantly in this range. MC simulations showed that the energy resolution changed from about 0.6 MeV to 0.7 MeV with negligible effect on the spectrum shape.

I left three parameters free in the fitting procedure, the overall normalization  $N$ , the energy scale  $A$ , and the detector energy resolution  $\sigma$ . The best-fit values of the energy scale and energy resolution are  $A = 1.0282 \pm 0.0006$  and  $\sigma = (0.74 \pm 0.03)$  MeV. With changes of the lower limit of range of the fit, the best fit parameters do not change significantly. The fit to the data is shown in Figure 6.23.

The most uncertain parameter in my model is the ratio of  $\mu^+$  and  $\mu^-$   $R_\mu$ . In Section 6.1.2, I conservatively estimated that it may vary from about 1.8 to 2.0 for the selected data. The best-fit values change only little when changes to  $R_\mu$ .

The two fit parameters  $A$  and  $\sigma$  are correlated. This correlation is included in the stated errors of the fit. I tested how the best-fit value of  $A$  changed when fixing the  $\sigma$  parameter to the values deviated by 2 standard deviations from the nominal fit  $\sigma = (0.74 \pm 0.03)$  MeV. Variations of best-fit parameter  $A$  with respect to changes in  $R_\mu$  and  $\sigma$  are plotted in Figure 6.24.

## 6.2.5 Summary

Spectrum of reconstructed energies of simulated muon decays matches well the measured spectrum after correcting to the simulated energies by factor 0.980.

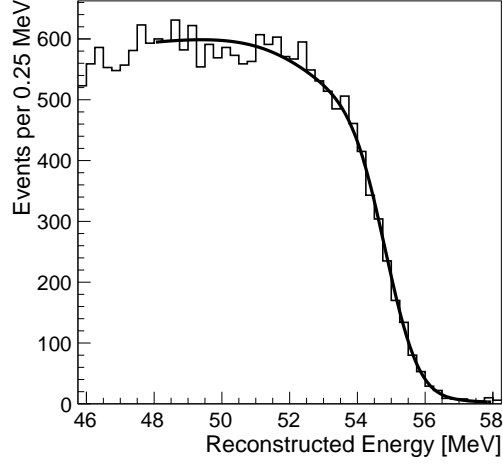


Figure 6.23: Spectrum of reconstructed energies of the selected decay events in EH1 (histogram) with the fit of my model.

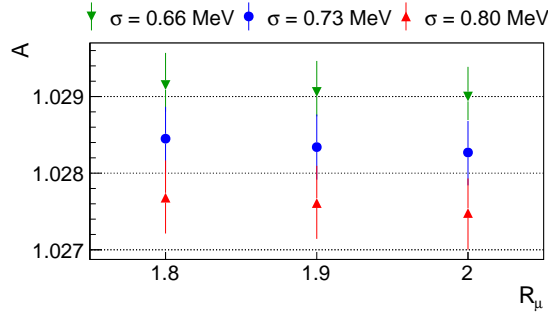


Figure 6.24: Best-fit values of energy scale  $A$  with varying muon charge ratio  $R_\mu$  and the assumed detector resolution  $\sigma$ .

Fits of my model and G4 model to the edge in the spectrum yielded relatively consistent best-fit values for energy scale at 53 MeV  $A = 1.028$  and  $A = 1.027$ , respectively.

The results of simulations of mono-energetic electrons and positrons show that the detector has different energy scale for the two kinds. When they deposit energy around 53 MeV their reconstructed energy is scaled by factors 1.032 and 1.028, respectively.

Best-fit parameters of the fit of my model to the edge in data from the two ADs in EH1 are  $A = 1.0282 \pm 0.006$  and  $\sigma = (0.73 \pm 0.03)$  MeV. Simulations suggest that the estimate of the energy resolution  $\sigma$  may be biased, but the estimate of energy scale  $A$  is unbiased within the statistical uncertainty.

The response of the detector to positrons from the anti-neutrino interactions is modeled for the neutrino oscillation analysis. Figure 6.25 compares the model presented in our recent publication [21], with the result of this work. The model is determined using calibration data from  $\gamma$ -ray sources and electrons from decays of  $^{12}\text{B}$  produced in interactions of cosmic rays inside the detector. I included the two points for electron and positron, and inflated the uncertainty to 0.002 to

conservatively allow for undetermined systematic biases.

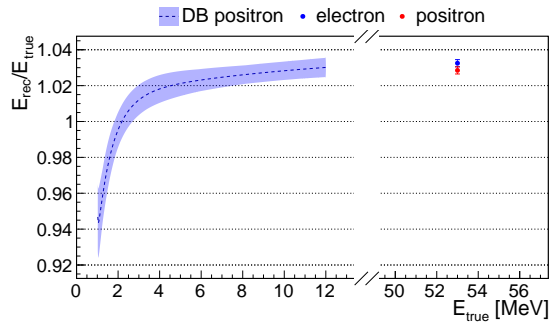


Figure 6.25: Comparison of a model of ratio of reconstructed energy over true energy,  $E_{\text{rec}}/E_{\text{true}}$ , for energies below 12 MeV, with the measurement at 53 MeV. The model at lower energies is applied to positron interactions contained in the target region of the antineutrino detector.

This measurement can be used to better constrain the energy model of the oscillation analysis and to further optimize the MC simulations. It also provides another calibration point for events with energies beyond the standard calibration sources. The Daya Bay experiment is a part of the Supernova Early Warning System[90] and is capable to detect interactions of antineutrinos from near supernova events[91]. The expected visible energies from the positrons of the antineutrino interactions peak around 20 MeV and have broad distribution. Calibration point at 53 MeV can extend the validity of the nominal energy model currently used.

# Conclusion

The Daya Bay experiment discovered the neutrino oscillation mode in disappearance of electron antineutrinos from nuclear reactors at short baselines. It measures parameters  $\theta_{13}$  and  $\Delta m_{ee}^2$  of the corresponding neutrino mixing at high precision. The experiment continues reducing uncertainties not only related to statistics but also the systematic uncertainties related to background and energy response of the detector.

Most of the background is related to cosmic ray muons. Daya Bay detectors are placed underground and are shielded against most of the cosmic ray radiation. Active muon system is used to further decrease the amount of background by vetoing signals correlated with detected muons. Two types of muon detectors are employed, water Cherenkov and RPC based.

The first part of this thesis, related to my contributions to the experiment, reports on tests and quality control of bare RPC chambers before they were used in building of RPC modules. RPCs were first trained and then tested with cosmic ray muons. In total, around 1600 bare chambers were tested and 185 RPCs did not pass quality criteria. The average efficiency of the accepted chambers is 96.05% at 8 kV, with signal threshold at 50 mV, and with filling gas mixture argon:Freon:isobutane in relative amounts of 53:43:4. The average efficiency of assembled RPC modules from performance measurements is 97.9%, which agrees with expectations based on the average of bare chambers.

The RPC system has been operational since the beginning of the experiment and it has been used to measure muon fluxes and in validations of measurements of background signals. Data from RPCs are employed in algorithms for muon track reconstruction.

The second part of the thesis describe the analysis of decays of cosmic ray muons in antineutrino detectors of the Daya Bay experiment. Events are identified as two consecutive signals, the first one from the muon entering the detector, the second one from its delayed decay. Due to effects related to PMT signals shortly after large amount of light in the detector, the selection was limited to events for which the decay signal occurred at least 10  $\mu\text{s}$  after the muon signal. This large dead time, which is about 5 times longer than the mean lifetime of the muon, trimmed the sample to the level of 1% of all decays. I estimated total decay rates of cosmic muons in the detectors to be  $(634 \pm 57) \text{ d}^{-1}\text{m}^{-3}$ ,  $(451 \pm 41) \text{ d}^{-1}\text{m}^{-3}$ , and  $(14 \pm 1) \text{ d}^{-1}\text{m}^{-3}$  in the first, the second, and the third experimental hall, respectively. These rates are in agreement with expectations from MC simulations based on total muon fluxes measured in each hall. Large part of the uncertainty of the rate is related to rate of nuclear captures of  $\mu^-$ .

I also determined a position of an edge in the spectrum of reconstructed energies in muon decays. The position is related to the energy scale of the detector response at around 53 MeV, i.e., the relation between the reconstructed energy and the actual energy deposited in the detector by the decay electrons and positrons together with associated gamma photons. The scale factor from fit to data is  $1.0282 \pm 0.0006$  which is consistent with MC simulations that predict different scales for positrons and electrons,  $1.0280 \pm 0.0004$  and  $1.0325 \pm 0.0004$ , respectively.

Negatively charged muons produce relatively long lived isotope  $^{12}\text{B}$  when they stop and are captured by  $^{12}\text{C}$  nucleus in the detector. The isotope is also produced in muon induced showers in the detector and it contributes to the background. The measurement of muon decays can be used to calculate rate of its production in the muon captures and validate measurement of its total production.

The measured energy scale of the detector response at 53 MeV provides another calibration point which can be useful in validation of models describing the energy response of the detector in the range of lower energies. Moreover, Daya Bay is also sensitive to the neutrinos from supernovae, for which the signal energy is expected to have a wide distribution peaking around 20 MeV and a calibration point at 53 MeV becomes useful.

# A. Supplement to Model of Muon Decay

## A.1 Radiative Corrections to Muon Decay Process

The differential decay width of the free muon with respect to the electron or positron energy is defined by formula (5.3) in section 5.2. The explicit form of the radiative correction  $f^{(1)}$  is presented here. Arbuzov calculated radiative correction to muon decay without neglecting the the mass of the electron[63]. However, I was unable to implement the analytic formula presented in the paper so that it would reproduce the numerical values also listed there. I suspect there is a mistake in the prescription given in the paper.

Instead, I chose a simpler formula (2.4) in paper by Kinoshita and Sirlin [67], where the mass of electron was neglected. The correction function there is labeled  $f(x)$ , but I will stay with current notation as  $f^{(1)}(x)$ :

$$f^{(1)}(x) = (6 - 4x) R(x) + (6 - 6x) \ln x + \frac{1-x}{3x^2} \times [(5 + 17x - 34x^2)(w + \ln x) - 22x + 34x^2] \quad (\text{A.1})$$

where

$$R(x) = 2\text{Li}_2(x) - \frac{1}{3}\pi^2 - 2 + \omega \left[ \frac{3}{2} + 2 \ln \left( \frac{1-x}{x} \right) \right] - \ln x (2 \ln x - 1) + \left( 3 \ln x - 1 - \frac{1}{x} \right) \ln(1-x) \quad (\text{A.2})$$

$\text{Li}_2(y)$  is a polylogarithm function which is defined in either integral representation

$$\text{Li}_2(y) = - \int_0^y dx \frac{\ln(1-x)}{x} \quad (\text{A.3})$$

or its equivalent series representation

$$\text{Li}_2(y) = \sum_{k=1}^{\infty} \frac{y^k}{k^2}. \quad (\text{A.4})$$

As a conclusion remark, I note that the final formula (5.3) is a combination of 1st order Fermi theory that includes electron mass, with 1st order radiative correction where the electron mass was neglected. Justification for the use of the correction with the electron mass neglected is demonstrated in Figure A.1. The correction in (A.1) is plotted against the numeric values of the correction by Arbuzov listed in Table 1 in [63]. Although the data did not match the analytic formula in that paper, they match sufficiently well the prescription (A.1).

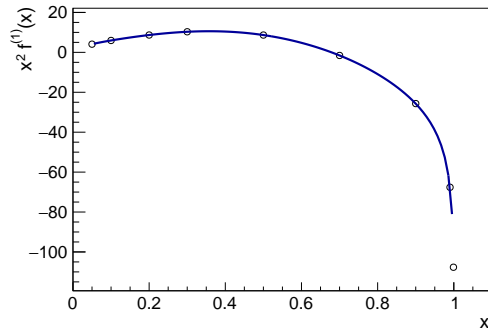


Figure A.1: The radiative-corrections function  $x^2 f^{(1)}$  (line) from [67] and from Equation A.1 is compared to numerical values from [63]. The former calculation neglects mass of the electron which is accounted for in the latter one.

## A.2 Branching Ratio of Radiative Muon Decay

Differential branching ratio of radiative muon decays with respect to energies of the decay electron or positron and the radiated photon are introduced in Equation (5.6) of Section 5.3:

$$\begin{aligned}
 \frac{d^2 B}{dx dy} &= \frac{\alpha}{8\pi} \beta \frac{1}{y} \int_{-1}^{\cos \theta_{\min}} F(x, y, d) d \cos \theta \\
 &= \frac{\alpha}{8\pi} \beta \frac{1}{y} \int_{-1}^{\cos \theta_{\min}} F^{(0)}(x, y, d) + r F^{(1)}(x, y, d) + r^2 F^{(2)}(x, y, d) d \cos \theta \\
 &= \frac{\alpha}{8\pi} \beta \frac{1}{y} [F^{(0)}(x, y) + r F^{(1)}(x, y) + r^2 F^{(2)}(x, y)].
 \end{aligned}
 \tag{A.5}$$

The branching ratio is used to calculate the spectrum of visible energy in the decays that include radiation of photons. The formula is derived from prescription of Kuno and Okada[70], where the authors presented the differential branching ratio of radiative muon decays of the polarized muon with the decay electron/positron and photon emitted at energy intervals  $dx$  and  $dy$ , and in solid angles  $d\Omega_e$  and  $d\Omega_\gamma$ . I considered only decays of unpolarized muon and integrated the differential branching ratio over the full solid angles of the electron/positron and the photon. This yielded Equation (A.5) where the only nontrivial operation left is the integral over the angle  $\theta$  between the emitted electron/positron and photon.

Following the same approach as in [70] I expanded the differential branching ratio in powers of  $r = (m_e/m_\mu)^2$ . I derive here the explicit form of  $F^{(i)}(x, y)$ .

In [70],  $F^{(i)}(x, y, d)$  are split into terms proportional to the powers of  $d$ , therefore I merely calculated the integrals of the powers of  $d$  within kinematically allowed range.

Conservation of energy and momentum requires that the angle  $\theta$  is larger than  $\theta_{\min}$ :

$$1 - \beta \cos \theta_{\min} = \frac{2(x + y - 1 - r)}{xy}
 \tag{A.6}$$

for  $2(x + y - 1 - r)/(xy) > 1 - \beta$ . Therefore, the minimum for  $d$  is

$$\begin{aligned} d_{\min} &= 2(x + y - 1 - r)/(xy), \text{ for } 2(x + y - 1 - r)/(xy) > 1 - \beta \\ d_{\min} &= 1 - \beta, \text{ otherwise.} \end{aligned} \quad (\text{A.7})$$

Integrals of  $F^{(i)}(x, y, d)$  over the angle between the photon the charged particle ranging from  $\theta = \theta_{\min}$  through  $\theta = \pi$  are

$$\begin{aligned} F^{(0)}(x, y) &= \frac{8}{\beta} \ln \frac{1 + \beta}{d_{\min}} \{y^2(3 - 2y) + 6xy(1 - y) + 2x^2(3 - 4y) - 4x^3\} \\ &\quad + \frac{8}{\beta} (1 + \beta - d_{\min}) \{-xy(3 - y - y^2) - x^2(3 - y - 4y^2) \\ &\quad \quad \quad + 2x^3(1 + 2y)\} \\ &\quad + \frac{1}{\beta} [(1 + \beta)^2 - d_{\min}^2] \{x^2y(6 - 5y - 2y^2) - 2x^3y(4 + 3y)\} \\ &\quad + \frac{2}{3\beta} [(1 + \beta)^3 - d_{\min}^3] x^3y^2(2 + y) \end{aligned} \quad (\text{A.8})$$

$$\begin{aligned} F^{(1)}(x, y) &= \frac{32}{\beta} \left( \frac{1}{d_{\min}} - \frac{1}{1 + \beta} \right) \left\{ -\frac{y}{x}(3 - 2y) - (3 - 4y) + 2x \right\} \\ &\quad + \frac{8}{\beta} \ln \frac{1 + \beta}{d_{\min}} \{y(6 - 5y) - 2x(4 + y) + 6x^2\} \\ &\quad + \frac{8}{\beta} (1 + \beta - d_{\min}) \{x(4 - 3y + y^2) - 3x^2(1 + y)\} \\ &\quad + \frac{3}{\beta} [(1 + \beta)^2 - d_{\min}^2] x^2y(2 + y) \end{aligned} \quad (\text{A.9})$$

$$F^{(2)}(x, y) = \frac{32}{\beta} \left( \frac{1}{d_{\min}} - \frac{1}{1 + \beta} \right) \left\{ \frac{(4 - 3y)}{x} - 3 \right\} + \frac{48}{\beta} y \ln \frac{1 + \beta}{d_{\min}}. \quad (\text{A.10})$$



# Bibliography

- [1] F. Reines and C. L. Cowan. Detection of the free neutrino. *Phys. Rev.*, 92:830–831, 1953.
- [2] C. L. Cowan, F. Reines, F. B. Harrison, H. W. Kruse, and A. D. McGuire. Detection of the free neutrino: A Confirmation. *Science*, 124:103–104, 1956.
- [3] R. Davis. Solar neutrinos. II: Experimental. *Phys. Rev. Lett.*, 12:303–305, 1964.
- [4] Q. R. Ahmad et al. Direct evidence for neutrino flavor transformation from neutral current interactions in the Sudbury Neutrino Observatory. *Phys. Rev. Lett.*, 89:011301, 2002.
- [5] Y. Fukuda et al. Evidence for oscillation of atmospheric neutrinos. *Phys. Rev. Lett.*, 81:1562–1567, 1998.
- [6] L. Wolfenstein. Neutrino Oscillations in Matter. *Phys. Rev.*, D17:2369–2374, 1978.
- [7] S. P. Mikheev and A. Yu. Smirnov. Resonance Amplification of Oscillations in Matter and Spectroscopy of Solar Neutrinos. *Sov. J. Nucl. Phys.*, 42:913–917, 1985. [Yad. Fiz.42,1441(1985)].
- [8] S. P. Mikheev and A. Yu. Smirnov. Resonant amplification of neutrino oscillations in matter and solar neutrino spectroscopy. *Nuovo Cim.*, C9:17–26, 1986.
- [9] T. Araki et al. Measurement of neutrino oscillation with KamLAND: Evidence of spectral distortion. *Phys. Rev. Lett.*, 94:081801, 2005.
- [10] M. H. Ahn et al. Indications of neutrino oscillation in a 250 km long baseline experiment. *Phys. Rev. Lett.*, 90:041801, 2003.
- [11] B. Pontecorvo. Neutrino Experiments and the Problem of Conservation of Leptonic Charge. *Sov. Phys. JETP*, 26:984–988, 1968. [Zh. Eksp. Teor. Fiz.53,1717(1967)].
- [12] Z. Maki, M. Nakagawa, and S Sakata. Remarks on the unified model of elementary particles. *Prog. Theor. Phys.*, 28:870–880, 1962.
- [13] C. Giunti and C.W. Kim. *Fundamentals of Neutrino Physics and Astrophysics*. Oxford University Press (OUP), 2007.
- [14] J. N. Bahcall, William A. Fowler, I. Iben, Jr., and R. L. Sears. Solar neutrino flux. *Astrophys. J.*, 137:344–346, 1963.
- [15] K. Eguchi et al. First results from KamLAND: Evidence for reactor anti-neutrino disappearance. *Phys. Rev. Lett.*, 90:021802, 2003.
- [16] A. Gando et al. Reactor On-Off Antineutrino Measurement with KamLAND. *Phys. Rev.*, D88(3):033001, 2013.

- [17] K. S. Hirata et al. Experimental Study of the Atmospheric Neutrino Flux. *Phys. Lett.*, B205:416, 1988. [447(1988)].
- [18] K. Abe et al. Measurements of neutrino oscillation in appearance and disappearance channels by the T2K experiment with  $6.6 \times 10^{20}$  protons on target. *Phys. Rev.*, D91(7):072010, 2015.
- [19] P. Adamson et al. Combined analysis of  $\nu_\mu$  disappearance and  $\nu_\mu \rightarrow \nu_e$  appearance in MINOS using accelerator and atmospheric neutrinos. *Phys. Rev. Lett.*, 112:191801, 2014.
- [20] K. A. Olive et al. Review of Particle Physics. *Chin. Phys.*, C38:090001, 2014. (and 2015 edition available on-line at [pdg.lbl.gov](http://pdg.lbl.gov)).
- [21] F. P. An et al. New Measurement of Antineutrino Oscillation with the Full Detector Configuration at Daya Bay. *Phys. Rev. Lett.*, 115(11):111802, 2015.
- [22] F. P. An et al. A side-by-side comparison of Daya Bay antineutrino detectors. *Nucl. Instrum. Meth.*, A685:78–97, 2012.
- [23] J. K. Ahn et al. Observation of Reactor Electron Antineutrino Disappearance in the RENO Experiment. *Phys. Rev. Lett.*, 108:191802, 2012.
- [24] C. Bemporad, G. Gratta, and P. Vogel. Reactor based neutrino oscillation experiments. *Rev. Mod. Phys.*, 74:297, 2002.
- [25] H. Minakata, H. Nunokawa, Stephen J. Parke, and R. Zukanovich Funchal. Determining neutrino mass hierarchy by precision measurements in electron and muon neutrino disappearance experiments. *Phys. Rev.*, D74:053008, 2006.
- [26] F. P. An et al. Spectral measurement of electron antineutrino oscillation amplitude and frequency at Daya Bay. *Phys. Rev. Lett.*, 112:061801, 2014.
- [27] F. P. An et al. Independent measurement of the neutrino mixing angle  $\theta_{13}$  via neutron capture on hydrogen at Daya Bay. *Phys. Rev.*, D90(7):071101, 2014.
- [28] F. P. An et al. New measurement of  $\theta_{13}$  via neutron capture on hydrogen at Daya Bay. *Phys. Rev.*, D93(7):072011, 2016.
- [29] F. P. An et al. Measurement of the Reactor Antineutrino Flux and Spectrum at Daya Bay. *Phys. Rev. Lett.*, 116(6):061801, 2016.
- [30] F. P. An et al. Search for a Light Sterile Neutrino at Daya Bay. *Phys. Rev. Lett.*, 113:141802, 2014.
- [31] H. Wei. Highlight on Supernova Early Warning at Daya Bay. *Phys. Procedia*, 61:802–806, 2015.
- [32] T. Goodman, M. Lasserre. Double chooz: A search for the neutrino mixing angle theta-13, 2006. [arXiv:hep-ex/0606025](https://arxiv.org/abs/hep-ex/0606025).

- [33] M. Apollonio et al. Initial results from the CHOOZ long baseline reactor neutrino oscillation experiment. *Phys. Lett.*, B420:397–404, 1998.
- [34] Y. Abe et al. Indication for the disappearance of reactor electron antineutrinos in the Double Chooz experiment. *Phys. Rev. Lett.*, 108:131801, 2012.
- [35] Y. Abe et al. Improved measurements of the neutrino mixing angle  $\theta_{13}$  with the Double Chooz detector. *JHEP*, 10:086, 2014. [Erratum: JHEP02,074(2015)].
- [36] I. Masaki. New results of double chooz. In *51st Rencontres de Moriond, La Thuile, ELECTROWEAK INTERACTIONS AND UNIFIED THEORIES*, 2016.
- [37] J. K. Ahn et al. RENO: An Experiment for Neutrino Oscillation Parameter  $\theta_{13}$  Using Reactor Neutrinos at Yonggwang, 2010. [arXiv:1003.1391](https://arxiv.org/abs/1003.1391) [hep-ex].
- [38] J. H. Choi et al. Observation of Energy and Baseline Dependent Reactor Antineutrino Disappearance in the RENO Experiment. *Phys. Rev. Lett.*, 116(21):211801, 2016.
- [39] T. K. Gaisser. *Cosmic rays and particle physics*. Cambridge University Press, 1990.
- [40] M. Guan, M.-Ch. Chu, J. Cao, K.-B. Luk, and Ch. Yang. A parametrization of the cosmic-ray muon flux at sea-level, 2015. [arXiv:1509.06176](https://arxiv.org/abs/1509.06176) [hep-ex].
- [41] M. F. Crouch, P. B. Landecker, J. F. Lathrop, F. Reines, W. G. Sandie, H. W. Sobel, H. Coxell, and J. P. F. Sellschop. Cosmic Ray Muon Fluxes Deep Underground: Intensity Versus Depth, and the Neutrino Induced Component. *Phys. Rev.*, D18:2239–2252, 1978.
- [42] W. Beriguete et al. Production of a gadolinium-loaded liquid scintillator for the Daya Bay reactor neutrino experiment. *Nucl. Instrum. Meth.*, A763:82–88, 2014.
- [43] HAMAMATSU. [http://www.hamamatsu.com/resources/pdf/etd/LARGE\\_AREA\\_PMT\\_TPMH1286E.pdf](http://www.hamamatsu.com/resources/pdf/etd/LARGE_AREA_PMT_TPMH1286E.pdf), 2016.
- [44] J. Liu et al. Automated calibration system for a high-precision measurement of neutrino mixing angle  $\theta_{13}$  with the Daya Bay antineutrino detectors. *Nucl. Instrum. Meth.*, A750:19–37, 2014.
- [45] F. P. An et al. The muon system of the Daya Bay Reactor antineutrino experiment. *Nucl. Instrum. Meth.*, A773:8–20, 2015.
- [46] F. P. An et al. The Detector System of The Daya Bay Reactor Neutrino Experiment. *Nucl. Instrum. Meth.*, A811:133–161, 2016.
- [47] F. P. An et al. Improved Measurement of Electron Antineutrino Disappearance at Daya Bay. *Chin. Phys.*, C37:011001, 2013.

- [48] R. Santonico and R. Cardarelli. Development of Resistive Plate Counters. *Nucl. Instrum. Meth.*, 187:377–380, 1981.
- [49] M. Ablikim et al. Design and Construction of the BESIII Detector. *Nucl. Instrum. Meth.*, A614:345–399, 2010.
- [50] M. Gagliardi. Commissioning and first performance of the resistive plate chambers for the ALICE muon arm. *Nucl. Instrum. Meth.*, A661:S45–S49, 2012.
- [51] A. Polini. Design and performance of the detector control system of the ATLAS resistive-plate-chamber muon spectrometer. *Nucl. Instrum. Meth.*, A661:S15–S18, 2012.
- [52] J. Puerta Pelayo. CMS muon system performance. *Nucl. Instrum. Meth.*, A617:52–56, 2010.
- [53] A. Bergnoli et al. The quality control tests for the RPCs of the OPERA experiment. *Nucl. Instrum. Meth.*, A533:203–207, 2004.
- [54] H. R. Band. Aging and performance of BaBar RPCs. In *Proceedings, 2007 IEEE Nuclear Science Symposium and Medical Imaging Conference (NSS/MIC 2007)*, volume 3, pages 1830–1835, 2007.
- [55] J. Vávra. Summary of session 6: Aging effects in RPC detectors. *Nucl. Instrum. Meth.*, A515:354–357, 2003.
- [56] R. Cardarelli, R. Santonico, and V. Makeev. Avalanche and streamer mode operation of resistive plate chambers. *Nucl. Instrum. Meth.*, A382:470–474, 1996.
- [57] A. Calcaterra et al. Analysis and interpretation of the performance degradation of glass Resistive Plate Chambers operated in streamer mode. *JINST*, 2:P10003, 2007.
- [58] L.-H. Ma et al. Study of RPC gas composition using Daya Bay RPCs. *Chin. Phys.*, C34:1116–1121, 2010.
- [59] Inc. MKS Instruments. <https://www.mksinst.com>.
- [60] T. Dohnal. Methods of determination of neutrino mass hierarchy. Diploma thesis, Charles University in Prague, 2016. (Not publicly available yet, July 23, 2016).
- [61] L. Michel. Energy spectrum of secondary electrons from  $\mu$ -meson decay. *Nature*, 163(4155):959–960, jun 1949.
- [62] L. Michel. Interaction between four half spin particles and the decay of the  $\mu$  meson. *Proc. Phys. Soc.*, A63:514–531, 1950. [,45(1949)].
- [63] A. B. Arbuzov. First order radiative corrections to polarized muon decay spectrum. *Phys. Lett.*, B524:99–106, 2002. [Erratum: *Phys. Lett.*B535,378(2002)].

- [64] R. E. Behrends, R. J. Finkelstein, and A. Sirlin. Radiative corrections to decay processes. *Phys. Rev.*, 101:866–873, 1956.
- [65] T. Kinoshita and A. Sirlin. Muon Decay with Parity Nonconserving Interactions and Radiative Corrections in the Two-Component Theory. *Phys. Rev.*, 107:593–599, 1957.
- [66] S. M. Berman. Radiative corrections to muon and neutron decay. *Phys. Rev.*, 112:267–270, 1958.
- [67] T. Kinoshita and A. Sirlin. Radiative corrections to Fermi interactions. *Phys. Rev.*, 113:1652–1660, 1959.
- [68] S.G Eckstein and R.H Pratt. Radiative muon decay. *Annals of Physics*, 8(2):297–309, oct 1959.
- [69] C. Fronsdal and H. Uberall. mu-Meson Decay with Inner Bremsstrahlung. *Phys. Rev.*, 113:654–657, 1959.
- [70] Y. Kuno and Y. Okada. Muon decay and physics beyond the standard model. *Rev. Mod. Phys.*, 73:151–202, 2001.
- [71] C. E. Porter and H. Primakofe. The Effect of Bohr Orbit Binding on Negative mu-Meson beta-Decay. *Phys. Rev.*, 83:849–850, 1951.
- [72] T. Muto, M. Tanifuji, K. Inoue, and T. Inoue. Interaction of  $\mu^-$  meson with matter, II: Spontaneous decay of negative  $\mu^-$  meson. *Progress of Theoretical Physics*, 8(1):13–27, jul 1952.
- [73] L. Tenaglia. Decay rate and spectrum of electrons from  $\mu^-$ -mesons of theK-shell. *Il Nuovo Cimento*, 13(2):284–291, jul 1959.
- [74] R. W. Huff. Decay rate of bound muons. *Annals of Physics*, 16(2):288 – 317, 1961.
- [75] P. Haenggi, R. D. Viollier, U. Raff, and K. Alder. Muon decay in orbit. *Phys. Lett.*, B51:119–122, 1974.
- [76] R. Watanabe, M. Fukui, H. Ohtsubo, and M. Morita. Angular Distribution of Electrons in Bound Muon Decay. *Prog. Theor. Phys.*, 78:114–122, 1987.
- [77] R. Watanabe, K. Muto, T. Oda, T. Niwa, H. Ohtsubo, R. Morita, and M. Morita. Asymmetry and energy spectrum of electrons in bound-muon decay. *Atomic Data and Nuclear Data Tables*, 54(1):165–178, may 1993.
- [78] D. F. Measday. The nuclear physics of muon capture. *Phys. Rept.*, 354:243–409, 2001.
- [79] A. Grossheim et al. Decay of negative muons bound in Al-27. *Phys. Rev.*, D80:052012, 2009.
- [80] A. Czarnecki, M. Dowling, X. Garcia i Tormo, W. J. Marciano, and R. Szafron. Michel decay spectrum for a muon bound to a nucleus. *Phys. Rev.*, D90(9):093002, 2014.

- [81] T. Suzuki, David F. Measday, and J. P. Roalsvig. Total Nuclear Capture Rates for Negative Muons. *Phys. Rev.*, C35:2212, 1987.
- [82] Sadakazu Haino et al. Measurements of primary and atmospheric cosmic - ray spectra with the BESS-TeV spectrometer. *Phys. Lett.*, B594:35–46, 2004.
- [83] Vardan Khachatryan et al. Measurement of the charge ratio of atmospheric muons with the CMS detector. *Phys. Lett.*, B692:83–104, 2010.
- [84] P. Achard et al. Measurement of the atmospheric muon spectrum from 20-GeV to 3000-GeV. *Phys. Lett.*, B598:15–32, 2004.
- [85] P. Adamson et al. Measurement of the atmospheric muon charge ratio at TeV energies with MINOS. *Phys. Rev.*, D76:052003, 2007.
- [86] P. Antonioli, C. Ghetti, E. V. Korolkova, V. A. Kudryavtsev, and G. Sartorelli. A Three-dimensional code for muon propagation through the rock: Music. *Astropart. Phys.*, 7:357–368, 1997.
- [87] V. A. Kudryavtsev. Muon simulation codes MUSIC and MUSUN for underground physics. *Comput. Phys. Commun.*, 180:339–346, 2009.
- [88] I. Antcheva et al. ROOT — a c++ framework for petabyte data storage, statistical analysis and visualization. *Computer Physics Communications*, 180(12):2499 – 2512, 2009.
- [89] S. Agostinelli et al. Geant4—a simulation toolkit. *Nuclear Instruments and Methods in Physics Research Section A: Accelerators, Spectrometers, Detectors and Associated Equipment*, 506(3):250 – 303, 2003.
- [90] SuperNova Early Warning System. <http://snews.bnl.gov>. (accessed in March 2016).
- [91] H. Wei. Supernova Early Warning in Daya Bay Reactor Neutrino Experiment. In *Proceedings, 15th International Workshop on Advanced Computing and Analysis Techniques in Physics Research (ACAT 2013)*, 2013.

# List of Figures

1.1	Reactor $\bar{\nu}_e$ flux, inverse beta decay cross section, and observed energy spectrum. . . . .	13
1.2	Electron neutrino survival probability vs. distance $L$ . . . . .	14
3.1	Layout of the Daya Bay experiment. . . . .	24
3.2	Schematic drawing of the far experimental hall. . . . .	25
3.3	Drawing of vertical section of the AD. . . . .	28
3.4	Top-view drawing of water pools of near and far halls. . . . .	29
3.5	Distribution of PMT multiplicity per trigger of Cherenkov detectors in all three halls. . . . .	30
3.6	Efficiencies of Cherenkov detectors to AD muons. . . . .	31
3.7	Drawing of RPC modules support frame and photograph of EH3 water pool with 3 ADs installed. . . . .	32
3.8	Average noise in layers of RPC modules in each hall. . . . .	33
3.9	Distribution of prompt and delayed reconstructed energies for pairs of signals of candidate events for IBD. . . . .	35
3.10	Example distribution of delayed energy of the selected IBD events. . . . .	36
4.1	Schematic drawing of cross-section of bare RPC. . . . .	42
4.2	Photograph of an assembled RPC. . . . .	43
4.3	A schematic drawing of a module structure, with top and side view. . . . .	44
4.4	A schematic drawing of a readout strip. . . . .	44
4.5	A schematic drawing of layers inside an RPC module. . . . .	45
4.6	A schematic drawing of flow of the filling gas mixture through the individual bare RPC in the module. . . . .	46
4.7	Diagram of the RPC DAQ system. . . . .	46
4.8	Monitored currents of 7 RPCs during the training period. . . . .	48
4.9	Time variations of room temperature, relative humidity, and atmospheric pressure in RPC testing room. . . . .	49
4.10	Schematic drawing of layout of RPC tests with cosmic muons. . . . .	50
4.11	Example of measured characteristics of RPC with respect to applied HV. . . . .	51
4.12	Distribution of efficiencies of tested RPCs. . . . .	52
4.13	Distribution of applied HV for which the tested RPCs reached 50% of their maximal efficiency. . . . .	53
4.14	Distributions of singles count rates and dark currents of the tested RPCs at applied voltage of 8 kV. . . . .	53
4.15	Photograph of RPC modules in the test shelves. . . . .	54
4.16	Efficiencies of individual patches of an example e module. . . . .	55
4.17	Distribution of RPC modules' overall and patch efficiencies. . . . .	57
4.18	Photograph of RPC test setup built at our institute in Prague. . . . .	58
4.19	Measured efficiency vs applied HV for two small RPCs. . . . .	59
5.1	Simplified Feynman diagram for amplitude of muon decay process which uses only four-fermion contact interaction. . . . .	62

5.2	Simplified diagrams for calculation of the amplitude of muon decay process with radiative corrections. . . . .	62
5.3	Simplified diagrams for calculation of the amplitude of radiative muon decay process. . . . .	63
5.4	Calculated spectrum of electrons from muon decay in Born approximation and with radiative corrections. . . . .	63
5.5	Differential branching ratio of the radiative muon decay with respect to the photon energy $E_{\text{phot}}$ and the electron energy $E_{\text{el}}$ . . . .	65
5.6	Spectra of photons and electrons from radiative muon decay. . . .	65
5.7	Spectrum of total visible energy in muon decay. . . . .	66
5.8	Calculated electron spectrum from muon decays in orbit. . . . .	68
5.9	Example of spectrum of energies of electrons from muon-decay in orbit. . . . .	68
6.1	Distribution of energies for pairs of signals correlated in time. . .	72
6.2	Distribution of time difference between prompt and delayed signal of muon-decay candidate events. . . . .	74
6.3	Measured muon capture rates for $^{12}\text{C}$ and $^{13}\text{C}$ . . . . .	76
6.4	Measured charge ratio of cosmic muons with respect to their momentum. . . . .	77
6.5	Distribution of surface energies of muons with energies lower than 5 GeV in each experimental hall. . . . .	78
6.6	Spatial distribution of muon decays in the detector for muons from nominal selection and from selection with muon signal $<20$ MeV	79
6.7	Distribution of the time of the second signal since the detected muon for events from nominal selection. . . . .	80
6.8	Distribution of the time of the second signal since the detected muon for events with low muon signal. . . . .	80
6.9	Best-fit parameter $\lambda_{\text{cap}}$ from fits to data from EH1 and EH2 for two selections of data and 3 fixed parameters $R_{\mu}$ . . . . .	81
6.10	Spectrum of reconstructed energies of muon-decay signals from the three halls. . . . .	83
6.11	Comparison of energy spectrum of muon-decay signals from MC simulation and from data. . . . .	84
6.12	Example of a selection of the cylindrical layer centered in AD. . .	85
6.13	Efficiency corrected numbers of events selected inside 5 AD layers.	87
6.14	Distribution of reconstructed energies of the muon-decay signal with fit of my model. . . . .	88
6.15	Comparison of muon-signal energy spectrum from MC and data. .	90
6.16	Details of comparison of muon-signal energy spectrum from MC and data in low and high energy intervals. . . . .	91
6.17	Comparison of modeled energy spectrum of muon decays before and after application of detector response function. . . . .	95
6.18	Spectrum of reconstructed energies of muon-decay signals selected in the central region of AD. . . . .	96
6.19	Comparison of energy spectrum of muon-decay signals from MC simulation and from data . . . . .	97

6.20	Comparison of fits of my model and G4 model to edge in muon-decay signal energy spectrum. . . . .	98
6.21	Spectrum of reconstructed energies of the $e^+$ and $e^-$ simulated with initial momentum of $53 \text{ MeV}/c$ . . . . .	99
6.22	Nonlinear energy response and relative resolution of the Daya Bay antineutrino detector to electron and positron events, based on MC simulation. . . . .	99
6.23	Spectrum of reconstructed energies of the selected decay events in EH1 with the fit of my model. . . . .	101
6.24	Best-fit values of energy scale $A$ with varying muon charge ratio $R_\mu$ and the assumed detector resolution $\sigma$ . . . . .	101
6.25	Comparison of a model of ratio of reconstructed energy over true energy with the measurement in this work. . . . .	102
A.1	Comparison of two calculations of radiative-correction function. . . . .	106



# List of Tables

1.1	Overview of parameters of three reactor antineutrino oscillation experiments, Double Chooz, RENO, and Daya Bay. . . . .	17
3.1	Vertical depth and distances of each experimental hall to each pair of the reactor cores. . . . .	24
3.2	Specifications of the three containers and their contained liquids in the antineutrino detector. . . . .	27
3.3	Numbers of PMTs installed in each water pool of near and far halls, EH1, EH, EH3. . . . .	29
3.4	Conditions for trigger of data readout from the Cherenkov detectors. . . . .	30
3.5	List of neutron capture cross sections of hydrogen and of two gadolinium isotopes with highest capture rates. . . . .	35
3.6	IBD selection criteria as applied in [21]. . . . .	37
3.7	List of backgrounds in $\bar{\nu}_e$ detection. . . . .	39
4.1	Efficiencies of patches over central dead areas of a module from MC simulations. . . . .	56
4.2	Module overall efficiency from MC simulations. . . . .	56
6.1	Requirements on coincidence of a signal in AD with signals from muon system detectors. . . . .	73
6.2	Background estimation based on fit to distribution of time differences $\Delta T$ between the prompt muon signal and its decay signal. . . . .	82
6.3	Dependence of efficiency of the cut on reconstructed energy of the muon-decay signal on position in AD. . . . .	86
6.4	A summary of muon-decay candidate sample. . . . .	92



# List of Abbreviations

ACU	Automated Calibration Unit: A, B, or C
AD	Antineutrino Detector
ADC	Analog to Digital Converter
AV	Acrylic Vessel: Inner (IAV) or Outer (OAV)
BESIII	Beijing Spectrometer III
bis-MSB	1,4-Bis(2-methylstyryl)benzol
CAMAC	Computer Automated Measurement And Control
CP	Charge Parity
DAQ	Data Acquisition
DIO	Decay In Orbit
DUT	Detector Under Test
EH	Experimental Hall: 1,2, or 3
ESum	Energy Sum
FEC	Font-end Electronics Card
FEE	Front-End Electronics
FPGA	Field-Programmable Gate Array
GdLS	Gadolinium-doped Liquid Scintillator
HV	High Voltage
IBD	Inverse Beta Decay
IH	Inverted Hierarchy
IWS	Inner Water Shield
K2K	KEK to Super-K Long-Baseline Oscillation Experiment
Kamiokande	Kamioka Nucleon Decay Experiment
KamLAND	Kamioka Liquid Scintillator Antineutrino Detector
kmw.e.	kilometre of water equivalent
LAB	Linear AlkylBenzen: main ingredient of the liquid scintillator
LS	Liquid Scintillator

LTB Local Trigger Board  
m.w.e metre of water equivalent  
MC Monte Carlo simulation  
MINOS Main Injector Neutrino Oscillation Search Experiment  
MKS MKS Instruments, Inc  
MSW Mikheev-Smirnov-Wolfenstein  
NH Normal Hierarchy  
NHit Number of Hits  
OWS Outer Water Shield  
PET Polyethylene Terephthalate  
PMT Photomultiplier Tube  
PPO 2,5-Diphenyloxazole  
PWR Pressurized Water Reactors  
R134a 1,1,1,2-tetrafluoroethane — refrigerant  
RENO Reactor Experiment for Neutrino Oscillations  
ROM ReadOut Module  
ROT ReadOut Transceiver  
RPC Resistive Plate Chamber  
RTM Readout Trigger Module  
SCR Singles Count Rate: rate of signals in RPCs not necessarily originating in cosmic rays  
T2K Tokai to Super-K Long-Baseline Oscillation Experiment  
TDC Time-to-Digital Converter  
TMHA 3,5,5-trimethylhexanoic acid